UNIVERSITY OF OKLAHOMA

GRADUATE COLLEGE

EVALUATION OF ROLLING-TYPE ISOLATION SYSTEMS FOR SEISMIC HAZARD MITIGATION

A THESIS

SUBMITTED TO THE GRADUATE FACULTY

in partial fulfillment of the requirements for the

Degree of

MASTER OF SCIENCE

By

SKYLAR J. CALHOUN
Norman, Oklahoma
2018

EVALUATION OF ROLLING-TYPE ISOLATION SYSTEMS
FOR SEISMIC HAZARD MITIGATION

A THESIS APPROVED FOR THE
SCHOOL OF CIVIL ENGINEERING AND ENVIRONMENTAL SCIENCE

BY

Dr. P. S. Harvey Jr., Chair

Dr. R. W. Floyd

Dr. J. S. Volz

The function of education is to teach one to think intensively and to think critically. Intelligence plus character–that is the goal of true education.
– Rev. Dr. Martin Luther King, Jr.

To my beloved family, thank you for instilling these ideals in me and supporting me throughout my life to reach both my personal and academic goals. I would like to thank my friends for building me up to overcome any obstacles along my journey.

Acknowledgements

I would like to first acknowledge the School of Civil Engineering and Environmental Science in the Gallogy College of Engineering at the University of Oklahoma. The programs in the Gallogy College of Engineering like the Oklahoma Louis Stokes Alliance for Minority Participation (OK-LSAMP) and the Multicultural Engineering Program (MEP) provided me with knowledge about different opportunities around the college. Without these programs, I would have not have participated in undergraduate research, which eventually led me to pursue an advanced degree.

I want to thank the National Science Foundation for their sponsorship of this work. This support is gratefully acknowledged and appreciated. This material is based upon work supported by the National Science Foundation under Grant No. NSF-CMMI-1663376. Any opinions, findings, and conclusions or recommendations expressed in this material are those of the author and do not necessarily reflect the views of the National Science Foundation.

Additionally, I would like to thank my committee members, Dr. Jeffery S. Volz and Dr. Royce W. Floyd, for agreeing to serve on my committee. I appreciate the time and effort they dedicated to encouraging me to perform at my best both academically and professionally.

Finally, I would like to thank Dr. P. Scott Harvey Jr., my advisor, for his willingness to support me throughout my academic career. Since my time as an undergraduate research assistant, Dr. Harvey has helped me discover my potential as an engineer. He

has always assisted me when troubled with certain concepts or tasks. Thank you, Dr. Harvey, for believing in me throughout my journey.

Contents

List of Figures

List of Tables

Abstract

Nonstructural components within mission-critical facilities such as hospitals and telecommunication facilities are vital to a community's resilience when subjected to a seismic event. Building contents like medical and computer equipment are critical for the response and recovery process following an earthquake. A solution to protecting these systems from seismic hazards is base isolation. Base isolation systems are designed to decouple an entire building structure from destructive ground motions. For other buildings not fitted with base isolation, a practical and economical solution to protect vital building contents from earthquake-induced floor motion is to isolate individual equipment using, for example, rolling-type isolation systems (RISs). RISs are a relatively new innovation for protecting equipment. These systems function as a pendulum-like mechanism to convert horizontal motion into vertical motion. An accompanying change in potential energy creates a restoring force related to the slope of the rolling surface.

This study seeks to evaluate the seismic hazard mitigation performance of RISs, as well as propose and test a novel double RIS. A physics-based mathematical model was developed for a single RIS via Lagrange's equation adhering to the kinetic constraint of rolling without slipping. The mathematical model for the single RIS was used to predict the response and characteristics of these systems. A physical model was fabricated with additive manufacturing and tested against multiple earthquakes on a shake table. The system featured a single-degree-of-freedom (SDOF) structure to represent a piece of

equipment. The results showed that the RIS effectively reduced accelerations felt by the SDOF compared to a fixed-base SDOF system. The single RIS experienced the most substantial accelerations from the Mendocino record, which contains low-frequency content in the range of the RIS's natural period (1–2 seconds). Earthquakes with these long-period components have the potential to cause impacts within the isolation bearing that would degrade its performance. To accommodate large displacements, a double RIS is proposed. The double RIS has twice the displacement capacity of a single RIS without increasing the size of the bearing components.

The mathematical model for the single RIS was extended to the double RIS following a similar procedure. Two approaches were used to evaluate the double RIS's performance: stochastic and deterministic. The stochastic response of the double RIS under stationary white noise excitation was evaluated for relevant system parameters, namely mass ratio and tuning frequency. Both broadband and filtered (Kanai-Tajimi) white noise excitation were considered. The response variances of the double RIS were normalized by a baseline single RIS for a comparative study, from which design parameter maps were drawn. A deterministic analysis was conducted to further evaluate the double RIS in the case of nonstationary excitation. The telecommunication equipment qualification waveform, VERTEQ-II, was used for these numerical simulations. Peak transient responses were compared to the single RIS responses, and optimal design regions were determined. General design guidelines based on the stochastic and deterministic analyses are given. The results aim to provide a framework usable in the preliminary design stage of a double RIS to mitigate seismic responses.

Chapter 1

Introduction

1.1 Overview

In the United States, structures are subject to various natural hazards ranging from earthquakes to wildfires. Engineers design structures to withstand the threats these natural hazards pose to humans and the built environment. These occurrences are hard to predict, but there is a continuous need to prepare for them. In some regions of the United States, earthquakes create a threat to many facets of the built environment. Base isolation systems offer a method to protect buildings and their contents (e.g., data cabinets) from the damaging ground accelerations caused by earthquakes. Conventional isolation designs are elastomeric bearings, rocking systems, coil springs, and rollers/ball bearings (Buckle and Mayes, 1990). This study specifically considers rolling isolation systems (RISs) as they relate to buildings, bridges, and equipment, and how RISs can improve the structural performance during earthquakes.

1.2 Background

This section discusses the hazards created by natural disasters and the cost they have on communities and their inhabitants, and how base isolation has been proven and implemented to provide protection for areas prone to earthquakes. Specifically in the case of the 1994 Northridge earthquake, base isolation mitigated the structural damage

that compromised the integrity of typical fixed base buildings. The world's first base isolated hospital, University Hospital at the University of Southern California (USC), demonstrated the advantages of using a base isolation design compared to a fixed base configuration (Housner and Masri, 1994). Furthermore, the nonstructural components within the USC hospital were not damaged–a benefit that the structurally strengthened University of California, Los Angeles (UCLA) Medical Center did not accomplish in the Northridge earthquake. For some facilities such as hospitals, the nonstructural components are as critical as the structural system; therefore, it is important to have these components of a structure protected at all cost. Nonstructural components may range from warehouse racks to data cabinets. Thus it is crucial to have these systems protected in the event of an earthquake. Base isolation is a promising solution because it allows nonstructural components such as data cabinets to move rigidly without the chance of equipment toppling over at lower accelerations than bolted configurations. In particular, the rolling isolation system provides a low-cost and simple installation compared to other base isolation methods, but these systems have a limited displacement capacity. This study will focus on increasing the displacement capacity of these systems without increasing the area of occupancy.

Disasters range from naturally occurring such as earthquakes to anthropogenic (i.e., acts of terror). Natural disasters like the Northridge earthquake have the potential to cause a significant amount of damage to civil infrastructure. The same is true for human-made blasts like the 1995 Murrah Federal Building bombing in Oklahoma City, Oklahoma. In the event of either incident, sensitive equipment such as data cabinets and telecommunication servers need to be protected to ensure uninterrupted business operations. According to Federal Emergency Management Agency (FEMA), the estimated earthquake losses to general building stock in a given year for the entire United States is 6.1 billion dollars (FEMA, 2008). Building-related losses are good benchmarks for

comparative studies of relative regional earthquake risk and to other natural hazards, but they do not fully encompass the total estimated risk from earthquakes. FEMA 366 (2008) detailed the total estimated risk including factors such as amount of debris created and social losses. With the growing numbers of densely populated areas exposed to earthquake risk, the need for innovative solutions for the protection of the general public and the built environment increases as well.

Throughout the last century, there have been substantial developments to mitigate hazards created from these type of disasters. A proposed solution to protecting structures and their contents prone to seismic hazards is using *base isolation*. As a concept, base isolation works to reduce the lateral stiffness of a structure, effectively decoupling a structure from destructive horizontal motions produced by seismic events (Ibrahim, 2008). The system works to either absorb or ignore energy released from a seismic incident. The widely accepted and implemented solution has been used for various applications. In areas susceptible to earthquakes, such as California, newer structures are increasingly fitted with passive isolation systems to increase seismic protection. Generally, older structures are built in the conventional fixed base configuration where the seismic demands are greater for the structural components and its contents (i.e., equipment). Base isolation provides an alternative to the standard, fixed-base design of structures and may be more cost efficient for new buildings in highly active seismic locations (Chopra, 2012).

In the incidence of one of the strongest earthquakes to hit the Los Angeles metropolitan area, the Northridge earthquake ($M_w = 6.7$) provided evidence on the benefits of base isolation and how it can prevent significant damage to isolated structures (Housner and Masri, 1994). Northridge cost 42 billion U.S. dollars in total damages and left 57 people dead, thousands of people injured, and 112,000 structures damaged. The earthquake created widespread disruption of health care facilities around the affected

area (EQE, 1994). In the EQE International Inc. summary report (1994), it was noted that the California Office of Statewide Health Planning and Development (OSHPD) assembled teams of disaster reconnaissance professionals consisting of structural engineers, fire marshals, and construction advisers to survey the nearly 750 state-licensed facilities of the afflicted area. Within the first week of inspections, OSHPD examined approximately 400 facilities for damage. It was reported that around 95 % of the examined structures did not endure significant structural damage, but widespread substantial damage occurred to nonstructural items such as equipment. As a result, equipment failure posed an additional threat to human life, especially in hospitals where patients are depending on life-saving machines to properly work. Eight facilities were deemed unsafe due to the earthquake damage to structural systems or nonstructural elements. The eight facilities were older structures that were built before the provisions of the seismic design codes and structural design reviews (EQE, 1994).

Numerous structures and systems were severely damaged. However, the several structures fitted with base isolation withstood the strong ground motions, one of which was the USC University Hospital. The 8-story structure was fitted with a total of 149 isolation bearings: (81) elastromeric and (67) lead-rubber bearings. In the initial design of the structure, fixed-base and base-isolated designs were considered, but upon further evaluation of the cost of potential damage of a strong earthquake the latter was selected. The building was located 35 km away from the Northridge earthquake epicenter. During the earthquake, the ground motions were recorded in four additional base isolated structures and the USC University Hospital experienced a 34 % acceleration reduction (Housner and Masri, 1994), thus proving that base isolation effectively reduces horizontal motion felt by a building but does not entirely attenuate them. It is worth noting the building did not suffer any damage to its structural or nonstructural components (EEFIT, 1997).

Other buildings in the area had different seismic protection strategies. The Olive View-UCLA Medical Center building was strengthened as a result of the 1971 Sylmar earthquake. The building was seismically retrofitted with a new steel frame and steel-plate shear walls (EQE, 1994). When the Northridge earthquake occurred, the recorded motion of the earthquake on the building was reported as some of the strongest shaking ever documented according to EQE (1994). Despite these strong motions, the Olive View Hospital suffered little to no structural damage, but nonstructural elements were damaged severely. Highlighted by Porter et al. (1993), most buildings depend as heavily on their nonstructural components as their architectural and structural features. Within buildings such as hospitals, the failure of equipment can impair the facility's functionality, causing detrimental effects to the community's ability to respond from a catastrophic event. For patients in critical care within a hospital damaged by an earthquake, it is crucial for every machine/equipment to remain functional throughout the duration of the slightest earthquake tremors. For instance, two seismically designed chillers on top of the Olive View hospital failed and caused piping failure that leaked water throughout the building. As a result, the facility was out of commission for one week (FEMA, 2004). Most of the nonstructural damage in healthcare facilities during the Northridge earthquake were due to water related components.

Many commercial buildings suffered severe interior damage, especially department stores where large items were placed on elevated racks with large masses. This created increased overturning moments during the Northridge earthquake due to its fixed-base configuration. Similarly, the same was true for warehouse, where racks with improper or poor anchorage caused mass eccentricities to occur during the earthquake, which then subsequently led to failure. Noted in the EQE (1994) report, a 5,115 square meter concrete tilt-up warehouse endured severe damage from the destruction caused by the failure of warehouse racks within the building's interior. The racks appeared to fail due

to progressively collapsing on one another. The EQE report suggests that the design of these racks requires an improvement in anchorage design.

Commercial businesses such as companies that house data centers suffered significant losses from earthquake-induced interior damage as well. Companies like IBM and Comdisco had to move their data center operations to back-up sites following the Northridge earthquake. In a prior earthquake, the 1989 Loma Prieta earthquake, various data centers were damaged and data operators were force to move their processing to alternate sites (Devlin et al., 1997). Notably, the interest of this thesis is the protection of physical hardware within data centers from created accidents by earthquake-induced motion. For reliability purposes, it is important that these nonstructural components remain active during any disturbance from an earthquake. There would be major societal and economical impacts if the data were lost due to an interruption of data processing. Depending on the importance of each facility sheltering the data center, the data processing operation can be critical to the response and recovery in the event of a strong earthquake (Porter et al., 1993). For example, businesses would struggle to relocate information due to discontinuity of data processing or community leaders would labor with the issue of locating areas of need if lines of communication are severed throughout the impacted area. Base isolation provides a promising solution to protecting nonstructural components such as data centers from destructive ground motions created by intense earthquakes.

Seismic isolation allows for a building or a warehouse racks to move as a rigid body when excited by an earthquake, preventing overtoppling of the structure of interest. Whether it is isolating the entire building or isolating an individual item, residual movement in both of these seismic designs poses a threat to utilities such as equipment and piping that would need additional accommodations for large lateral movement. This study will provide additional information about the benefits of base isolation when ac-

commodating for significant lateral movement. In the next section, the basic theory of seismic base isolation is described.

1.2.1 Basic Theory of Seismic Isolation

In active seismic areas, buildings and their contents are susceptible to harmful vibrations from earthquake ground motions, which pose a threat to the structural integrity of buildings and damage to sensitive equipment. Consider the fixed-base building shown in Fig. 1.1(a), which has lumped mass m, damping coefficient c, and lateral stiffness k. The natural period of the fixed-base structure is given by

$$T_{\mathrm{f}} = \frac{2\pi}{\omega_{\mathrm{f}}} \quad \text{where} \quad \omega_{\mathrm{f}} = \sqrt{\frac{k}{m}} \tag{1.1}$$

The natural period calculated from this equation, together with the damping ratio

$$\zeta_{\mathrm{f}} = \frac{c}{2\sqrt{km}} \tag{1.2}$$

is used to determine the pseudo-acceleration and hence earthquake-induced forces in the structure from elastic design spectra (Fig. 1.2). The fundamental period of low- to medium-rise buildings is commonly in the range of periods where earthquake energy is strongest, giving rise to large spectral accelerations. These accelerations can be reduced if the structure is designed to be more flexible (longer period), but this approach may be

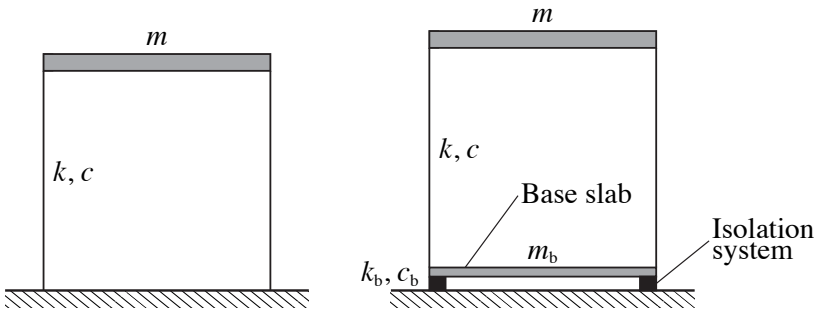

Figure 1.1: Conceptual idealization of fixed-base (a) and isolated (b) structures.

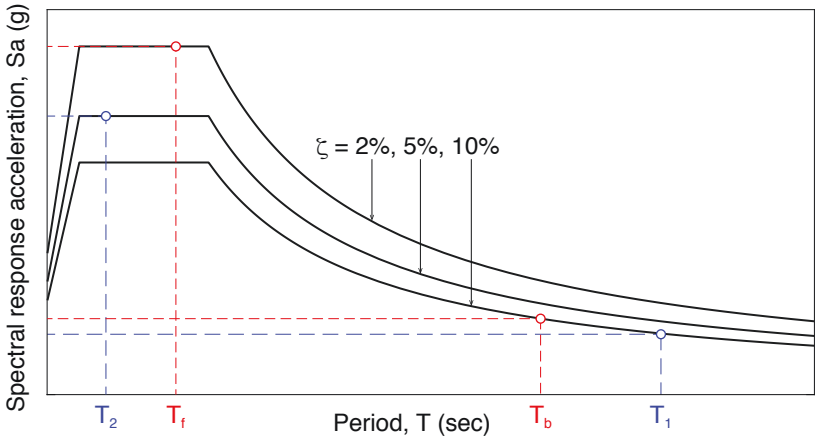

Figure 1.2: Elastic design spectra.

neither feasible nor practical (Kelly, 1990). The necessary flexibility can be achieved by *base isolation*.

Consider the same *m*-*c*-*k* structure from before, but now mounted on a base slab of mass m_b supported by isolation bearings [Fig. 1.1(b)]. The isolation system has lateral stiffness k_b and damping coefficient c_b. The period of the isolation system, assuming the building to be rigid, is given by

$$T_\mathrm{b} = \frac{2\pi}{\omega_\mathrm{b}} \quad \text{where} \quad \omega_\mathrm{b} = \sqrt{\frac{k_\mathrm{b}}{m + m_\mathrm{b}}} \tag{1.3}$$

The base isolation period T_b must be much longer than the fixed-base period T_f in order to be effective in reducing the spectral accelerations and as a result the forces in the building.

The equations of motion for the above 2DOF system [Fig. 1.1(b)] subject to ground excitation $\ddot{u}_\mathrm{g}(t)$ are

$$m_\mathrm{b}\ddot{u}_\mathrm{b} + (c_\mathrm{b} + c)\dot{u}_\mathrm{b} - c\dot{u}_\mathrm{r} + (k_\mathrm{b} + k)u_\mathrm{b} - ku_\mathrm{r} = -m_\mathrm{b}\ddot{u}_\mathrm{g}(t) \tag{1.4}$$

$$m\ddot{u}_\mathrm{r} - c\dot{u}_\mathrm{b} + c\dot{u}_\mathrm{r} - ku_\mathrm{b} + ku_\mathrm{r} = -m\ddot{u}_\mathrm{g}(t) \tag{1.5}$$

where u_b and u_r are the base slab and roof displacements relative to the ground, respectively. Alternatively, in matrix form:

$$\mathbf{M}\ddot{\mathbf{u}}(t) + \mathbf{C}\dot{\mathbf{u}}(t) + \mathbf{K}\mathbf{u}(t) = -\mathbf{M}\boldsymbol{\iota}\ddot{u}_{\mathrm{g}}(t) \tag{1.6}$$

where

$$\mathbf{M} = \begin{bmatrix} m_{\mathrm{b}} & 0 \\ 0 & m \end{bmatrix},\ \mathbf{C} = \begin{bmatrix} c_{\mathrm{b}} + c & -c \\ -c & c \end{bmatrix},\ \mathbf{K} = \begin{bmatrix} k_{\mathrm{b}} + k & -k \\ -k & k \end{bmatrix},\ \boldsymbol{\iota} = \begin{Bmatrix} 1 \\ 0 \end{Bmatrix},\ \mathbf{u} = \begin{Bmatrix} u_{\mathrm{b}} \\ u_{\mathrm{r}} \end{Bmatrix} \tag{1.7}$$

The two-degree-of-freedom system that defines the isolated structure [Fig. 1.1(b)] has two natural periods (T_1, T_2) that are close to, but do not exactly match, the fixed-base period T_{f} and isolation period T_{b}. The periods of the coupled system are given by

$$T_1 = \frac{2\pi}{\omega_1} \quad \text{and} \quad T_2 = \frac{2\pi}{\omega_2} \tag{1.8}$$

where the natural frequencies are found from solving the homogeneous solution of Eq. (1.6), $\det(\mathbf{K} - \omega^2\mathbf{M}) = 0$ (Kelly, 1999):

$$\omega_{1,2}^2 = \frac{1}{2(1-\gamma)}\left[\omega_{\mathrm{b}}^2 + \omega_{\mathrm{f}}^2 \mp \sqrt{(\omega_{\mathrm{b}}^2 - \omega_{\mathrm{f}}^2)^2 + 4\gamma\omega_{\mathrm{b}}^2\omega_{\mathrm{f}}^2}\right] \tag{1.9}$$

in which the mass ratio γ is defined as

$$\gamma = \frac{m}{m + m_{\mathrm{b}}} \tag{1.10}$$

Fig. 1.3 shows the influence of γ and the period ratio $T_{\mathrm{b}}/T_{\mathrm{f}}$ on the coupled system's modal periods.

The first mode is called the *isolation mode* because the isolation system undergoes deformations but the structure behaves essentially rigid. The second mode is called the *structural mode* because it involves deformation of the structure as well as the isolation system. While the structural mode's pseudo-acceleration may be large (Fig. 1.2), this mode is essentially not excited (Chopra, 2012) and contributes little to the earthquake-induced forces in the structure. The earthquake-induced forces are dominated by the

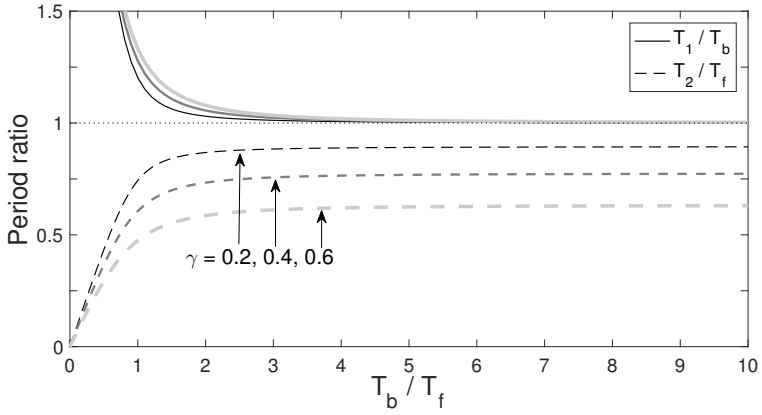

Figure 1.3: Effect of mass ratio γ and uncoupled period ratio $T_\mathrm{b}/T_\mathrm{f}$ on the coupled system's natural periods T_1 and T_2.

fundamental (isolation) mode, which has low pseudo-accelerations (Fig. 1.2). Further, these forces are carried by the isolation bearings because the isolation mode involves deformations primarily in the isolation system. Hence, the primary benefit of base isolation is the lengthening of the fundamental period, reducing earthquake-induced forces in the building. A secondary benefit of base isolation is the reduction in structural response through the damping in the isolation system (Kelly, 1999).

Various studies over the past several decades have shown base isolation as a feasible option to mitigate strong disturbances caused by earthquakes (Kelly, 1986). Base isolation preserves the structural integrity of the built environment by reducing the seismic forces transmitted from the ground into the structure. Base isolation introduces a flexible interface between the ground and the superstructure; the flexibility increases the period of the structure to the long range (e.g., two to four seconds), which lowers peak accelerations felt by structures affected by earthquakes with high-frequency content (Warn and Ryan, 2012). Base isolation is a practical solution for protecting data centers because the entire floor of data cabinets can be isolated or individually isolated. The common types of flexible systems are elastomeric bearings, rocking systems, coil springs, sliding plates, and rollers/ball bearings (Buckle and Mayes, 1990). The next

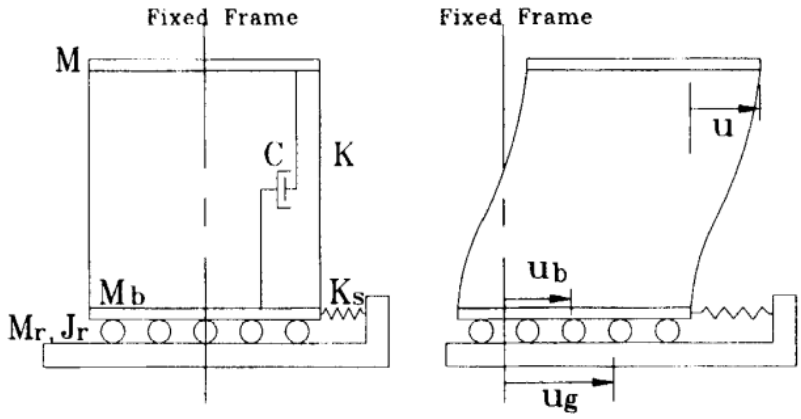

Figure 1.4: Structure isolated by free rolling rods under basement. Source: Lin et al. (1995).

section highlights the various applications of rolling-type isolation.

1.3 Applications of Rolling-Type Isolation

1.3.1 Buildings

In Lin and Hone (1993) and Lin et al. (1995), free rolling rods for base isolation was implemented. In these two studies, the use of two sets of orthogonal free rolling rods to isolate a single-story building was proposed, as shown in Fig. 1.4. Due to the flat rolling surface, "the maximum forces of excitation transmitted into the superstructure by earthquakes are the rolling friction in the isolation device" (Harvey and Kelly, 2016). Lin and Hone (1993) recommended a coefficient of rolling friction $\mu \leqslant 0.01$ because it can be effective on any site. They found that the maximum displacements across the isolation system were 1.5 times the peak ground displacement (PGD), and a control force that could act as a re-centering device was proposed. Lin et al. (1995) used a soft spring as the control force to reduce large displacements, resulting in permanent deflections of "nearly zero."

In a numerical study, Jangid (2000) found that cylindrical rolling rods could be placed in a parallel configuration to a re-centering device below a multi-story struc-

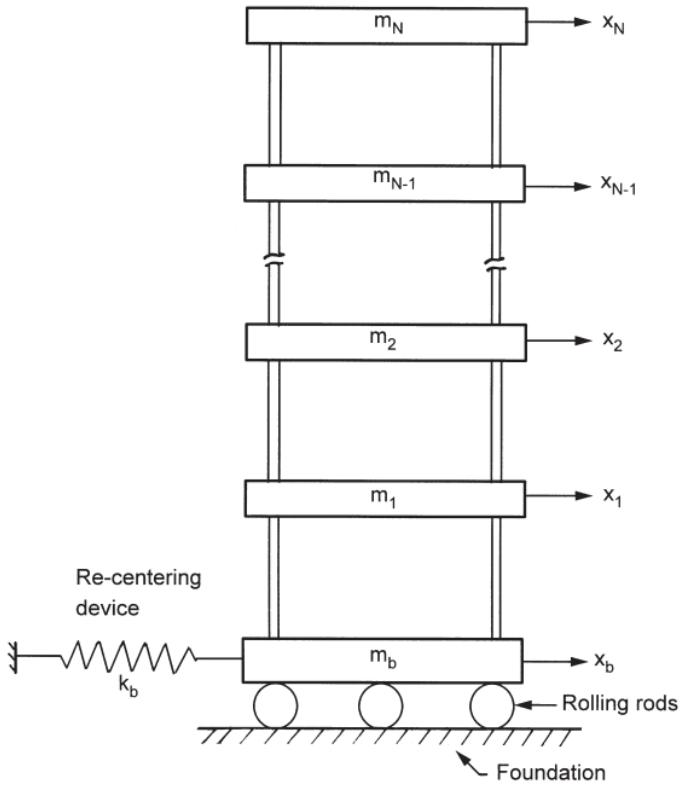

Figure 1.5: Structural model of multi-story building supported on rolling rods. Source: Jangid (2000)

ture, as shown in Fig. 1.5. The study found that "the optimal friction coefficient of the rolling rods decreased with the increase of the number of stories in the superstructure (provided the other parameters, like the duration of isolation tests, are held constant)" (Jangid, 2000). Notably, when the ground motion periods become longer in time, the optimum coefficient of friction decreases. The results showed that the isolation system's base displacement was larger for extended time periods, thus posing a threat to an isolation system′s displacement capacity (Jangid, 2000). In a study to investigate the behavior of rubber layer roller bearings as a base isolator for low-rise structures, Foti and Kelly (1996) found that the system performed well. Harmonic excitation and earthquake motion tests determined that a system with high damped natural rubber pads and steel balls is capable of absorbing significant amounts of energy during a single dis-

placement cycle. The system continued to function well with increased ground motion (Foti and Kelly, 1996).

A study conducted by Houseini and Soroor (2011) continued on the same idea of isolating entire structures; the researchers used bi-axial rolling isolation of two orthogonal pairs of rollers on concave beds (OPRCB) for short- to mid-rise buildings. This design is an affordable and efficient alternative to existing retrofitting methods because typical earthquake retrofitting is expensive (Houseini and Soroor, 2011). The system's robust ability to provide restoring and re-centering capabilities mitigates issues found with other isolation systems. The OPRCB's simplicity of fabrication, installation, low cost, low weight and small dimensions boost the system's practicality (Houseini and Soroor, 2013).

When a building is isolated, it can behave as a linear system. Linear behavior means the displacements increase by the same amount as the accelerations increase in an earthquake. There are cases where the isolation system does not behave in this linear fashion, making the structure's responses in an earthquake hard to predict. Studies conducted by Chung et al. (2009) and Yang et al. (2011) determined the benefit of nonlinearities in building isolation. Chung et al. (2009) reported that linear isolators used at locations near a fault may experience resonance and large displacement response, while nonlinear isolation may avoid this situation due to its varied vibration period. The authors described how the eccentrically pinned cylindrical rollers created re-centering forces that allowed for the system to always return to its neutral position, thus creating a stable system. The system consisted of a pin-connection between a mass block (representing a structure or equipment) to a set of circular rolling isolators. The frictionless pins were connected eccentrically to the isolator. They also illustrated how the eccentric rolling isolation system (ERIS) avoided the coupling effect of resonance with significant displacement, as opposed to the linear isolation system for both near-fault ground

motions and far-field earthquakes (Chung et al., 2009). These results give engineers the confidence to design isolation systems that are likely to experience nonlinear responses.

Wei et al. (2013) conducted a numerical study of a rolling damper isolation system with different damping constants and rolling friction coefficients. The authors stated that further review would be needed to select the most optimal combination of damping and friction.

1.3.2 Bridges

When modeling bridges for seismic hazards, it is vital to redistribute vertical and lateral loads from the dynamic loading of vehicles and earthquakes. Typically, the displacement capacity is more significant for bridges than buildings because of the size of the structure compared to buildings. In the studies below, the importance of the slope of the rolling profile and the friction forces are highlighted to allow for bridges to return to the center of their rolling profiles.

Kasalanati et al. (1997) were the first to study bridge application of a RIS, named the "Ball-in-Cone" (BNC) system. The full-scale experimental system consisted of two steel plates with a spherical metal ball. The plates were sloped at 1:10 and frictional dampers were used. Four bearings and two dampers were utilized for the bridge experiment. Kasalanati et al. (1997) tested forty-two scenarios of varying earthquakes on the system. Hardened steel plates were preferred because the steel plates were more effective in resisting the creation of grooves by the steel balls through the repetition of testing. The bridge deck acceleration was found to be 4-6 times lower than non-isolated systems.

Tsai et al. (2007) created a RIS for a 1/7.5-scale single span bridge with a V-shaped rolling dishes with a cylindrical roller. Two tests were performed: one with viscous dampers and one without viscous dampers. The viscous dampers reduced bearing displacements and stopped deck oscillation. Tsai et al. (2007) also found that the seismic

force of the test transmitted through the bearings was independent of the shaking intensity due to the constant slope of the bearings. Ou et al. (2010) studied rolling isolation bearing on highway bridges. Their system was similar to Tsai et al. (2007), but Ou's system had two cylindrical rollers instead of one. Ou et al. (2010) altered the slope angle to find that the RIS would not return to the center if the angle was created below 2 degrees, and slipping might occur with an angle higher than 8 degrees. Lee et al. (2010) found that an upper bound of 10 degrees could ensure rolling without slipping.

Ou et al. (2010) executed a numerical study of twenty-eight horizontal ground motions separated in categories of near-fault, high velocities; high frequency, high acceleration; and moderate ground shaking, which were performed on highway bridges. The results showed that the peak displacement increased as the peak ground acceleration (PGA) increased without frictional forces; the peak displacement and periods decreased as the frictional forces increased. The study found that a large isolator slope had a larger bearing strength, larger displacement capacity, and lower effective period. Notably, the addition of frictional forces outperformed changing the profile's slope. The best performance was found when both frictional forces and a steeper slope were simulated. This result was preferred because it lowered displacements, but at the cost of increasing accelerations (Ou et al., 2010).

1.3.3 Equipment

When isolating a building, it is important to decouple the structure from the dangerous ground motions; the building holds critical contents that need to be protected. The contents of the building consist of vital equipment (e.g., server cabinets) that is integral to business operations. Therefore, it is critical to ensure that the structure and equipment are protected from dangerous earthquake-induced motions. A feasible solution is base isolation of individual contents. Base isolation provides a method of attenuating energy transmitted into equipment. The following is a survey of how base isolation of

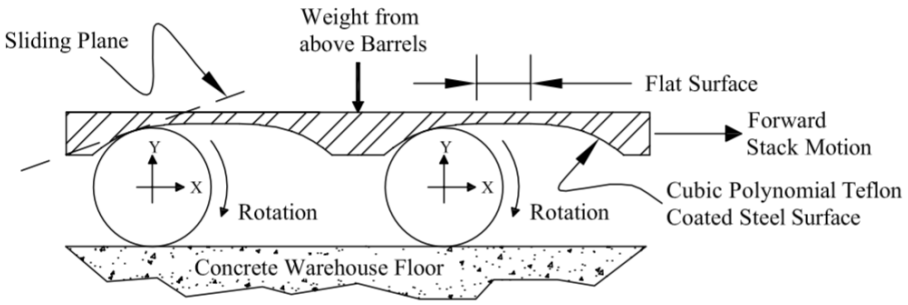

Figure 1.6: Wine barrel isolation system layout. Source: Chadwell et al. (2009)

individual building contents has been applied previously. Chadwell et al. (2009) experimented with rolling isolation to protect wine barrel stacks in California. For isolation of wine barrels, the main objective of protection is on collapse prevention. Large lateral displacements were not of concern in this design. The isolation system consisted of a high strength steel ball bearing coated in Teflon with a cubic polynomial profile on a flat concrete floor. Fig. 1.6 shows the configuration of the isolation system (Chadwell et al., 2009). The configuration shown does not have a limited lateral displacement restriction on the bottom half of the system because it is directly on the warehouse floor. As mentioned by Lin et al. (1995), flat isolation systems can experience large displacements, which can be dangerous if the system was to reach its displacement capacity.

Seismic isolation has been implemented to protect buildings and other large structures from earthquake shaking in seismically active areas since the 1970s. Isolation systems for data centers is a cheaper alternative to isolating an entire building. WorkSafe Technologies produce isolation systems to help isolate computer servers and sensitive computer equipment. WorkSafe's BNC technology is a seismic isolation system consisting of two steel dishes and a ball bearing that is capable of isolating individual data cabinets as well as entire rows of cabinets. Nacamuli and Sinclair (2011) conducted a review of WorkSafe's: ISO-Base isolation system, Isolated Raised Access Floors (IRAF), and the Isolated Equipment Platform. These systems use BNC technology to provide seismic hazard mitigation for a range of applications. The ISO-Base isolator is capa-

Figure 1.7: Typical isolation platform for computer rack using ISO-Base system (WorkSafe Technologies, Inc., 2011).

Figure 1.8: Isolated Raised Access Floors Structural System (WorkSafe Technologies, Inc., 2011)

ble of handling relatively low axial loads compared to the other two systems. Fig. 1.7 displays a typical ISO-Base plank system used for a single computer rack.

Nacamuli and Sinclair (2011) found that ISO-Base had lateral limitations of 8 inches that might make the system unsuitable for large earthquakes. The IRAF applies the same technology as the ISO-Base but to an entire access floor by elevating the access floor on the isolator's pedestals shown in Fig. 1.8. The IRAF system had many benefits that the ISO-Base system did not have, namely a large displacement capacity of 18 inches,

higher payloads, and possible viscous damper installation. The Isolated Equipment Platform had similar benefits to the IRAF; however, it extends the use of BNC isolators to specific needs of broader applications such as large equipment, fragile art installation, and lightly-framed residential construction.

The double (or stacked) RIS concept proposed by Harvey and Gavin (2014) helps to increase the displacement capacity of isolation systems. The RISs in use today have displacement capacities of about 20 cm compared to a double RIS full displacement capacity of 44 cm. In their study, Harvey and Gavin (2014) investigated the non-linear behavior of the double RIS by creating a complete model of the coupled dynamics. The model was validated through numerical and experimental testing. The system was simulated through a range of shake table disturbances of levels ranging from weak to strong motion for a given floor motion period. For a moderate disturbance at a parameterized period of 1.60 seconds, the displacement of the double RIS did not exceed 30 cm. This additional displacement capacity allowed the system to be capable of handling more considerable disturbances.

Pendulum-type isolation bearings are the topic of interest in this study which includes RISs. This study will characterize double RISs with adaptive behavior. Adaptive behavior means that this system's response is displacement dependent and values of the displacement amplitudes can be calculated and controlled by the change of the stiffness and effective friction of the system (Fenz and Constantinou, 2008a,b). While the focus of this study is on rolling-type isolation systems, more extensive research has been conducted on friction pendulum isolation systems (FPSs) with the goal of achieving displacement-dependent adaptive behavior. This study will draw upon the findings of studies of FPSs, in particular, the triple pendulum bearing.

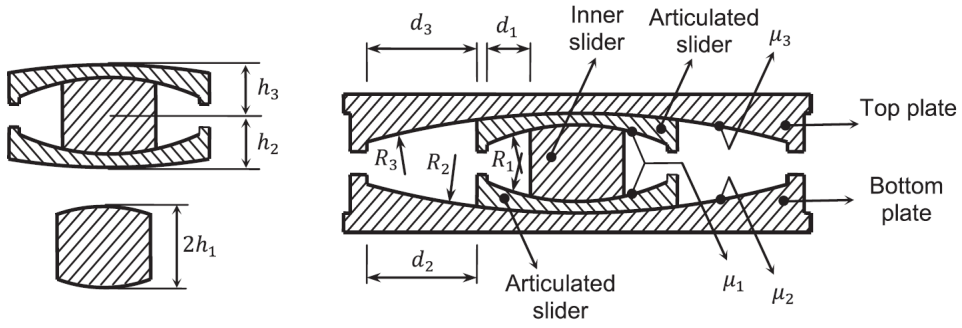

Figure 1.9: Section view of Triple Pendulum bearing. Source: Dao et al. (2013).

1.3.4 Friction Pendulum Systems

The friction pendulum concept for seismic isolation dates back to a 1967 patent by Penkuhn (1967). In particular, the first adaptive friction pendulum system that featured multiple independent mechanisms was introduced by Tsai et al. (2010). Currently, the Triple Pendulum^{TM} (TP) for seismic isolation is widely manufactured by Earthquake Protection Systems, Inc. (EPS), which consists of four concave surfaces and three independent pendulum mechanisms shown in Fig. 1.9. The system consists of two articulated sliders and an inner slider. Depending on the level of disturbance in the horizontal direction, each slider helps to dissipate energy. The curvature of the slider combined with the vertical load provides a restoring force when lateral displacement occurs. The geometrical parameters and friction coefficients dictate which different pendulum mechanism engages during different earthquake levels (Dao et al., 2013). As shown in Fig. 1.9, three pendulum mechanisms occur: first between the inner slider and two articulated sliders, second between the lower articulated slider and bottom concave plate, and lastly between the upper articulated slider and top concave plate. Each mechanism is reserved for small, moderate, and large earthquakes, respectively. In Fig. 1.9, the friction coefficient μ_i between surfaces and displacement limit d_i of the sliders determines the stiffness of each stage to reduce the displacement demand of the TP or slow the movement of the structure above the isolator. These properties of the system prevent

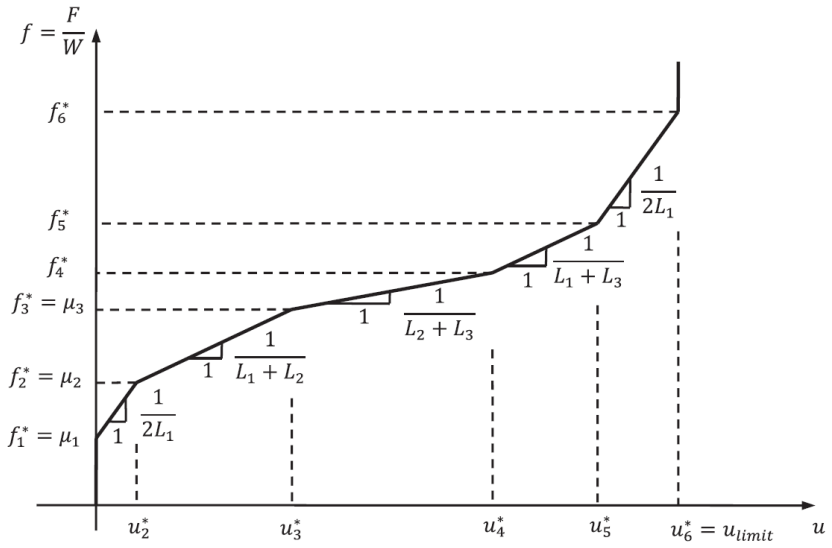

Figure 1.10: Backbone curve of standard TP bearing. Source: Morgan and Mahin (2011).

the overall displacement limit from being reached in an extreme earthquake, thus preventing a system failure. The response of a TP bearing is determined by the design parameters μ_i, d_i, and L_i. L_i is the effective pendulum lengths ($L_i = R_i - h_i$) where R_i = radius of the spherical radius and h_i = height measured from end-to-end of an given pendulum mechanism (Dao et al., 2013). According to Fenz and Constantinou (2008a) and Morgan and Mahin (2011), the backbone curve of the force-deformation of a standard TP bearing can be divided into five stages as shown in Fig. 1.10. These curves can be used to control the response of the system.

1.4 Vibration Absorption

Another common vibration mitigation strategy is *vibration absorption*. Vibration absorption for fixed bodies like buildings reduces the main structure's largest disturbance amplitude, also known as the resonance response, by the use of a secondary system such as a tuned mass damper (TMD). A TMD, or dynamic vibration absorber (DVA), is a passive vibration control device which is attached to a vibrating structure labeled the primary structure subjected to an external force or motion. Frahm (1909) was the first

to apply the concept behind tuned mass vibration absorbers. He managed to determine if an undamped auxiliary device is tuned to the undamped natural vibration frequency of the main structure, then the device effectively damps the main structure's response to approximately zero. He applied this concept to reduce the rolling motion of ships.

Ormondroyd and Den Hartog (1928) worked to improve the theory behind Frahm's design for a wide range of frequencies not just one frequency. The initial theory was designed for an undamped main structure subjected to a sinusoidal force excitation with a damped vibration absorber. They introduced discussion about optimal tuning and damping parameters. When these parameters were changed certain points remained at the same location regardless the amount of the change of damping and tuning frequency. As a result, the invariant points allowed for the arrival of the analytically optimal solution described in more detail by Den Hartog (1985). In Asami et al. (2002), it is said that the optimum tuning parameter ν_{opt} of the Voigt type DVA was first derived by Hahnkamm (1932). Hahnkamm's method of deriving the optimum tuning parameters is said to be the fixed-point theory (the invariant points noted above). Brock (1946) derived the expression of the optimum absorber damping utilizing the theory Hahnkamm developed. This is highlighted in the textbook *Mechanical Vibration* by Den Hartog (1985). Noted by Ozer and Royston (2005), invariant points only exist for systems where the main structure is undamped, although invariant points do not exist for real systems with damping. However, research has been found for lightly damped main structures, and the optimal parameters of Den Hartog's method are "nearly optimal" (Ozer and Royston, 2005). Studies focused on damped single-degree-of-freedom (SDOF) and multiple-degrees-of-freedom (MDOF) main systems are summarized by Ozer and Royston (2005).

This study considers a double rolling isolation system (RIS) with damping in both the primary and the secondary isolator. A similar study has been conducted by Becker

and Ezazi (2016); the authors studied a dual isolation system, where the two layers of isolation were at the base and mid-story of the structure. They found by modeling the dual isolation system as a two DOF model, a simpler analysis can be done by assuming the superstructures above each isolation layer behave as rigid bodies, thus each pair of superstructures and isolators were considered a single DOF. Becker and Ezazi (2016) established that the simplified model yielded similar displacement demands as a MDOF reduced to a 2DOF model created by Takewaki (2008). The equations of motions used by Becker and Ezazi (2016) were the same equations given by Naeim and Kelly (1999) for classic base isolation. Becker and Ezazi (2016) observed that the dual isolation holds similarities to "both traditional isolation and TMD theory," therefore permitting the compared performances of each system.

Continuing in the same direction of Becker and Ezazi (2016) report, this study will examine and optimize the double RIS's behavior when subjected to random base excitation. Optimization for DVA were first proposed by Frahm (1909), where he reduced the response of a single resonant frequency, as known as H-Infinity (H_∞). The objective of H_∞ is to minimize the maximum amplitude response of the primary system (Asami et al., 2002). Asami et al. (2002) provides an analytic series solution for H_∞ optimization for absorber parameter when the primary system is damped. For a randomly excited primary system, the excitation comprise of "infinitely many" frequencies, so any of these forcing frequencies could detrimentally damage the system. Therefore, it is preferred to focus on all frequencies, not only the resonant frequencies.

Crandall and Mark (1963) first proposed H-Two (H_2) optimization criteria for the design of a damped DVA. The optimization criteria was to reduce the area underneath the frequency response curve of the primary system. The exact solution for H_2 optimization for the DVA attached to undamped primary system was determined by Iwata (1982) and Asami et al. (1991). Asami et al. (2002) proposed the exact closed-form

solution of the H_2 optimization for the DVA attached to a damped primary system. It is worth noting that the main objective for the DVA is to improve the steady state response of the primary system. It was deemed for this thesis to use H_2 optimization. RIS's design parameters (tuning frequency ratio and damping ratios) associated with a cost function will be optimized using the H_2 control method through numerical integration and compared with a classic isolation system.

1.5 Research Overview

Previous studies such as Harvey (2013) and Casey (2017) highlighted the benefits of RISs and their capabilities of seismic hazard mitigation through simulated and experimental tests. Using the lessons learned from their studies this study seeks to evaluate and optimize RISs to achieve performances not previously achieved. The objectives of this study are:

1. Restrict expected accelerations below the object of interest's acceleration tolerance;

2. Increase the displacement capacity of rolling-type isolation systems;

3. Assess rolling-type isolation systems through simulations validated by experimental systems;

4. Develop a design approach for rolling-type isolation system for practical use in the field of earthquake engineering.

1.5.1 Decrease Acceleration Demand

When facilities that house mission-critical systems are subjected to strong floor motion, the systems may fail. The floor motion from an earthquake may create significant damage to free-standing objects, excessive structural deformation, and even structural

failure (Harvey and Gavin, 2014). Restraining equipment by bolting or welding it to the floor may prevent toppling and decrease relative displacements at the cost of increasing inertial loads and deforming of equipment (Lopez Garcia and Soong, 2003a,b). Noted by Harvey and Gavin (2014), amplification of acceleration can be avoided by introducing a sliding or rolling interface. Isolation bearing, sliding isolators, and rolling isolation systems provide a flexible interface between the ground and the equipment; the flexibility lengthens the period of the isolated system and shifts the system away from the predominant period of the disturbance, avoiding resonant effects. Previous studies such as Harvey and Gavin (2014) have proven the principle of seismic isolation can be effective for protecting equipment and structures. The same principle will be implemented in this study for the double RIS.

1.5.2 Increase Displacement Capacity

Various studies have looked at methods to increase the displacement capacity of RISs (Harvey and Kelly, 2016). Methods proposed have considered increasing the bowl diameter and stacking two identical RISs on top of one another. The former would be the preferred method because of the ease of adapting a geometric property of a single isolator instead of fabricating and installing another isolator to the single isolator. According to Harvey (2013), two issues arise when adjusting the bowl diameter to accommodate large displacements. First, the platform footprint needs to increase to conform with the increase of the bowl diameter. For certain projects, space could be limited and the platform footprint has to remain fixed. If the system does not increase the platform footprint, the top-frame of the RIS is more likely to overturn from large platform displacements or mass eccentricities. Second, particularly for a conical bowl profile when the bowl diameter is increased, the ball-bearing diameter has to equally increase to ensure the appropriate clearance between the top and bottom bowl for the system when stationary at zero displacement. It is noted that when steel ball-bearings increase in size,

the cost rapidly increases, proving to be cost inefficient. The double RIS configuration surmounts the shortcomings of the previous method by keeping the platform footprint and rolling profile the same (Harvey, 2013). The considered double RIS, originally proposed by Harvey and Gavin (2014), has twice the displacement capacity of the single subsystems alone with the addition of an increase in the height of the system.

1.5.3 Design and Evaluate Double RISs

Once the double RIS is designed to suppress high accelerations from an earthquake by enduring large displacement across its rolling profile, there lies a level of stiffness (radii) where the optimal performance is achieved. This can be done through common practice for optimizing the behavior of a tuned mass damper (e.g., H_2 control). This technique will be applied to the double RIS to find values of damping, mass, and tuning ratios dependent on the system's stiffness where the RIS is utilizing its full displacement capacity of both isolators to reduce accelerations (i.e., total accelerations).

1.5.4 Practical Application

The double RIS will be optimized according to its performance against a synthetic waveform to test the protection of equipment during an earthquake (i.e., VERTEQ-II). The generic standard for network equipment building systems (NEBS) physical protection created by Bell Communications, outlines the test procedure for equipment and provides the time history for VERTEQ-II (Telcordia Technologies, 2012). This study will utilize VERTEQ-II to create design response curves for practical use for equipment isolation design.

1.6 Summary

In summary, recent studies have shown seismic isolation to be a successful solution for seismic hazard mitigation (e.g., USC University Hospital). In early isolation systems,

where the isolation layer is placed between the superstructure and the substructure, the reduction of accelerations of the structure is achieved at the cost of large displacements at the isolation layer. For designers to meet this displacement demand, large isolation gaps must be provided (Becker and Ezazi, 2016). For structures located in crowded locations where real estate is at a premium or additional space is not available, such gaps would not be possible. Therefore, the challenge for the implementation of base isolation arises. Noted by Becker and Ezazi (2016), this problem is a continuous tradeoff in the base isolation design process; if smaller accelerations are desired as the required performance objective, then displacements must be increased. Focusing on developing an optimized double rolling-type isolation system (RIS) capable of performance not previously achieved, the objectives of this study are to increase the displacement capacity of RISs and enhance their behavior through control techniques. This study aims to optimize the stiffness in a double RIS system to fully utilize displacement capacity and attain an adaptive behavior that permits the isolation system to be separately optimized for small displacements in a design basis event (DBE) and large displacements in a maximum considered event (MCE).

Rolling-type isolation systems constitute a practical solution for earthquake-exposed data cabinets. The protection that rolling-type isolation systems provide are comparable to other types of isolation systems, but at a lower cost with simpler installation. Studies have shown rolling-type isolation systems allow for various attributes to be altered for the specific object it is protecting. Examples include the use of bi-axial rolling configurations, cylindrical rollers, dampers, re-centering mechanisms, rolling friction, rolling profiles, and even understanding nonlinearity behavior (Naeim and Kelly, 1999). For data cabinets, it is important to keep the system's footprint as small as possible so the data center can accommodate as many cabinets as possible. The double RIS proposed would keep the system's footprint the same, while doubling displacement

capacity. The double RIS would be able to accommodate larger displacements than a single RIS, which allows for better performance in a potential severe earthquake.

The remainder of this study will discuss development of the double RIS and an optimization technique to evaluate its performance. The optimization of the double RIS will address the competing objectives of reducing accelerations at the cost of increasing displacements demands, by increasing the displacement capacity of system.

Chapter 2

Single Rolling Isolation System

2.1 Overview

In this chapter, the mathematical modeling of a single rolling isolation system (RIS) is described. The mathematical model will facilitate an evaluation of the system's performance in numerous earthquakes with varying RIS geometries and system parameters via numerical simulation. The system's equation of motion is derived via Lagrange's equation. The typical rolling profiles for the RIS are given; circular and conical slopes are described. The equation of motion for the RIS can be abbreviated to a linearized expression. Currently, friction pendulum bearings are predominantly used in practice, so the mathematical modeling for the RIS is extended to friction pendulum bearings.

2.2 Mathematical Model

Consider the isolation system shown in Fig. 2.1, which is idealized as an uni-axial system. Consider the isolation system to have equipment rigidly placed on the top layer. The kinetic energy of the system, regarding the total mass m, which includes the top frame and isolated equipment, is

$$\mathcal{T}(u, v) = \frac{1}{2}m(\dot{u}_{\mathrm{g}} + \dot{u})^2 + \frac{1}{2}m\dot{v}^2 \tag{2.1}$$

where $u_{\mathrm{g}}(t)$ is the horizontal ground displacement, $u(t)$ is the relative horizontal dis-

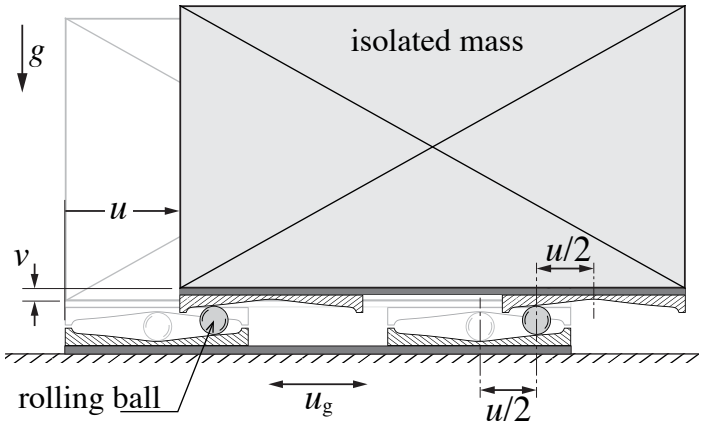

Figure 2.1: Single rolling isolation system: Geometry and displacement configuration.

placement across the isolation bearings, $v(t)$ is the relative vertical displacement along the isolation bearings and the overdot indicates differentiation with respect to time.

The potential energy in the system is only the gravitational potential energy associated with the vertical motion caused by rolling along the concave rolling surface

$$\mathcal{V}(v) = mgv \tag{2.2}$$

where m is defined earlier in the kinetic properties of the system, g is the acceleration due to gravity, and the height $v(u)$ is determined by the rolling surface profile whether it is conical (constant slope), circular, or separate functional form of $v(u)$ on a specific isolation bearing type. The above equation assumes the equipment behaves as a rigid body, where no deformation is experienced in the equipment.

The system is kinematically constrained by the rolling surface profile and can be expressed as follows:

$$f(u, v) \equiv v - h(u) = 0 \tag{2.3}$$

where the $h(u)$ is the height function dictated by the rolling profile discussed in Section 2.3.

The basic model for the isolation systems can be developed using Lagrange's equa-

tion (Greenwood, 2003):

$$\frac{d}{dt}\frac{\partial \mathcal{L}}{\partial \dot{q}} - \frac{\partial \mathcal{L}}{\partial q} = \lambda \frac{\partial f}{\partial q} \tag{2.4}$$

where the Lagrangian $\mathcal{L} = \mathcal{T} - \mathcal{V}$ and the Lagrange multiplier λ enforces the kinematic constraint f. The two (constrained) generalized coordinates of the system are $q \in \{u, v\}$. Applying Eq. (2.4) for each generalized coordinates gives

$$u: \quad m(\ddot{u}_g + \ddot{u}) = -\lambda h'(u) \tag{2.5a}$$
$$v: \quad m\ddot{v} + mg = \lambda \tag{2.5b}$$

The multiplier is found from Eq. (2.5b). The multiplier can be eliminated by substituting Eq. (2.5b) into Eq. (2.5a) to give

$$m(\ddot{u}_g + \ddot{u}) = -(m\ddot{v} + mg)h'(u) \tag{2.6}$$

Note that the vertical acceleration $\ddot{v}$ appears in the above expression are kinematically constrained per Eq. (2.3). It can be eliminated by substituting the kinematic constraints into Eq. (2.6), where the time derivative is taken twice to Eq. (2.3) to find the vertical acceleration

$$\ddot{v} = h''(u)\dot{u}^2 + h'(u)\ddot{u} \tag{2.7}$$

Substituting these expressions into Eq. (2.6), the equation of motion is

$$m(\ddot{u}_g + \ddot{u}) = -\{m[h''(u)\dot{u}^2 + h'(u)\ddot{u}] + mg\}h'(u) \tag{2.8}$$

Rearranging the equation where the forcing $\ddot{u}_g$ is by itself

$$m[1 + h'(u)]\ddot{u} + mh''(u)h'(u)\dot{u}^2 + mgh'(u) = -m\ddot{u}_g \tag{2.9}$$

This derivation will be extended for the double isolation system configuration in Chapter 4 following a similar procedure.

2.3 Typical Rolling Profiles

As previously noted, the heights $h(u)$ are dictated by the rolling surface profile $y(x)$ (see Fig. 2.2), with the functional form depending on the specific isolation bearing type. For a rolling pendulum bearing, the height is given by two times the surface profile elevation at the ball, which is half the displacement across the bearing (see Fig. 2.1):

$$h(u) = 2y(u/2) \tag{2.10}$$

Common bowl profiles $y(x)$ include circular and constant slope (Harvey et al., 2014). The former is considered here as the dynamics can easily be linearized, whereas the latter results in highly nonlinear gravitational restoring forces that will be presented later.

Circular profile. Assuming a circular profile, the elevation is given by the equation of a circle centered a distance R vertically above the origin with a radius of R, i.e.,

$$x^2 + (y - R)^2 = R^2 \tag{2.11}$$

Eq. (2.11) can be rearranged to solve for $y(x)$ as follows:

$$y(x) = R - \sqrt{R^2 - x^2} \tag{2.12}$$

The equation of motion [Eq. (2.9)] depends on the gradient and curvature of the assumed profile through the height function [Eq. (2.10)]. The gradient $y'(x)$ and curvature $y''(x)$ can be simplified by retaining the linear term in the Taylor series expansions:

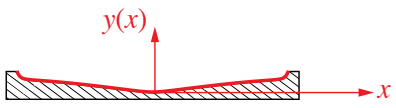

Figure 2.2: Rolling surface profile $y(x)$.

$$y'(x) = \frac{x}{(R^2 - x^2)^{1/2}} \approx \frac{x}{R} \tag{2.13}$$

$$y''(x) = \frac{R^2}{(R^2 - x^2)^{3/2}} \approx \frac{1}{R} \tag{2.14}$$

Hence, the gradients and curvatures appearing in Eq. (4.8) are given by

$$h'(u) \approx \frac{u}{2R} \text{ and } h'' \approx \frac{1}{2R} \tag{2.15}$$

Conical profile. The equation of motion for the conical slope would be considered a piece-wise function because of the transition between the constant slope and the radial sloped center profile. The motion of the ball can be parameterization as such:

$$\text{If } |x| \leq R\sin(\theta), \text{ then } \begin{cases} y(x) = R - \sqrt{R^2 - x^2} \\ y'(x) = x(R^2 - x^2)^{-1/2} \\ y''(x) = R^2(R^2 - x^2)^{-3/2} \end{cases} \tag{2.16a}$$

$$\text{If } |x| > R\sin(\theta), \text{ then } \begin{cases} y(x) = s\,|x| + R - R\sqrt{1 + s^2} \\ y'(x) = s\,\mathrm{sgn}(x) \\ y''(x) = 0 \end{cases} \tag{2.16b}$$

where u is the height of the ball when translated across the rolling surface, R is the radius of the rolling profile, s is the slope of the rolling profile ($dy/dx = s$), and θ is the angle of inclination, $\theta = \arctan(s)$.

2.4 Linear Equation of Motion

Note that even with the linearized expressions for the gradient $h'(u)$ and curvature h'' [Eq. (2.15)], the equation of motion [Eq. (2.9)] remain nonlinear due to the terms $h'^2(u)\ddot{u}$ and $h'(u)h''\dot{u}^2$. The equation of motion can be linearized if these nonlinear terms are assumed negligible, which is reasonable given that the radius R is relatively large to achieve isolation. Therefore, the linear equation of motion are as follows:

$$m\ddot{u} + m\frac{g}{2R}u = -m\ddot{u}_{\mathrm{g}} \tag{2.17}$$

Comparing this equation to a simple mass-spring system, the natural frequency is

$$\omega = \sqrt{\frac{g}{2R}} \tag{2.18}$$

which is independent of the mass, as expected in *pendulum-type* isolation systems. Also, linear viscous damping is assumed in the single RIS, parameterized by the damping ratio ζ. The damping coefficient is taken to be $c = m2\zeta\omega$, resulting in the following equation of motion:

$$m\ddot{u} + m2\zeta\omega\dot{u} + m\omega^2 u = -m\ddot{u}_g \tag{2.19}$$

A solution to the equation of motion [Eq. (2.19)] can be solved through numerical integration. The MATLAB (MathWorks, Natick, MA) command, ode45, numerically integrates the equation of motion with ease because of its adaptive step-size control when exposed to rapid changes due to impulsive behavior (i.e., earthquake loading). To use the numerical integrator, the equation of motion has to be reduced to a first-order, or state-space equation. The rows of the state space vector gives properties of the system in terms of displacement and velocity. For the single RIS model, the state vector is given by:

$$\mathbf{x}(t) = \begin{Bmatrix} u(t) \\ \dot{u}(t) \end{Bmatrix} \tag{2.20}$$

The equation of motion is expressed in state space form as follows:

$$\frac{d}{dt}\mathbf{x}(t) = \begin{bmatrix} 0 & 1 \\ -\omega^2 & -2\zeta\omega \end{bmatrix}\mathbf{x}(t) + \begin{Bmatrix} 0 \\ -1 \end{Bmatrix}\ddot{u}_g(t) \tag{2.21}$$

This procedure will be extended for the double RIS in Section 4.2.1.

2.5 Extension to Friction Pendulum Bearings

Extending the discussion to the friction pendulum bearing, the height $h(u)$ can be articulated as the surface profile elevation at the ball as a function of the displacement across the bearing. The height can be expressed similarly to Eq. (2.10) as the following mathematical expression:

$$h(u) = y(u) \tag{2.22}$$

The equation of motion for the friction pendulum bearing appears sightly different from the rolling pendulum bearing with the introduction of friction between the articulated slider and the sliding profile surface. The generalized equation of motion, via Lagrange's equation, by the second-order differential equation

$$m\ddot{u} + c\dot{u} + f_{\mathrm{f}} + mgh'(u) = -m\ddot{u}_{\mathrm{g}} \tag{2.23}$$

where c is the linear viscous damping coefficient, f_{f} is the friction force, and other terms are previously defined. The friction may be modeled as the Coulomb friction (Almazán et al., 1998), and f_{f} is taken to be $f_{\mathrm{f}} = \mu mg\,\mathrm{sgn}(\dot{u})$ where μ is the coefficient of friction. The gravitational restoring force $mgh'(u)$ depends on the gradient of the assumed profile [Eq. (2.11)] through the height function [Eq. (2.22)]. Following a similar procedure as with the rolling system, the (linearized) gravitational restoring force for the friction pendulum bearing is

$$mgh'(u) = mg\frac{u}{R} \tag{2.24}$$

Compared to the gravitational restoring force for the rolling pendulum

$$mgh'(u) = mg\frac{u}{2R} \tag{2.25}$$

the friction pendulum restoring force is twice that of the rolling pendulum.

2.6 Summary

A mathematical model for an uni-axial single RIS with a rigidly attached piece of equipment has been described. The model was derived using Lagrange's equation, which required relationships between the system's constraints and the kinematics of the ball relative to the upper and lower rolling surfaces. The kinetic energy of the system was determined by the horizontal motion of the isolation bearings relative to the ground, and the vertical motion of the top isolation bearings relative to the bottom isolation bearing. Potential energy was derived using the vertical change in height of the top bearing relative to the bottom bearing, which is dictated by the function of the location of ball along the rolling surface profile. Strain energy from the equipment was assumed to be negligible due to the equipment's rigid behavior relative to the isolation bearings. The system is kinematically constrained by the rolling surface profile, where the vertical height of the bearing is determined by the functional form of rolling surface profile. The rolling surface profile imposes the relationship between the horizontal displacement and the vertical displacement, which outlines the slope of the rolling surface that creates the restoring forces.

Typical rolling profiles discussed were circular and conical, but the circular profile was selected as the focus of this study. The circular height function's gradient and curvature was simplified using a Taylor series expansion, thus creating linearized expressions. Through more simplification to the nonlinear terms such as multiple paired gradient and curvature variables, the equation of motion was linearized to an equation similar to a simple mass-spring system.

In the next chapter, a circular uni-axial single RIS, as well as a friction pendulum system, were fabricated using 3D printers and experimentally tested. A coupled system was constructed consisting of the single degree-of-freedom (SDOF) structure and the single RIS. The free response tests were conducted to determine properties of the cou-

pled system. Using a shaker table to simulate previous notable earthquakes, the single RIS was tested under seismic loading conditions to determine the RIS's performance.

Chapter 3

Experimental Testing of a Single RIS

3.1 Overview

Chapter 2 described a mathematical model of the single rolling isolation system (RIS), which can facilitate a numerical evaluation of the system's performance under seismic loading. In this chapter, simple experimental models are fabricated using 3D printing, which provides a means to rapidly fabricate bearings for isolation systems (Calhoun and Harvey, 2018). The mechanisms for both rolling and sliding bearings are modeled, designed, fabricated, and tested to assess the influence of bearing geometry (radius) and damping (rolling resistance versus friction) on the dynamic characteristics and isolation performance.

3.2 3D Printing of Seismic Isolation Bearings

3D printing (or additive manufacturing) has increasingly been used as a teaching and research tool in mechanical engineering (Pieterse and Nel, 2016), revolutionizing the prototyping of mechanical components such as gears. More recently, 3D printing has been used to teach linear structural analysis (Virgin, 2017a) and structural dynamics (Virgin, 2017b) in the context of civil engineering. Thus, 3D printing has the capabilities of being used to teach base isolation, merging efforts from across mechanical and civil engineering disciplines. This study focuses attention on planar, pendulum-

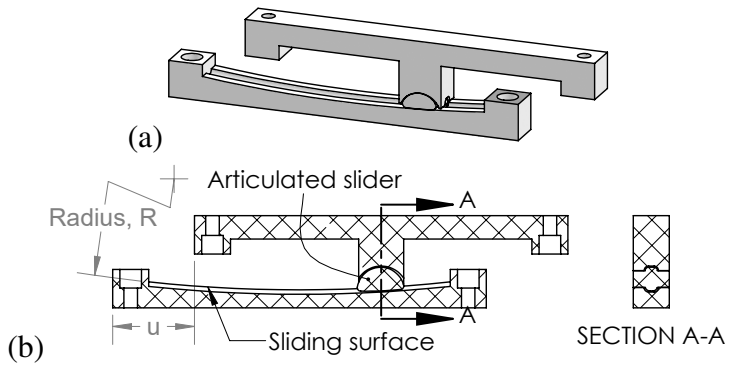

Figure 3.1: Friction pendulum bearing schematic.

type isolation bearings supporting a single-degree-of-freedom planar frame structure. Two mechanisms are considered for the isolation bearings: sliding and rolling. These mechanisms were chosen partly to facilitate 3D printing, but also due to their ubiquity in practice. This study shall focus attention on relatively simple geometries, as discussed in the following section, to obtain linear force-displacement relationships, but more complex geometries are discussed later.

3.2.1 Isolation Bearing Design and Fabrication

This study considers two typical pendulum-type isolation bearings: friction pendulum (FP) bearings and rolling pendulum (RP) bearings. Fig. 3.1 shows the design for the FP bearing, which was modeled after a common design in practice (Mosqueda et al., 2004). The bearing is comprised of a bottom plate with circular sliding surface of radius R that is attached to the ground, an upper plate that supports the structure, and an articulated slider that transfers the load between the sliding surface and the upper plate. Fig. 3.2 shows the design for the RP bearing, which is comprised of lower and upper rolling surfaces (both of radius R) and a steel ball interposed therebetween. Both of these bearings function under a pendulum-like mechanism, whereby horizontal translations result in vertical motion generating a gravitational restoring force. Details on modeling of these bearings was given in Section 2.5.

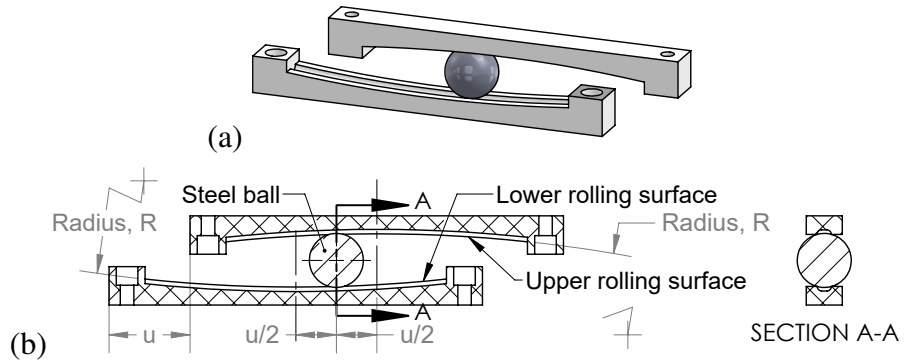

Figure 3.2: Rolling pendulum bearing schematic.

In addition to varying the isolation mechanism, the bearing radius R provided parametric variation. Two radii were fabricated and tested: $R = 254$ and 508 mm. More specific details will be given on the selection of these two values in Section 3.2.2. The sliding and rolling surfaces were designed to be interchangeable to reduce the number of surfaces that needed to be printed. Details of the sliding/rolling surfaces are shown in Fig. A.1 (see Appendix A). The surfaces had a center line groove that accommodated the articulated slider (that had a matching tongue; Fig. A.2) and the 19.1-mm steel ball (not shown), which provided resistance transverse to the bearing's intended motion. The radii of the articulated slider were selected so as to avoid binding both laterally and longitudinally. A matching groove in the upper mount of the FP bearing (Fig. A.3) was designed to allow the slider to articulate. To keep the bearing profile as thin as possible, the bearings were designed with recessed bolt holes leaving enough clearance to avoid contact at zero displacement. For the bearing component designs, the nominal displacement capacities of the FP and RP bearings are 44 and 89 mm, respectively.

The bearing components were fabricated using a relatively inexpensive 3D printer (Taz 6, LulzBot, Loveland, CO). Polylactic acid (PLA) thermoplastic was used because it tends to be more forgiving and show less warping from differential cooling than acrylonitrile butadiene styrene (ABS) thermoplastics. The 3D printer has a heated print surface to further reduce the warping. Warping was of particular concern because it

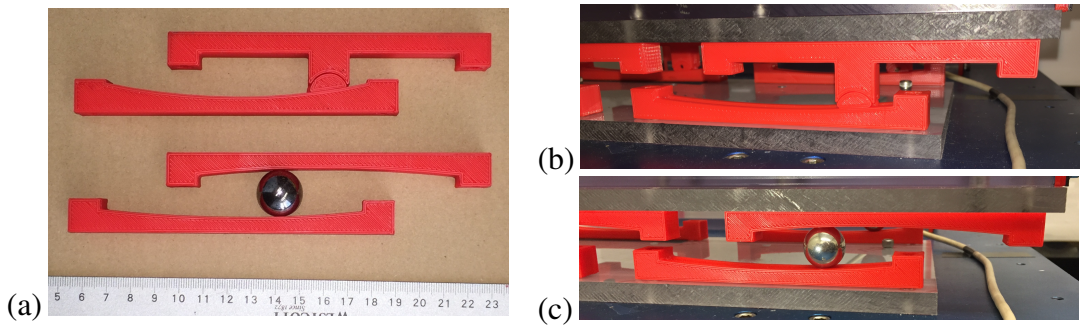

Figure 3.3: (a) Printed friction pendulum (top) and rolling pendulum (bottom) bearings. Assembled isolation bearings: (b) friction pendulum bearing; (c) rolling pendulum bearing.

would lead to misalignment in the bearings.

3.2.2 System Assembly and Setup

For the experimental system, a single-story shear-type building model was isolated using the 3D printed bearings. The fabricated bearing components are shown in Fig. 3.3(a), and the assembled isolation bearings are shown in Figs. 3.3(b) and 3.3(c). The isolation layer was assembled from two 152.4 mm × 304.8 mm polycarbonate plates to which four bearings were attached at the corners. The bottom plate was bolted to a single-axis shake table, and the top plate was bolted to the base of the building model. The base slab mass m_b is approximately 1.24 kg, which includes the upper bearing elements, the top plate, the base of the building model, one accelerometer, half the column masses, and mounting hardware. The structure mass m is approximately 0.677 kg, which includes the roof of the building model, an accelerometer, and half the column masses.

To reduce friction and wear in the FP bearings, a wet lubricant (petrolatum) was applied to the sliding surfaces. Quasi-static inclination tests were conducted to determine the static coefficient of friction. Motion was initiated at an incline of approximately 15°, which corresponds to a static coefficient of friction of 0.27. While this is substantially higher than traditional ranges for friction coefficient in self-lubricating bearing

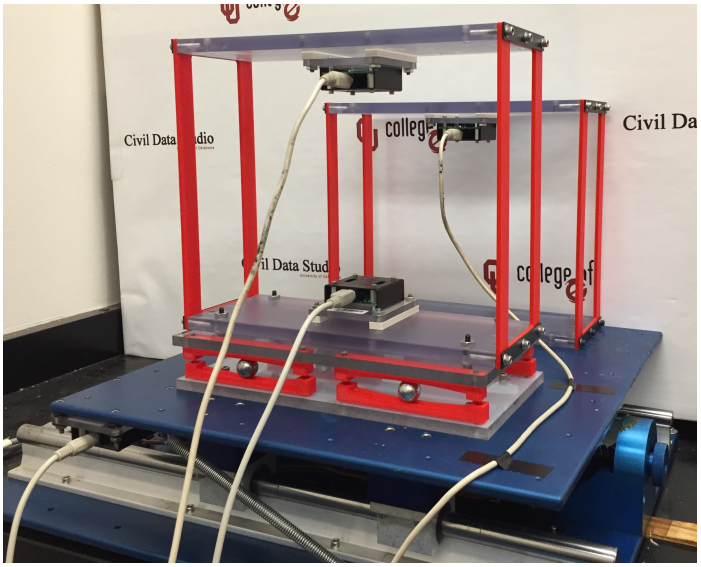

Figure 3.4: The experimental test setup. Isolated structure in foreground, with the fixed-base structure in the background. Both are attached to the shake table. Accelerometers are attached to the shake table, above the isolation layer, and to the roofs of both structures.

surfaces (0.05 – 0.15) (Constantinou et al., 1987; Bondonet and Filiatrault, 1997), other researchers have recently explored low-cost, high-friction (0.15 – 0.25) FP bearings as an approach to significantly decrease required design displacements (Jampole et al., 2014, 2016). These 3D fabricated bearings, therefore, are more representative of the latter. It is worth noting that such a high coefficient of friction will affect the sliding isolation performance, as shown later.

Fig. 3.4 shows the experimental setup. A second structure was attached directly to the shake table to serve as a point of comparison between base isolated and fixed-base buildings subject to an earthquake.

Experiments were conducted on a Quanser Shake Table II (Markham, Ontario, Canada). The Quanser table was acquired through the University Consortium on Instructional Shake Tables (Dyke et al., 2003), which was was developed to enhance undergraduate and graduate education in earthquake engineering. The table can achieve a peak acceleration of 2.5 g and has a stroke of ±75 mm. The table was controlled in *Simulink* through *QUARC* real-time control software.

An array of accelerometers was installed on the experimental system. Four accelerometers (ADXL210E, Alldata, Elk Grove, California) were installed to measure acceleration in the x direction (horizontal): one mounted underneath the stage to measure the acceleration of the shake table, one mounted immediately above the isolation layer to measure the acceleration across the isolation system, and one mounted to to roof of each structure to measure the roof acceleration. Accelerations were acquired at 1 kHz.

The rest of this chapter seeks to establish natural periods of the pendulum bearings and their geometric parameter dependence, as well as their seismic isolation performance.

3.3 Experimental Testing

Free vibration tests were first conducted to identify the experimental system properties, and then the systems were subjected to earthquake ground motions to evaluate the seismic isolation performance.

3.3.1 Free Vibration Tests

Table 3.1 gives the theoretical natural periods for the two radii considered. Note that for the two different mechanisms (sliding and rolling), the natural periods are different for the same radius R. This is due to the factor of 2 in the denominator of the restoring force [Eq. (2.25)] for the rolling pendulum bearing, which is present because of the kinematics of the rolling ball that moves half the total displacement across the bearing.

Assuming a natural period of the fixed-base structure alone of 0.182 s (the experimentally determined T_{f} described later), Eq. (1.9) can be used in conjunction with Eq. (1.8) to determine the natural periods of the coupled system. Table 3.1 gives the theoretical values for T_1 and T_2 for a mass ratio $\gamma = 0.353$ (the value determined for the experimental setup described before). The isolation period T_1 lengthens very little from

the isolation system period T_b, while the structural period is shortened by about 25%. Free vibration tests were conducted to extract the natural periods of the fixed-base structure and isolated system. Motion for the free response tests was initiated by applying an initial deflection and then releasing, and the subsequent time series was recorded by the accelerometers. Gathered data was then subject to a spectral analysis and the natural periods extracted. In particular, the natural frequency was extracted using the fast Fourier transform (FFT) within Matlab. Fig. 3.5 shows the measured free decay time series and corresponding FFT spectra for (a) the fixed-base structure and (b,c) the structure isolated with the rolling isolation system (RIS) with radius R = (b) 508 and (c) 254 mm. Note that the friction pendulum system (FPS) was not tested because the friction prevented any free vibration in the bearings.

For the fixed-base structure [Fig. 3.5(a)], the FFT gives a natural frequency of 5.497 Hz, corresponding to a period of 0.182 s (the value reported in Table 3.1 for the fixed-base structure). The natural period can alternatively be determined by picking peaks over j cycles of motion and averaging the time to complete a cycle. Doing so confirms the period of oscillation of 0.182 s. Additionally, the damping ratio ζ_f can be determined from the decrease in acceleration amplitude from $\ddot{u}_i$ to $\ddot{u}_{i+j}$ over j cycles of motion (Chopra, 2012):

Table 3.1: Isolation bearing geometries and results from free response system identification. Fixed-base structure period T_f = 0.182 s.

		Theoretical*			Experimental		
Type	R [mm]	T_b [s]	T_1 [s]	T_2 [s]	T_b [s]	T_1 [s]	T_2 [s]
Sliding	508	1.43	1.43	0.146	–	–	–
	254	1.01	1.02	0.146	–	–	–
Rolling	508	2.02	2.03	0.146	1.97	2.00	0.154
	254	1.43	1.43	0.146	1.41	1.42	0.156

*For mass ratio γ = 0.353.

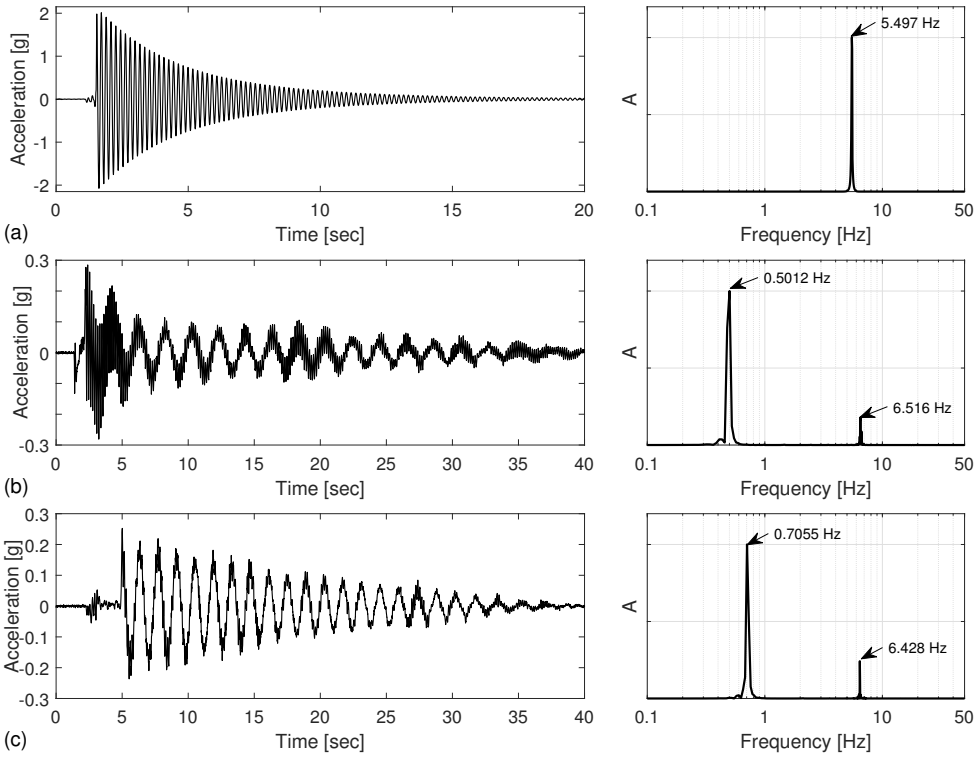

Figure 3.5: Free responses of the (a) fixed-base structure and the isolated building—(b) 508-mm RIS and (c) 254-mm RIS—and the corresponding frequency content (FFT). A is in arbitrary units.

$$\zeta \approx \frac{1}{2\pi j} \ln\left(\frac{\ddot{u}_i}{\ddot{u}_{i+j}}\right) \tag{3.1}$$

Using the logarithmic decrement approach, the damping ratio for the fixed-base structure was found to be 0.82%, confirming that the structure is very lightly damped.

For the isolated structures [Figs. 3.5(b) and 3.5(c)], two distinct frequencies can be observed in the time series and FFT, which correspond to the isolation and structural modes. For the RIS with radius $R = 508$ mm [Fig. 3.5(b)], the FFT gives natural frequencies of 0.5012 and 6.516 Hz, or natural periods of 2.00 and 0.154 s. The former is the fundamental period of the system, the isolation mode, where the structure remains effectively rigid. This value closely matches the theoretical value (Table 3.1). The latter is the structural mode, which involves deformation of the structure as well as the

isolation system. The value is sightly shorter than that of the fixed-base structure due to the frequency splitting phenomena caused by coupling the building to the isolation system. Good agreement is observed between the theoretical and experimental isolation and structural periods.

A similar behavior appears for the the 254 mm rolling isolation system. Fig. 3.5(c) shows the response of the 254 mm RIS and the isolated and structural frequencies 0.7055 and 6.428 Hz, respectively. The isolated frequency is close to the theoretical value of 0.707 Hz. It appears to be a decrease in the structural frequency value. Table 3.1 summarizes the theoretical and experimental free responses described above.

In addition to the free vibration tests of the isolated system (i.e., the isolated SDOF structure), free vibration tests were conducted on the isolation system alone by replacing the structure with rigid blocks. The free responses (not shown) gave base isolation periods T_{b} of 1.97 and 1.41 s for the RISs with radius $R = 508$ and 254 mm, respectively. These values are also reported in Table 3.1. As predicted theoretically, the base isolation period is shorter than the isolation period in the coupled system.

3.3.2 Earthquake Tests

Next, the earthquake response of the fixed-base building and isolated building with FP and RP bearings was examined to assess the seismic isolation performance. For the dynamic earthquake testing, we consider three earthquake records, which are listed in Table 3.2. The earthquake records were scaled in length and time to meet the limitations of the shake table. The time and length scale factors, peak ground acceleration (PGA), and peak ground displacement (PGD) of each record (at the 100% amplitude) are listed in Table 3.2. Additional length scales are considered in the incremental dynamic analysis (Section 3.3.2).

The ground-motion time-histories are shown in Fig. 3.6 for the three earthquake records (at the 100% amplitude). Additionally, acceleration response spectra are shown

Table 3.2: Records used for earthquake tests.

Event	Year	Station	Record	Time scale	Length scale	PGA [g]	PGD [mm]
Kobe	1995	HIK	HIK000	1/4	1/3.3	0.68	10
Northridge	1994	Sylmar - Hospital	SYL090	1/2	1/11	0.80	15
Cape Mendocino	1992	Cape Mendocino	CPM000	1/4	1/7.0	0.81	50

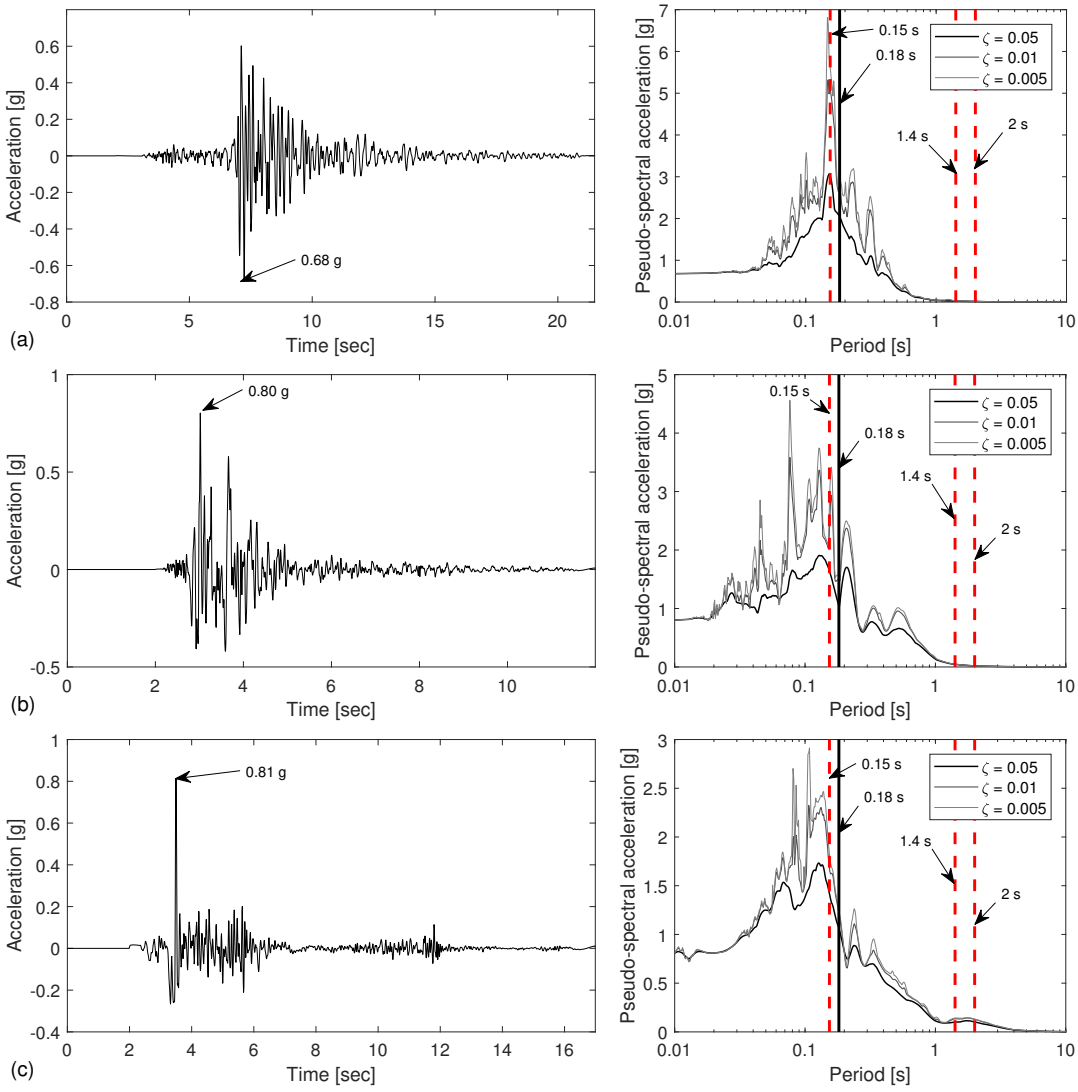

Figure 3.6: Time history of earthquakes used for evaluating the fixed base and isolation systems—(a) Kobe, (b) Northridge (c) Mendocino—and their corresponding frequency content (response spectra).

for damping ratios of $\zeta = 0.5$, 1 and 5 %. The vertical lines indicate the periods of interest for the experimental system: fixed-base period, $T_{\mathrm{f}} = 0.18$ s; base isolation periods, $T_{\mathrm{b}} = 2$ and 1.4 s; and structural-mode period of the isolated system, $T_2 = 0.15$ s. Note that T_{f} and T_2 fall within the portion of the spectrum where the energy is strongest, whereas T_{b} is in the lower energy region (by design).

Figs. 3.7 and 3.9 show the response time histories for Kobe and Mendocino at the

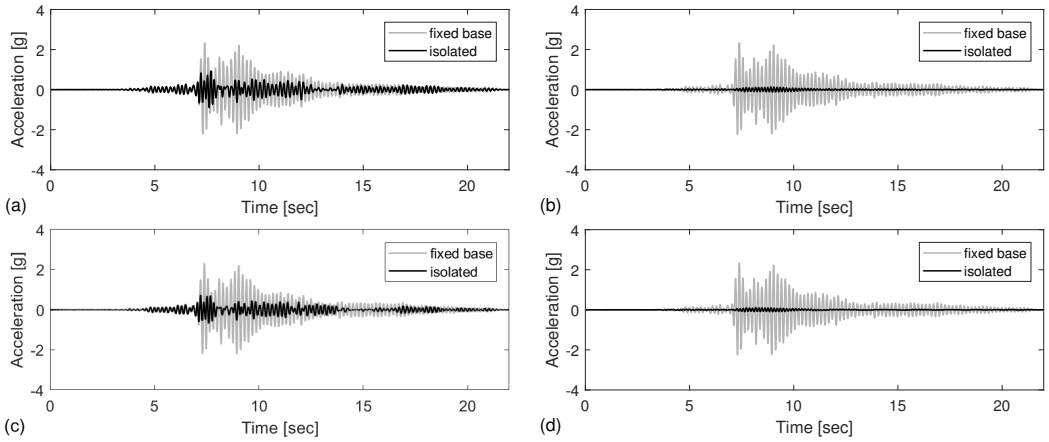

Figure 3.7: Roof acceleration response of fixed-base building and isolated buildings—(a) 254 mm FPS, (b) 508 mm RIS, (c) 508 mm FPS, and (d) 254 mm RIS—subjected to Kobe ground motion.

100% amplitude. From these figures, it is immediately apparent that the roof acceleration is considerably reduced in the isolated cases when compared to the fixed-base building. For Kobe (Fig. 3.7), reductions on the order of 60% and 90% are observed for the FP and RP bearings, respectively. The damping in the FP bearing increases the coupling and decreases the isolation performance, whereas the RP bearing is very lightly damped leading to the dramatic reduction in accelerations. In fact, the RP bearing consistently isolates throughout the entire test, while there is a portion at the beginning of the FP test in which the fixed-based and isolated buildings respond identically [e.g., time 0–7 s in Fig. 3.7(a)]. This corresponds to base shear insufficient to break the friction in the sliding bearing, with the bearing acting as rigid; it is not until the ground accelerations become sufficiently large to break friction that bearing displacements are realized and isolation is achieved. Similar response behaviors and isolation performance were observed in the case of Northridge (Fig. 3.8).

For Mendocino (Fig. 3.9), the FP bearings (a,c) exhibited similar performance as the Kobe event, but the RP bearing (b,d) exhibited much larger responses, with a distinct component of the response at the isolation period. The reason for this large isolation response can be explained from the response spectra in Fig. 3.6. Above a period of

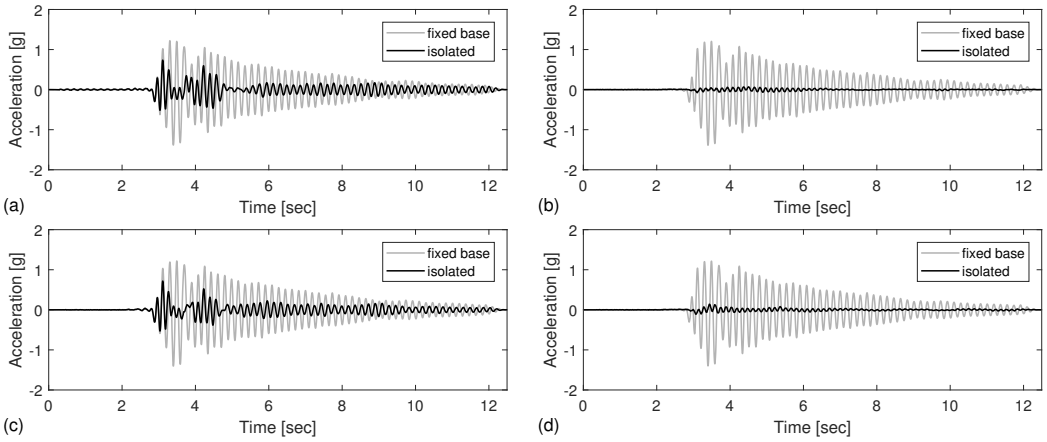

Figure 3.8: Roof acceleration response of fixed-base building and isolated buildings—(a) 254 mm FPS, (b) 508 mm RIS, (c) 508 mm FPS, and (d) 254 mm RIS—subjected to Northridge ground motion.

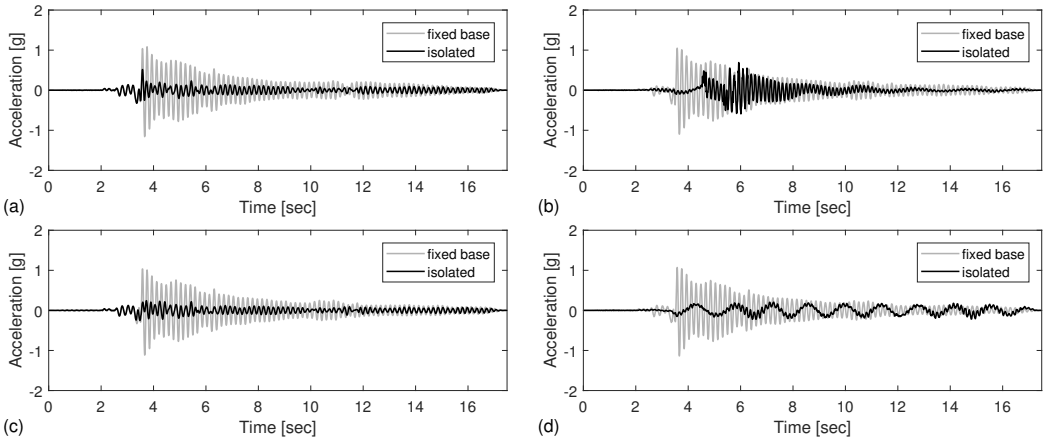

Figure 3.9: Roof acceleration response of fixed-base building and isolated buildings—(a) 254 mm FPS, (b) 508 mm RIS, (c) 508 mm FPS, and (d) 254 mm RIS—subjected to Mendocino ground motion.

1 s, Kobe (a) and Northridge (b) have nearly zero pseudo-spectral acceleration, while Mendocino exhibits a long period component in the 1–2 s range where the isolation period is located. The spectral acceleration at the isolation period is roughly 0.15 g, which matches the measured acceleration response in this case [Fig. 3.9(d)]. It is clear that the effectiveness of base isolation is diminished under long-period ground motions (Sato et al., 2011).

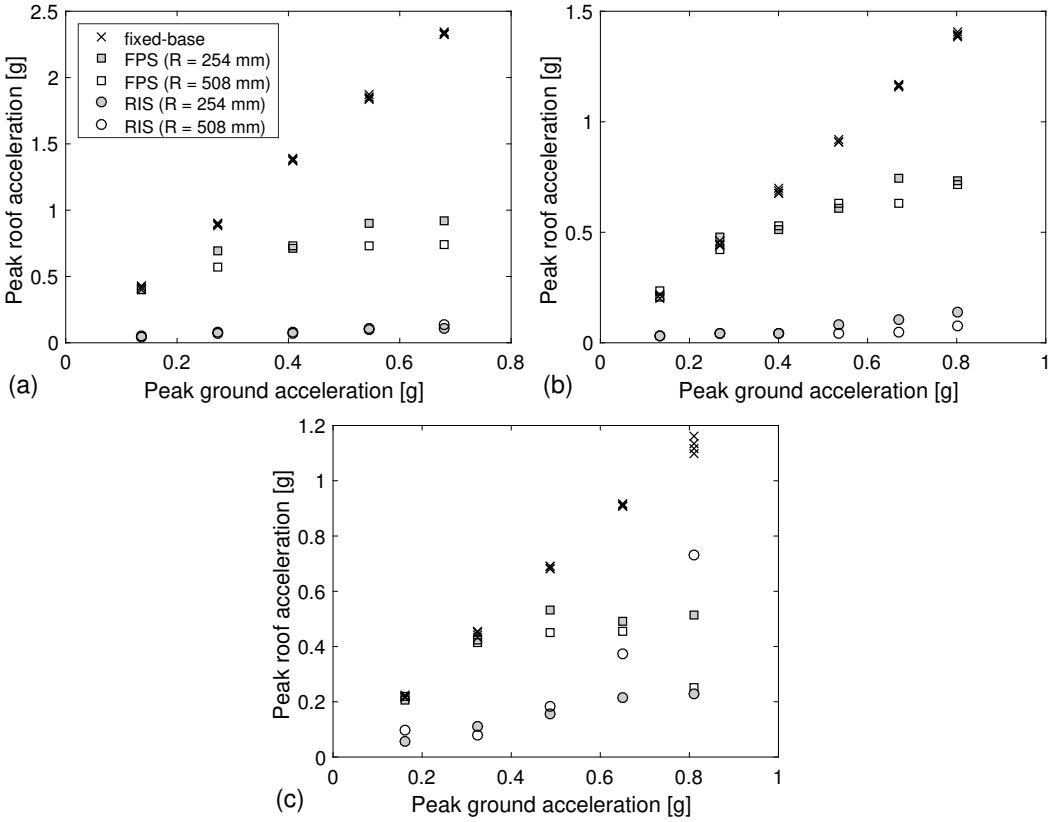

Figure 3.10: Incremental dynamic analysis. Peak roof acceleration versus peak ground acceleration for the fixed-base building and the building isolated using a friction pendulum system (FPS) or a rolling isolation system (RIS) with varying radius R: (a) Kobe, (b) Northridge, and (c) Mendocino.

Incremental Dynamic Analysis

Finally, the behavior of the systems is assessed at multiple ground-motion amplitudes. In this *incremental dynamic analysis* (Vamvatsikos and Cornell, 2002), five to six ground-motion amplitudes are considered for each earthquake, and peak responses are recorded for the fixed-base building and isolated building with each bearing. By making incremental changes to the earthquake intensity, it is then possible to gain an appreciation for nonlinearities and their effect on the systems' behavior.

Fig. 3.10 show the peak roof accelerations versus PGA for (a) Kobe, (b) Northridge, and (c) Mendocino. These figures contain a wealth of information. First, the fixed-base

structure behaves linearly as expected. With increasing PGA, the peak roof acceleration increases proportionately. This behavior is seen to be repeatable as well, as indicated by the four coincident markers at each PGA—one for each isolation configuration.

Second, the peak roof acceleration for the friction pendulum systems (FPSs) are identical to those of the fixed-base building for low PGAs. This is due to the base shear being insufficient to break friction in the bearings, not allowing deflection across the bearing, resulting in an effectively fixed-base building. The critical PGA at which friction is overcome and motion in the bearing is initiated is in the range (a) 0.136 – 0.272 g, (b) 0.268 – 0.401 g, and (c) 0.325 – 0.487 g. Neglecting any dynamic effects, the coefficient of static friction can be approximated by this critical PGA. Doing so, gives a value of about $\mu_s = 0.27$, which is consistent with the value determined by gradually inclining the system until motion ensued.

Third, the rolling isolation system (RIS) isolated effectively for all PGAs. This is due to the very low rolling resistance in these systems. The worst performance for the RIS was for Mendocino [Fig. 3.10(c)], which is attributed to the long-period content as previously discussed.

Fourth, the radius had a slight influence on the isolation performance. For example, the response of the FPS with $R = 254$ mm under Kobe [Fig. 3.10(a)] is consistently larger than with $R = 508$ mm, which is suggested by Eq. (1.3) (i.e., smaller R means a shorter period closer to the portion of the response spectrum where the energy is strongest). Similar trends are observed for the RIS under Northridge [Fig. 3.10(b)].

3.4 Summary

In this chapter, the experimental setup for a sliding and rolling isolators was described. Additive manufacturing was shown to be convenient for easy, rapid fabrication of these isolators. The results presented in this chapter validated the linearization assumption

made in Chapter 2, with the largest percent of error for experimental natural periods of the isolator within 7% of their theoretical value. As for the earthquake tests, significant reduction appeared for both the sliding and rolling bearing, especially for the rolling bearing against earthquakes with high frequency content. When the rolling bearing was tested against low frequency earthquakes (e.g., Mendocino), significant acceleration responses occurred. These types of earthquakes potentially could produce impacts that would degrade the single RIS's performance. By increasing the displacement capacity of the single isolator with a second isolator, the system could prevent severe impacts due limitations of displacement capacity. The remainder of this thesis seeks to model and validate a new type of rolling bearing—a double RIS—that has twice the capacity of its subcomponents alone.

Chapter 4

Double Rolling Isolation System

4.1 Overview

Chapter 2 details a mathematical model which predicts the dynamics properties for a single RIS of various sizes and masses. The model describes the horizontal and vertical motion of the system. Using the assumption of the large radius relative to the small displacements (similarly to a pendulum), the equations of motion can be linearized. This linearization simplifies the equations of motion, while still keeping the integrity of the system's performance. Chapter 3 verified this assumption through experimental testing. This chapter will use the same mathematical modeling procedure to construct the equations of motion for the double RIS. The equations of motion the system will be assess for the best possible performance for a white noise disturbance.

4.2 Mathematical Model

As in similar fashion in Sec. 2.2, the equation of motion for the double rolling isolation system can be derived. Consider a double rolling isolation where there are two bearings placed on one another and a rigid mass connected to the top frame.

Consider the double RIS shown in Fig. 4.1. The relative horizontal displacement across the first and second isolation layers are given by $u_1(t)$ and $u_2(t)$, respectively. The relative vertical displacements $v_1(t)$ and $v_2(t)$ are kinematically constrained by the

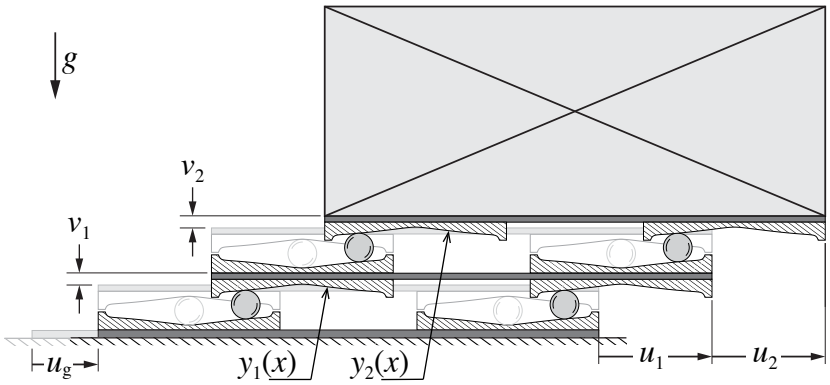

Figure 4.1: Double rolling isolation system: Geometry and displacement configuration.

rolling surface profile and depend on the bearing type. In general, these kinematic constraints can be expressed as follows:

$$f_1(u_1, v_1) \equiv v_1 - h_1(u_1) = 0 \tag{4.1a}$$
$$f_2(u_2, v_2) \equiv v_2 - h_2(u_2) = 0 \tag{4.1b}$$

where the specific form of the height functions $h_1(u_1)$ and $h_2(u_2)$ is discussed in Section 2.3.

The relevant inertial properties of the system are the masses m_1 and m_2 of the middle platform and of the top platform plus the isolated mass, respectively. The potential energy of the system is given by

$$\mathcal{V}(v_1, v_2) = m_1 g v_1 + m_2 g(v_1 + v_2), \tag{4.2}$$

and the kinetic energy is given by

$$\mathcal{T}(\dot{u}_1, \dot{v}_1, \dot{u}_2, \dot{v}_2) = \frac{1}{2} m_1 (\dot{u}_g + \dot{u}_1)^2 + \frac{1}{2} m_1 \dot{v}_1^2 + \frac{1}{2} m_2 (\dot{u}_g + \dot{u}_1 + \dot{u}_2)^2 + \frac{1}{2} m_2 (\dot{v}_1 + \dot{v}_2)^2 \tag{4.3}$$

where $u_g(t)$ is the ground displacement. Lagrange's equation is used to derive the equations of motion that satisfy the kinematic constraints [Eq. (4.1)]:

$$\frac{d}{dt}\frac{\partial \mathcal{L}}{\partial \dot{q}} - \frac{\partial \mathcal{L}}{\partial q} = \lambda_1 \frac{\partial f_1}{\partial q} + \lambda_2 \frac{\partial f_2}{\partial q} \tag{4.4}$$

where the Lagrange multipliers λ_1 and λ_2 enforce the kinematic constraints f_1 and f_2, respectively. The four (constrained) generalized coordinates of the system are $q \in \{u_1, v_1, u_2, v_2\}$. Application of Eq. (4.4) for each generalized coordinate yields

$$u_1: \quad m_1(\ddot{u}_\mathrm{g} + \ddot{u}_1) + m_2(\ddot{u}_\mathrm{g} + \ddot{u}_1 + \ddot{u}_2) = -\lambda_1 h_1'(u_1) \tag{4.5a}$$
$$v_1: \quad m_1\ddot{v}_1 + m_2(\ddot{v}_1 + \ddot{v}_2) + m_1 g + m_2 g = \lambda_1 \tag{4.5b}$$
$$u_2: \quad m_2(\ddot{u}_\mathrm{g} + \ddot{u}_1 + \ddot{u}_2) = -\lambda_2 h_2'(u_2) \tag{4.5c}$$
$$v_2: \quad m_2(\ddot{v}_1 + \ddot{v}_2) + m_2 g = \lambda_2 \tag{4.5d}$$

The multipliers λ_1 and λ_2 are immediately found from Eqs. (4.5b) and (4.5d), respectively. The multipliers can be eliminated by substituting Eqs. (4.5b) and (4.5d) into Eqs. (4.5a) and (4.5c), respectively, to give

$$\begin{aligned}(m_1 + m_2)[\ddot{u}_1 + \ddot{v}_1 h_1'(u_1)] + m_2[\ddot{u}_2 + \ddot{v}_2 h_1'(u_1)] \\ + (m_1 + m_2) g h_1'(u_1) = -(m_1 + m_2)\ddot{u}_\mathrm{g}\end{aligned} \tag{4.6a}$$
$$m_2[\ddot{u}_1 + \ddot{v}_1 h_2'(u_2)] + m_2[\ddot{u}_2 + \ddot{v}_2 h_2'(u_2)] + m_2 g h_2'(u_2) = -m_2\ddot{u}_\mathrm{g} \tag{4.6b}$$

Note that the vertical accelerations $\ddot{v}_1$ and $\ddot{v}_2$ appearing in these expressions are kinematically constrained per Eq. (4.1). They can be eliminated by substituting the kinematic constraints into Eq. (4.6), which requires Eq. (4.1) to be twice differentiated to find the vertical accelerations

$$\ddot{v}_1 = h_1''(u_1)\dot{u}_1^2 + h_1'(u_1)\ddot{u}_1 \tag{4.7a}$$
$$\ddot{v}_2 = h_2''(u_2)\dot{u}_2^2 + h_2'(u_2)\ddot{u}_2 \tag{4.7b}$$

Substituting these expressions into Eq. (4.6), the (unconstrained) equations of motion in u_1 and u_2 are

$$\begin{aligned}(m_1 + m_2)[(1 + h_1'^2)\ddot{u}_1 + h_1' h_1'' \dot{u}_1^2] + m_2[(1 + h_1' h_2')\ddot{u}_2 + h_1' h_2'' \dot{u}_2^2] \\ + (m_1 + m_2) g h_1' = -(m_1 + m_2)\ddot{u}_\mathrm{g}\end{aligned} \tag{4.8a}$$
$$m_2[(1 + h_2' h_1')\ddot{u}_1 + h_2' h_1'' \dot{u}_1^2] + m_2[(1 + h_2'^2)\ddot{u}_2 + h_2' h_2'' \dot{u}_2^2] + m_2 g h_2' = -m_2\ddot{u}_\mathrm{g} \tag{4.8b}$$

where $h_i' \equiv h_i'(u_i)$ and $h_i'' \equiv h_i''(u_i)$ for $i = 1, 2$. It is immediately apparent from these

equations that the system dynamics are inextricably tied to the specific form of these height functions, which are discussed in Section 2.3.

4.2.1 Linear Equations of Motion

Note that even with the linearized expressions for the gradients h_i' and curvatures h_i'' [Eq. (2.15)], the equations of motion [Eq. (4.8)] remain nonlinear due to the terms $h_i'h_j'\ddot{u}_j$ and $h_i'h_j''\dot{u}_j^2$. The equations of motion can be linearized if these nonlinear terms are assumed negligible, which is reasonable given that the radii R_i are relatively large to achieve isolation. Therefore, the linear equations of motion are as follows:

$$(m_1 + m_2)\ddot{u}_1 + m_2\ddot{u}_2 + \frac{(m_1 + m_2)g}{2R_1}u_1 = -(m_1 + m_2)\ddot{u}_g \tag{4.9a}$$

$$m_2\ddot{u}_1 + m_2\ddot{u}_2 + \frac{m_2 g}{2R_2}u_2 = -m_2\ddot{u}_g \tag{4.9b}$$

For the subsequent analysis and discussion, it is convenient to define the following natural frequencies:

$$\omega_1 = \sqrt{\frac{g}{2R_1}} \text{ and } \omega_2 = \sqrt{\frac{g}{2R_2}} \tag{4.10}$$

which are independent of the mass, as expected in *pendulum-type* isolation systems. Also, linear viscous damping is assumed in the two subsystems, parameterized by the damping ratios ζ_1 and ζ_2. The damping coefficients are taken to be $c_1 = (m_1 + m_2)2\zeta_1\omega_1$ and $c_2 = m_2 2\zeta_2\omega_2$, resulting in the following equations of motion:

$$(m_1 + m_2)\ddot{u}_1 + m_2\ddot{u}_2 + (m_1 + m_2)2\zeta_1\omega_1\dot{u}_1 + (m_1 + m_2)\omega_1^2 u_1 = -(m_1 + m_2)\ddot{u}_g \tag{4.11a}$$

$$m_2\ddot{u}_1 + m_2\ddot{u}_2 + m_2 2\zeta_2\omega_2\dot{u}_2 + m_2\omega_2^2 u_2 = -m_2\ddot{u}_g \tag{4.11b}$$

These equations can be expressed in matrix form as follows:

$$\mathbf{M}\ddot{\mathbf{u}}(t) + \mathbf{C}\dot{\mathbf{u}}(t) + \mathbf{K}\mathbf{u}(t) = -\mathbf{M}\boldsymbol{\iota}\ddot{u}_g(t) \tag{4.12}$$

where $\mathbf{u}(t) = \{u_1(t)\ u_2(t)\}^T$, $\boldsymbol{\iota} = \{1\ 0\}^T$, and

$$\mathbf{M} = \begin{bmatrix} m_1 + m_2 & m_2 \\ m_2 & m_2 \end{bmatrix},\ \mathbf{C} = \begin{bmatrix} (m_1 + m_2)2\zeta_1\omega_1 & 0 \\ 0 & m_2 2\zeta_2\omega_2 \end{bmatrix},\ \mathbf{K} = \begin{bmatrix} (m_1 + m_2)\omega_1^2 & 0 \\ 0 & m_2\omega_2^2 \end{bmatrix}$$

In the subsequent eigenanalysis, it is convenient to define the dimensionless mass ratio

$$\mu = \frac{m_1}{m_2} \qquad \text{(mass ratio)} \tag{4.13}$$

Note that for the system of interest (Fig. 4.1), $m_1 \ll m_2$, so μ will be small ($< 50\%$).

4.2.2 Eigenanalysis

Solving the characteristic equation, $\det(\mathbf{K} - \Omega^2\mathbf{M}) = 0$, for the natural frequencies of the coupled system, we find

$$\Omega_{1,2}^2 = \frac{1+\mu}{2\mu}\left[(\omega_1^2 + \omega_2^2) \mp \sqrt{(\omega_1^2 + \omega_2^2)^2 - 4\frac{\mu}{1+\mu}\omega_1^2\omega_2^2}\right] \tag{4.14}$$

The associated mode shapes are given by

$$\boldsymbol{\phi}_{1,2} = \left\{ \begin{array}{c} 1 \\ \dfrac{2\frac{\mu}{1+\mu}\omega_1^2 - (\omega_1^2 + \omega_2^2) \pm \sqrt{(\omega_1^2 + \omega_2^2)^2 - 4\frac{\mu}{1+\mu}\omega_1^2\omega_2^2}}{\frac{1}{1+\mu}\left[(\omega_1^2 + \omega_2^2) \mp \sqrt{(\omega_1^2 + \omega_2^2)^2 - 4\frac{\mu}{1+\mu}\omega_1^2\omega_2^2}\right]} \end{array} \right\} \tag{4.15}$$

Unlike traditional base isolation where $\omega_1 < \omega_2$ always, in the dual-layer base isolation system three configurations are equally possible: (I) $\omega_1 < \omega_2$, (II) $\omega_1 = \omega_2$, and (III) $\omega_1 > \omega_2$. To facilitate the comparison of these three cases, the following dimensionless frequency ratio is defined:

$$\nu = \omega_1/\omega_2 \equiv \sqrt{R_2/R_1} \qquad \text{(tuning frequency)} \tag{4.16}$$

In terms of ν, the three cases are given by: (I) $\nu < 1$, (II) $\nu = 1$, and (III) $\nu > 1$. The mode shapes [Eq. (4.15)] may be re-expressed in terms of ν as well:

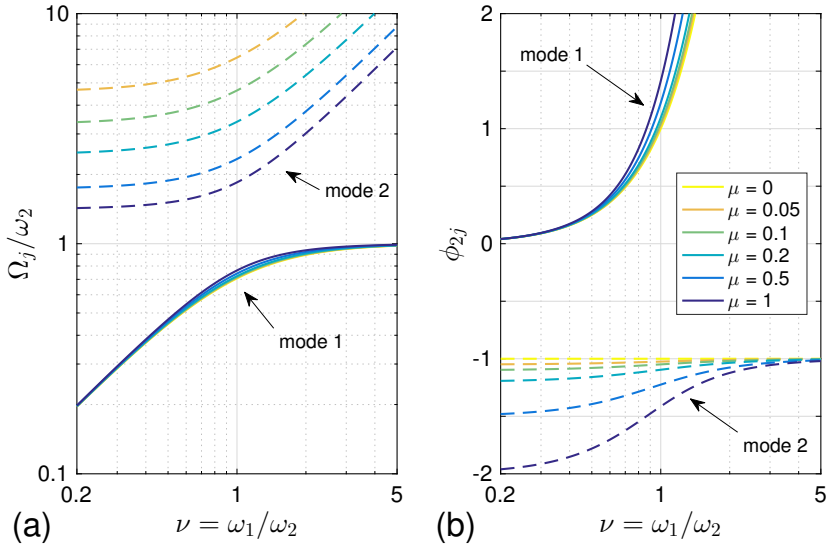

Figure 4.2: Coupled modal properties: (a) Normalized modal frequency Ω_j/ω_2 and (b) the second element of the jth mode shape, ϕ_{2j}, versus tuning frequency ν for modes 1 ($j = 1$) and 2 ($j = 2$).

$$\boldsymbol{\phi}_{1,2} = \left\{ \begin{array}{c} 1 \\ \dfrac{2\frac{\mu}{1+\mu}\nu^2 - (1+\nu^2) \pm \sqrt{(1+\nu^2)^2 - 4\frac{\mu}{1+\mu}\nu^2}}{\frac{1}{1+\mu}\left[(1+\nu^2) \mp \sqrt{(1+\nu^2)^2 - 4\frac{\mu}{1+\mu}\nu^2}\right]} \end{array} \right\} \tag{4.17}$$

The coupled modal frequencies (Ω_1 and Ω_2) normalized by ω_2 and the second element of the mode shapes (ϕ_{21} and ϕ_{22}) are shown in Fig. 4.2 for varying tuning frequency ν and mass ratio μ.

The limiting case $\mu \to 0$ is considered in additional detail here. For this case, there is zero mass in the middle platform ($m_1 = 0$), and the system reduces to a single mass (m_2) isolated by, effectively, two springs in series. The second coupled frequency blows up, $\Omega_2 \to \infty$, while the first frequency $\Omega_1^2 \to \omega_1^2\omega_2^2/(\omega_1^2+\omega_2^2) \equiv g/[2(R_1+R_2)]$. The coupled system has a lower frequency than the constituent subsystems, which is ideal for isolation performance. For the case of identical lower and upper isolators ($R_1 = R_2 \equiv R$), the effective radius is four times the radii of the subsystems, and the coupled frequency is reduced by a factor of $\sqrt{2}$. This is similar in nature to the difference between a friction

pendulum bearing and a rolling pendulum bearing described in Section 2.5. The associated mode shape $\boldsymbol{\phi}_1 = \{1, \omega_1^2/\omega_2^2\}^T \propto \{R_1, R_2\}^T$, which is advantageous as the subsystem with the larger radius would accommodate the larger displacements.

4.3 Stochastic Performance Assessment

In this section, the optimal design problem of a double RIS is posed. State space representation is used in the subsequent analysis to pose and solve the the optimal design problem. Defining the state vector $\mathbf{x}(t) = \{\mathbf{u}^T(t)\ \dot{\mathbf{u}}^T(t)\}^T$, the equations of motion [Eq. (4.11)] are expressed in state space form as follows:

$$\frac{d}{dt}\mathbf{x}(t) = \mathbf{A}\mathbf{x}(t) + \mathbf{B}\ddot{u}_{\mathrm{g}}(t) \equiv \begin{bmatrix} \mathbf{0}_{2\times2} & \mathbf{I}_{2\times2} \\ -\mathbf{M}^{-1}\mathbf{K} & -\mathbf{M}^{-1}\mathbf{C} \end{bmatrix}\mathbf{x}(t) + \begin{Bmatrix} \mathbf{0}_{2\times1} \\ -\boldsymbol{\iota} \end{Bmatrix}\ddot{u}_{\mathrm{g}}(t) \tag{4.18}$$

Details of the entries of the state matrix $\mathbf{A}$ are given here:

$$\mathbf{M}^{-1}\mathbf{K} = \frac{1}{\mu}\begin{bmatrix} (1+\mu)\omega_1^2 & -\omega_2^2 \\ -(1+\mu)\omega_1^2 & (1+\mu)\omega_2^2 \end{bmatrix}, \quad \mathbf{M}^{-1}\mathbf{C} = \frac{1}{\mu}\begin{bmatrix} (1+\mu)2\zeta_1\omega_1 & -2\zeta_2\omega_2 \\ -(1+\mu)2\zeta_1\omega_1 & (1+\mu)2\zeta_2\omega_2 \end{bmatrix}$$

where the mass ratio μ is defined in Eq. (4.13).

In practice, the ground acceleration $\ddot{u}_{\mathrm{g}}(t)$ cannot be known *a priori*. For designing the double RIS, the ground motion can be modelled by a stationary stochastic process with power spectral density (PSD) denoted $S(\omega)$. Initially, the excitation is assumed to be a white-noise process having a constant PSD $S(\omega) = S_o$. This model is an approximation for broadband ground motions, making the results independent of the specifics of the input ground motion. Then, a more informative PSD is used, based on the well-known Kanai-Tajimi spectrum (Kanai, 1957; Tajimi, 1960):

$$S(\omega) = S_o \frac{\omega_{\mathrm{g}}^4 + 4\zeta_{\mathrm{g}}^2\omega_{\mathrm{g}}^2\omega^2}{(\omega_{\mathrm{g}}^2 - \omega^2)^2 + 4\zeta_{\mathrm{g}}^2\omega_{\mathrm{g}}^2\omega^2} \tag{4.19}$$

where ω_{g} and ζ_{g} are characteristic ground frequency and damping ratio, respectively. Eq. (4.19) can be used to represent different spectral density shapes by proper selec-

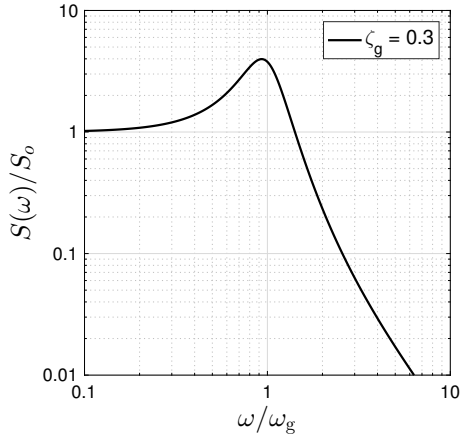

Figure 4.3: Kanai-Tajimi power spectral density $S(\omega)$ for $\zeta_g = 30\%$.

tion of ω_g and ζ_g. Fig. 4.3 shows the general shape of the Kanai-Tajimi spectrum for $\zeta_g = 30\%$. The Kanai-Tajimi spectrum has been widely used in studies of tuned mass dampers (TMDs) for seismic applications (Hoang et al., 2008; Fu and Johnson, 2011).

As the total acceleration of the isolated mass m_2 is of primary concern in this study, the first output of interest is

$$a^t(t) = \ddot{u}_g(t) + \ddot{u}_1(t) + \ddot{u}_2(t) \qquad \text{(total horizontal acceleration)} \tag{4.20}$$

Also of interest are the relative displacements across each of the isolation layers, $u_1(t)$ and $u_2(t)$. Each output can be expressed in state space form,

$$\mathsf{y}(t) = \mathbf{C}\mathbf{x}(t) \tag{4.21}$$

where the output vector is given by

$$\mathbf{C} = \begin{cases} \{0 & -\omega_2^2 & 0 & -2\zeta_2\omega_2\}, & \text{total horizontal acceleration } a^t \\ \{1 & 0 & 0 & 0\}, & \text{displacement } u_1 \\ \{0 & 1 & 0 & 0\}, & \text{displacement } u_2 \end{cases} \tag{4.22}$$

The goal is to minimize the variance of each output under random ground excitation with PSD $S(\omega)$. The variance of output y is given by

$$\sigma_{\mathrm{y}}^2 = \int_{-\infty}^{+\infty} |H(\omega)|^2 S(\omega)\,\mathrm{d}\omega \tag{4.23}$$

where $H(\omega)$ is the complex transfer function. The transfer function $H(\omega)$ is given by

$$H(\omega) = \mathbf{C}(\mathrm{j}\omega\mathbf{I} - \mathbf{A})^{-1}\mathbf{B} \tag{4.24}$$

where $\mathrm{j} = \sqrt{-1}$. The transfer function $H(\omega)$ for the system described by Eqs. (4.18) and (4.21) is

$$H(\omega) = \frac{-\mathrm{j}\omega^3 B_3 - \omega^2 B_2 + \mathrm{j}\omega B_1 + B_0}{\omega^4 A_4 - \mathrm{j}\omega^3 A_3 - \omega^2 A_2 + \mathrm{j}\omega A_1 + A_0} \tag{4.25}$$

where

$$A_0 = \omega_1^2\omega_2^2, \quad A_1 = (2\zeta_1\omega_2 + 2\zeta_2\omega_1)\omega_1\omega_2 \tag{4.26a}$$

$$A_2 = 4\zeta_1\zeta_2\omega_1\omega_2 + \omega_1^2 + \omega_2^2, \quad A_3 = 2\zeta_1\omega_1 + 2\zeta_2\omega_2, \quad A_4 = \frac{\mu}{1+\mu} \tag{4.26b}$$

For total horizontal acceleration a^{t}:

$$B_0 = \omega_1^2\omega_2^2, \quad B_1 = (2\zeta_1\omega_2 + 2\zeta_2\omega_1)\omega_1\omega_2, \quad B_2 = 4\zeta_1\zeta_2\omega_1\omega_2, \quad B_3 = 0 \tag{4.27}$$

For displacement u_1:

$$B_0 = -\omega_2^2, \quad B_1 = -2\zeta_2\omega_2, \quad B_2 = -\frac{\mu}{1+\mu}, \quad B_3 = 0 \tag{4.28}$$

For displacement u_2:

$$B_0 = -\omega_1^2, \quad B_1 = -2\zeta_1\omega_1, \quad B_2 = 0, \quad B_3 = 0 \tag{4.29}$$

4.3.1 Baseline Scenario – Single RIS

To investigate the effect of the double RIS in reducing the acceleration demands on the isolated mass and displacement demands on the isolators, the response ratio $\sigma_{\mathrm{y}}^2/(\sigma_{\mathrm{y}}^2)_{\omega_i}$ is considered, where $(\sigma_{\mathrm{y}}^2)_{\omega_i}$ denotes the variance of the response of the isolated mass in

a single RIS configuration with natural frequency ω_i ($= \sqrt{g/2R_i}$) and damping ratio ζ_i:

$$\ddot{u} + 2\zeta_i\omega_i\dot{u} + \omega_i^2 u = -\ddot{u}_g \tag{4.30}$$

For this baseline single RIS configuration, the relevant transfer functions can easily be shown to be

$$H(\omega) = \frac{1}{(\omega_i^2 - \omega^2) + 2\zeta_i\omega_i\omega\mathrm{j}} \begin{cases} 2\zeta_i\omega_i\omega\mathrm{j} + \omega_i^2, & \text{total horiz. acceleration } a^{\mathrm{t}} \\ 1, & \text{displacement } u \end{cases} \tag{4.31}$$

In going from the single RIS to a double RIS, two scenarios need to be considered: inserting a second isolation layer above (*Scenario A*) or below (*Scenario B*) the baseline single RIS. The total acceleration performance is benchmarked to the baseline single RIS; i.e., the acceleration response ratios $\sigma^2_{a^{\mathrm{t}}}/(\sigma^2_{a^{\mathrm{t}}})_{\omega_1}$ is used for scenario A, while the acceleration response ratios $\sigma^2_{a^{\mathrm{t}}}/(\sigma^2_{a^{\mathrm{t}}})_{\omega_2}$ is used for scenario B. Conversely, the relative displacement performances are benchmarked to a single RIS with the frequency of the isolation layer; i.e., the response ratios $\sigma^2_{u_1}/(\sigma^2_u)_{\omega_1}$ and $\sigma^2_{u_2}/(\sigma^2_u)_{\omega_2}$ are used for both scenarios. The parameters to be studied are the tuning frequency ω_1/ω_2 [Eq. (4.16)] and the mass ratio m_1/m_2 [Eq. (4.13)]. For all analyses, the damping ratios are taken to be 2% (Harvey and Gavin, 2013), which is representative of a lightly damped RIS (i.e., steel balls on steel rolling surfaces).

4.4 Results and Discussion

4.4.1 White Noise

In this section, a broadband (white noise) excitation is considered, i.e., $S(\omega) = S_o$. Figs. 4.4 and 4.5 show the manifolds of the normalized output variances (response ratios) for scenarios A and B, respectively, with varying tuning frequency and mass ratio.

The total acceleration manifolds [Figs. 4.4(a) and 4.5(a)] depict the variance of a^{t} for the double RIS, denoted $\sigma^2_{a^{\mathrm{t}}}$, normalized by the variance of a^{t} for a single RIS with

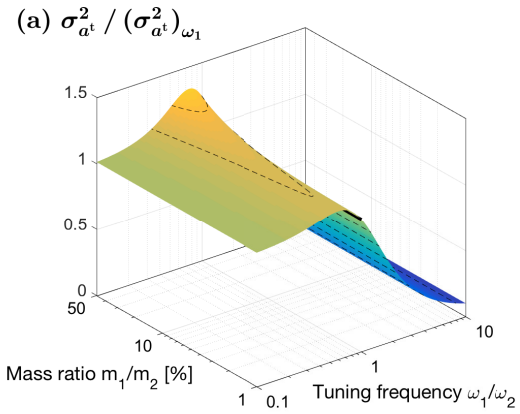

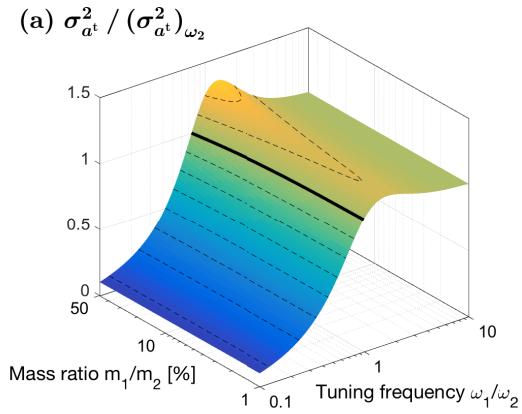

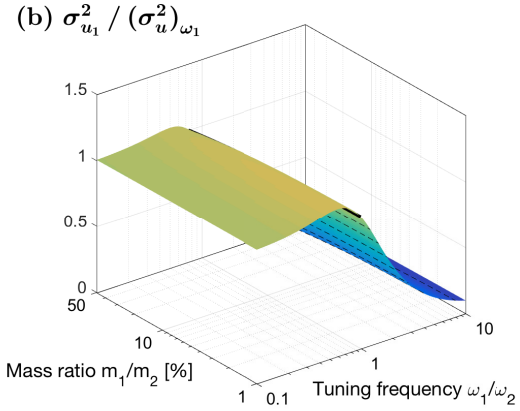

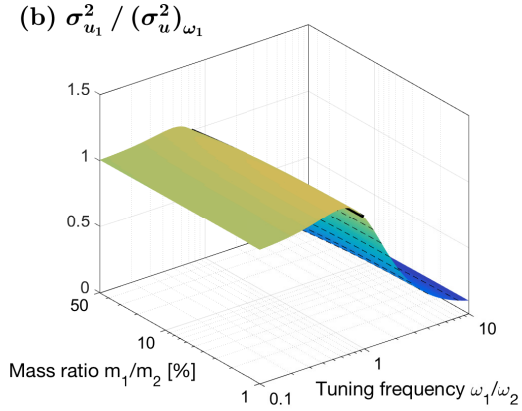

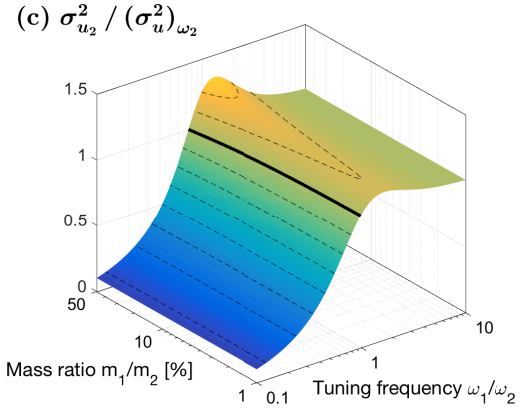

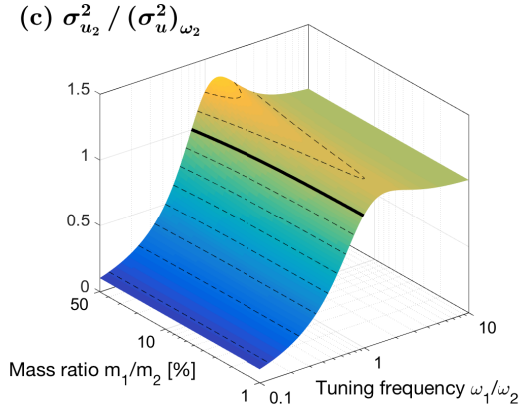

Figure 4.4: Response ratio manifolds for Scenario A (ω_1 fixed) under white noise with varying tuning frequency and mass ratio: (a) total acceleration a^t, (b) displacement u_1, and (c) displacement u_2.

Figure 4.5: Response ratio manifolds for Scenario B (ω_2 fixed) under white noise with varying tuning frequency and mass ratio: (a) total acceleration a^t, (b) displacement u_1, and (c) displacement u_2.

frequency ω_1 (scenario A) or ω_2 (scenario B), respectively. These manifolds are mirror images of each other about $\omega_1/\omega_2 = 1$, which is due to ω_1 and ω_2 always appearing together in the transfer function [see Eqs. (4.26) and (4.27)] (if $\zeta_1 = \zeta_2$). Accelerations are generally reduced (response ratio < 1) when a lower frequency isolator is introduced into the system (e.g., $\omega_1/\omega_2 > 1$ for scenario A), as expected. Conversely, when the introduced isolator has a higher frequency, the acceleration is amplified (response ratio > 1). In the limit when the introduced frequency is significantly higher (e.g., $\omega_1/\omega_2 \gg 1$ for scenario B), the response ratio approaches unity; this is because the introduced system is effectively rigid and the coupled system behaves as a single RIS.

The displacement manifolds depict the variance of u_1 [Figs. 4.4(b) and 4.5(b)] and u_2 [Figs. 4.4(c) and 4.5(c)] for the double RIS, denoted $\sigma^2_{u_1}$ and $\sigma^2_{u_2}$, normalized by the variance of u for a single RIS with frequencies ω_1 and ω_2, respectively. The displacement manifolds are identical for the two scenarios considered. In general, better displacement performance is achieved within a given isolation layer when the frequency of the other layer is smaller (e.g., u_1 at $\omega_1/\omega_2 > 1$).

On all of the manifolds, the thick black line indicates a unit response ratio, below which the double RIS outperforms the single RIS. Figs. 4.6 and 4.7 illustrate these regions of enhanced performance for the two scenarios. For a given scenario, there exists no regions where enhanced performance is simultaneously realized for all three responses (a^{t}, u_1, and u_2). Note, however, that the performance boundary (thick black line) for all three normalized variances asymptote to a frequency ratio of one as the mass ratio approaches zero. Only at a perfectly tuned system ($\omega_1/\omega_2 = 1$) with mass $m_1 = 0$ will the performance in each response be equal to the comparable single RIS, but never better. Therefore, the double RIS provides no improvements in performance over a single RIS when the disturbance is white noise (or broadband). This assumption of broadband disturbance is relaxed in the following section, where information about

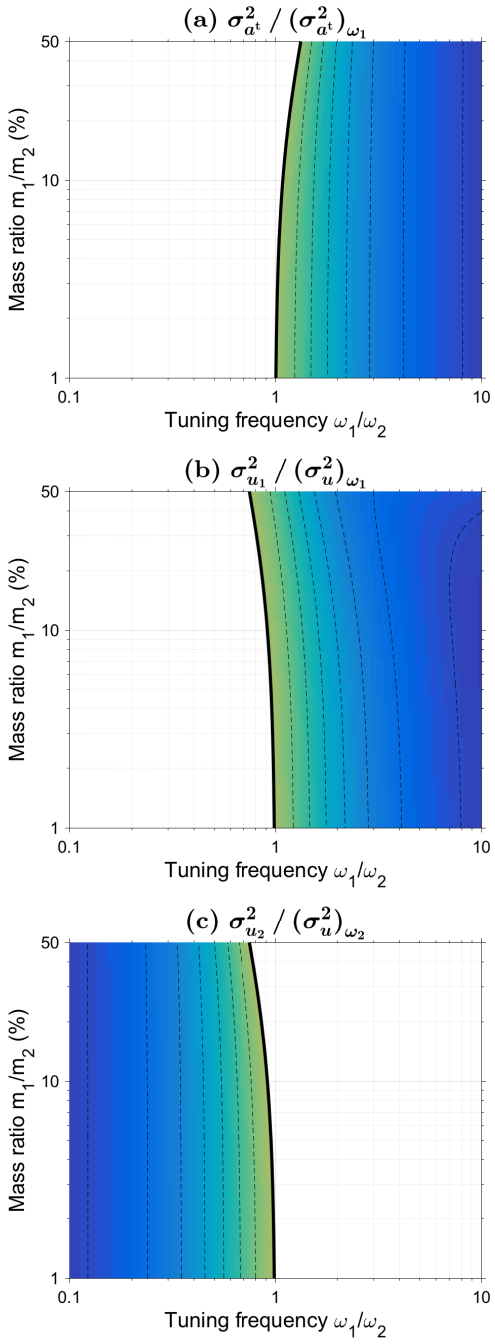

Figure 4.6: Regions of enhanced performance for Scenario A (ω_1 fixed) under white noise: (a) total acceleration a^t, (b) displacement u_1, and (c) displacement u_2.

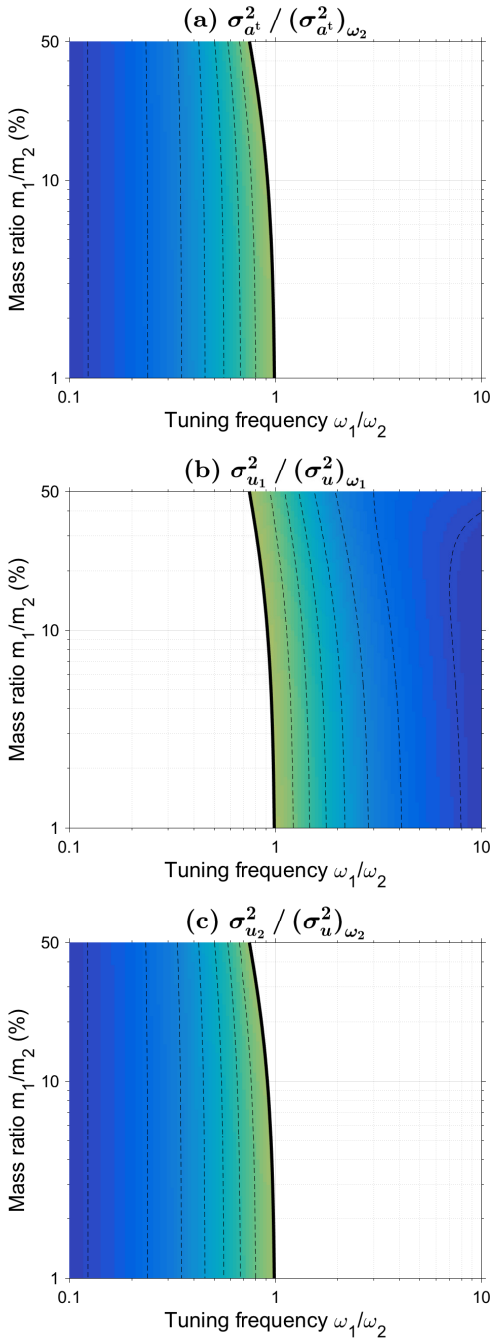

Figure 4.7: Regions of enhanced performance for Scenario B (ω_2 fixed) under white noise: (a) total acceleration a^t, (b) displacement u_1, and (c) displacement u_2.

the disturbance is introduced through the Kanai-Tajimi spectrum.

4.4.2 Kanai-Tajimi Spectrum

In this section, a random disturbance characterized by the Kanai-Tajimi spectrum [Eq. (4.19)] is considered. The characteristic ground damping ratio ζ_g is taken to be 30%, which captures well the dispersion of historical seismic events such as the N-S component recorded at the Kobe Japanese Meteorological Agency (JMA) station during the Hyogo-ken Nambu earthquake of January 17, 1995 and the simulated ground motion using fault rupture model for seismic retrofit design of Minoto Bridge (Hoang et al., 2008). The specific value of the characteristic ground frequency ω_g does not matter. Instead, only the ratio of the isolator's frequency to the ground frequency matters. It is convenient, therefore, to introduce the following dimensionless parameter:

$$\lambda = \omega_g/\omega_i \qquad \text{(ground frequency ratio)} \tag{4.32}$$

where ω_i is the natural frequency of the baseline single RIS [Eq. (4.30)] from which the double RIS is to be built. Similar scenarios apply here: Scenario A where $\omega_1 \leftarrow \omega_g/\lambda$ and ω_2 varies, and Scenario B where $\omega_2 \leftarrow \omega_g/\lambda$ and ω_1 varies.

Figs. 4.8 and 4.9 show the manifolds of the normalized output variances (response ratios) for scenarios A and B, respectively, under Kanai-Tajimi spectrum with a ground frequency ratio λ of 2. Similar trends to the white noise disturbance (Figs. 4.4 and 4.5) are observed. Differences include (1) a (relative) reduction in the acceleration response ratio [Figs. 4.8(a) and 4.9(a)] when a higher frequency isolator is introduced into the system (e.g., $\omega_1/\omega_2 < 1$ for scenario A) and (2) significantly degraded displacement performance when the frequency of the added isolator becomes large [e.g., see Figs. 4.8(c) and 4.9(b)].

Figs. 4.10 and 4.11 illustrate the regions of enhanced performance for the two scenarios. Unlike for white noise, the enhanced performance boundaries (thick black line

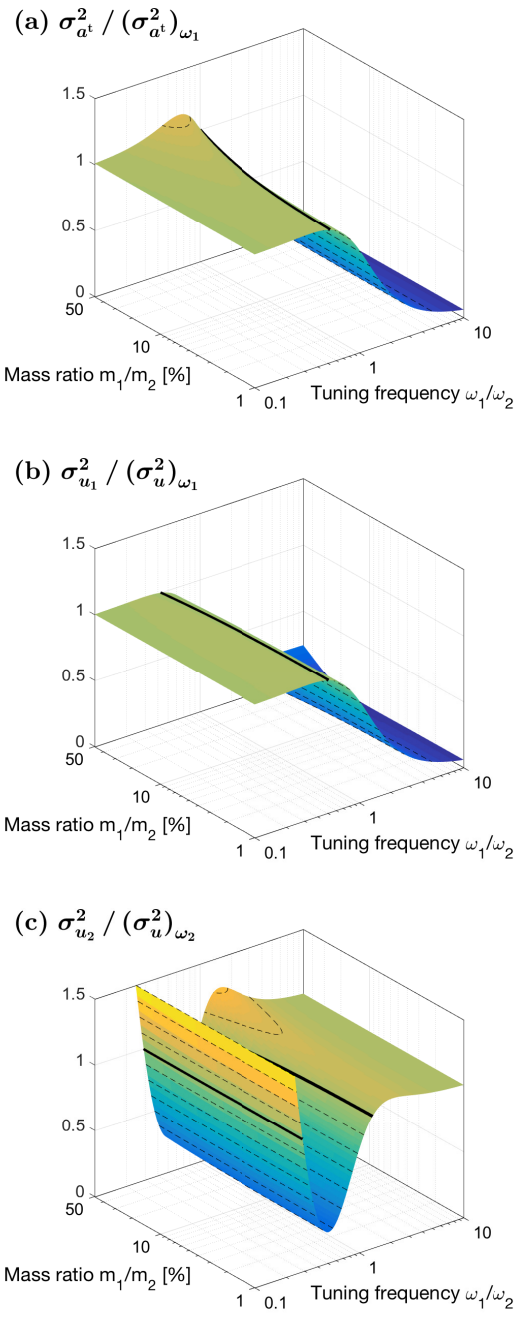

Figure 4.8: Response ratio manifolds for Scenario A ($\omega_1 = \omega_g/2$) under Kanai-Tajimi spectrum ($\zeta_g = 30\%$) for ground frequency ratio $\lambda = 2$ with varying tuning frequency and mass ratio: (a) total acceleration a^t, (b) displacement u_1, and (c) displacement u_2.

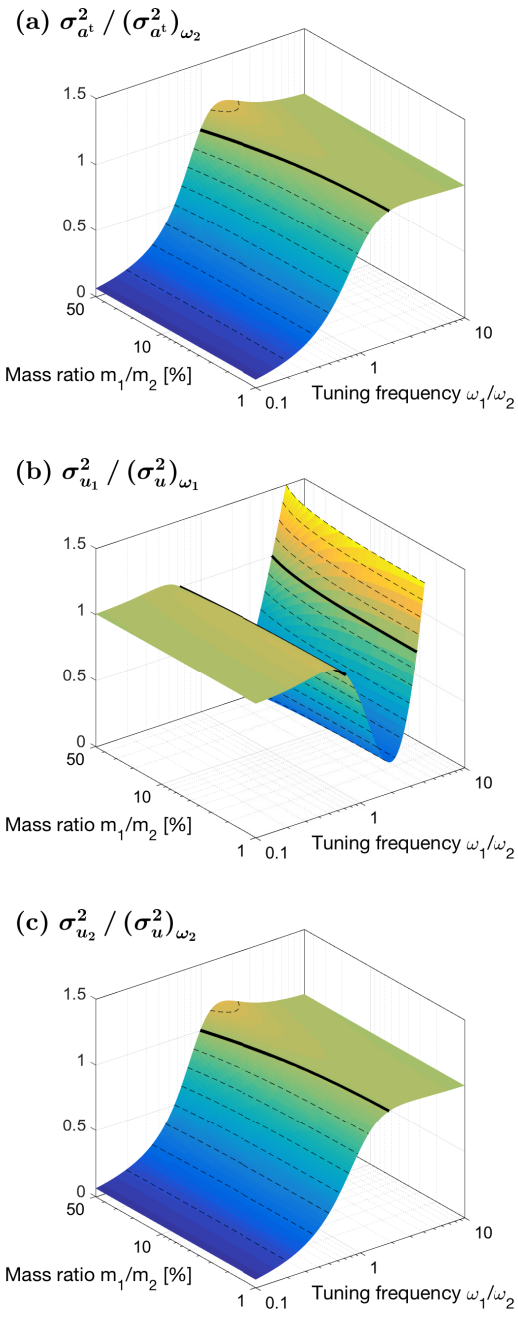

Figure 4.9: Response ratio manifolds for Scenario B ($\omega_2 = \omega_g/2$) under Kanai-Tajimi spectrum ($\zeta_g = 30\%$) for ground frequency ratio $\lambda = 2$ with varying tuning frequency and mass ratio: (a) total acceleration a^t, (b) displacement u_1, and (c) displacement u_2.

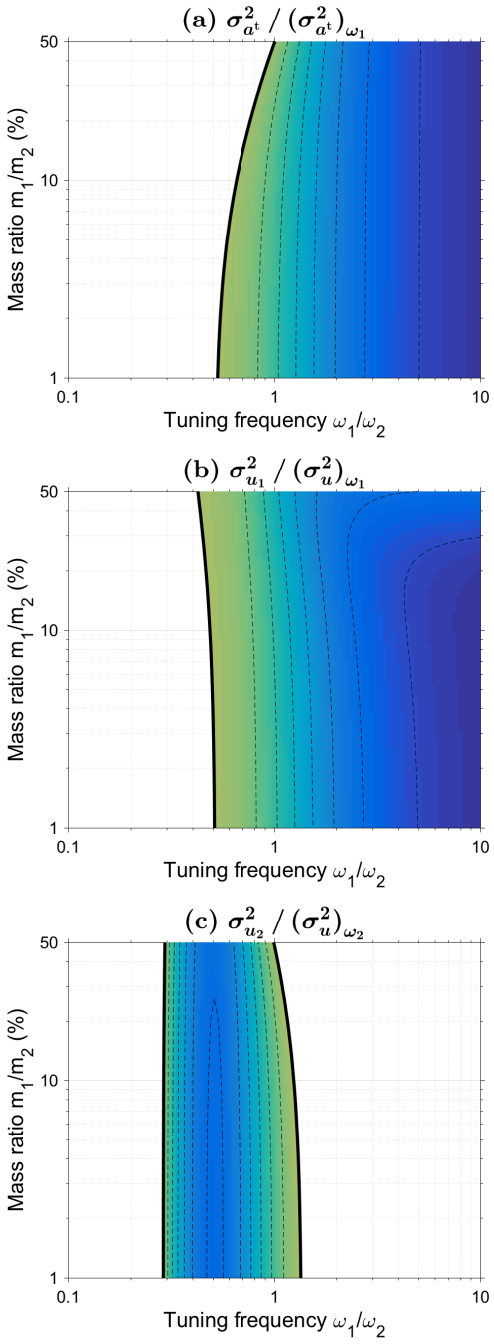

Figure 4.10: Regions of enhanced performance for Scenario A ($\omega_1 = \omega_g/2$) under Kanai-Tajimi spectrum ($\zeta_g = 30\%$) for ground frequency ratio $\lambda = 2$: (a) total acceleration a^t, (b) displacement u_1, and (c) displacement u_2.

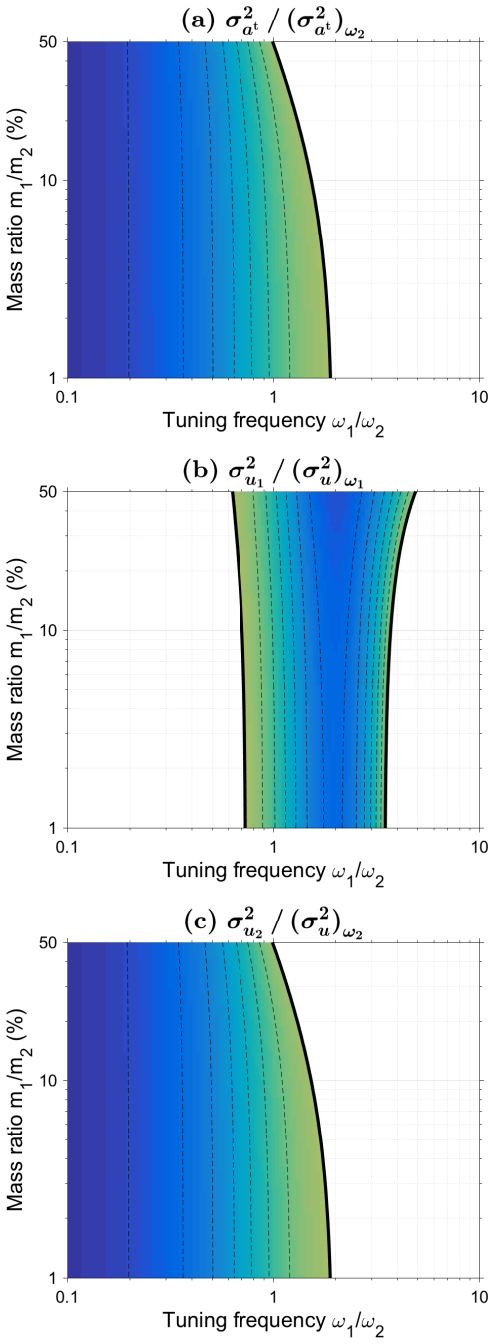

Figure 4.11: Regions of enhanced performance for Scenario B ($\omega_2 = \omega_g/2$) under Kanai-Tajimi spectrum ($\zeta_g = 30\%$) for ground frequency ratio $\lambda = 2$: (a) total acceleration a^t, (b) displacement u_1, and (c) displacement u_2.

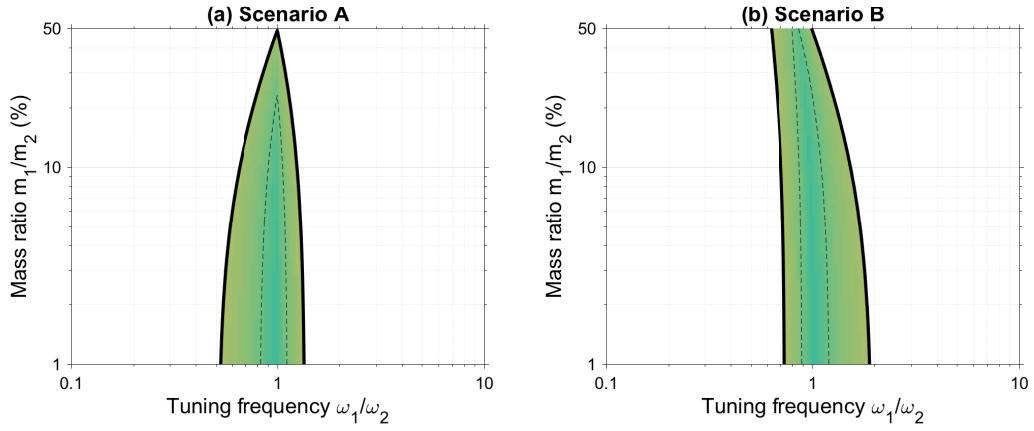

Figure 4.12: Regions of enhanced performance for all three outputs under Kanai-Tajimi spectrum ($\zeta_g = 30\%$) for ground frequency ratio $\lambda = 2$: (a) Scenario A, $\omega_1 = \omega_g/2$; (b) Scenario B, $\omega_2 = \omega_g/2$.

corresponding to unit response ratio) do *not* asymptote to a frequency ratio of one as the mass ratio approaches zero. In fact, there is a region in the (ν,μ)-plane where the enhanced domains for all three metrics overlap. This region is shown in Fig. 4.12 for the two scenarios. This figure shows that the double RIS performs better than the single RIS over certain combinations of tuning frequency and mass ratio. In general, the region is centered about a tuning frequency of one ($\omega_1/\omega_2 = 1$). Better performance is observed at lower mass ratio, as dictated by the width of the region, which indicates that the double RIS is more robust to mistuning at low mass ratios.

Up to now, a single ground frequency ratio has been considered ($\lambda = 2$). Similar enhanced performance regions can be drawn for other ground frequency ratios λ. Fig. 4.13 shows the boundaries of the enhanced performance regions for a range of ground frequency ratios. The areas within these boundaries constitute the desired design domain. This domain shrinks as the tuning frequency increases, which is equivalent to assuming a white noise disturbance due to the nearly constant PSD at low frequencies (see Fig. 4.3). For scenario A [Fig. 4.13(a)] the design domain diminishes in terms of both tuning frequency (width) and mass ratio (height), whereas for scenario B [Fig.

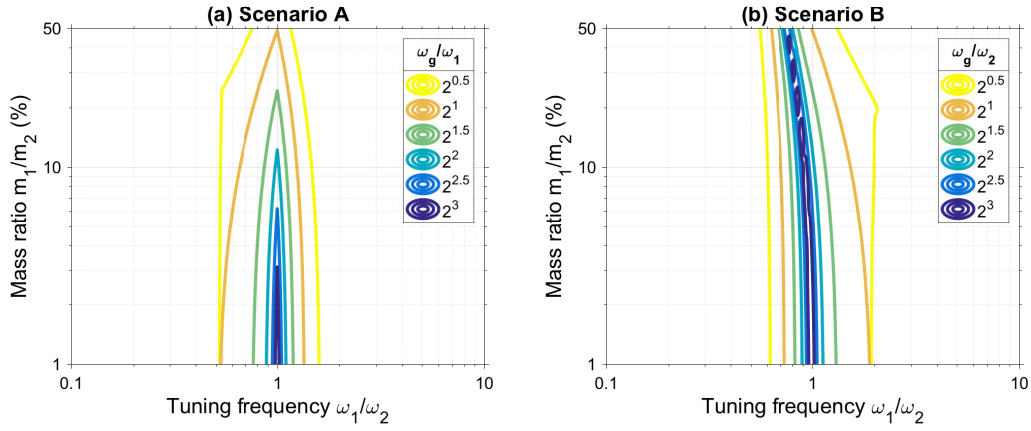

Figure 4.13: Enhanced performance boundaries under Kanai-Tajimi spectrum ($\zeta_g = 30\%$) for varying ground frequency ratio λ: (a) Scenario A, ω_g/ω_1 fixed; (b) Scenario B, ω_g/ω_2 fixed.

4.13(b)] the design domain is constricted width-wise (tuning frequency) but does not shrink height-wise (mass ratio).

4.5 Summary

In this chapter, the mathematical model developed for the single RIS was extended to the double RIS. The nonlinear equations of motion were linearized under the small angle approximation used for pendulums. The equations of motion were recast in state-space form, which was used to formulate the transfer function for three outputs (responses) of interest: total acceleration and the displacement across each isolation layer. Response variances were dictated by the disturbance power spectral density (PSD) that was multiplied by the transfer function. Two forms of the PSD were considered: broadband (constant) or an earthquake-like motion (Kanai-Tajimi). The stochastic response was quantified using the H_2 norm by numerically integrating over all possible frequencies. For verification purposes, a baseline single RIS was considered. The baseline single RIS benchmarked whether or not the double RIS was the preferred option in design. Two scenarios outlined the optimal setup configuration of the double RIS: adding a second isolation layer above (A) or below (B) the baseline single RIS.

Trends found for the broadband excitation include when an lower frequency (softer) isolator was introduced the acceleration were generally attenuated, but when a high frequency isolator was introduce the acceleration were generally amplified. White noise (broadband) excitations did not show any evidence of a double RIS being more suitable than a single RIS. Conversely, the Kanai-Tajimi spectrum showed regions of improved performance over the single RIS. The Kanai-Tajimi is more representative of a possible earthquake compared to a broadband excitation. In the next chapter, a deterministic analysis will be performed to further analyze the double RIS's performance subject to a nonstationary seismic excitation.

Chapter 5

Assessment of Double RIS

5.1 Overview

The purpose of this thesis is to evaluate and design a double rolling isolation system (RIS) that properly protects nonstructural components, more specifically network equipment systems, from physical harm due to external disturbances such as earthquakes. Telecommunication equipment protection is a relatively new field within earthquake engineering. In recent years, there has been more development in the design of these systems due the growth of modern society's dependence on telecommunications. This chapter is geared to assist practicing engineers in the field of structural and nonstructural components design with the ability to effectively design protective systems for critical equipment such as electronic/electrical cabinets. Simulations of a single RIS and double RIS subjected to an industry standard waveform will be performed, and the results will be discussed.

5.2 Telecommunications Equipment Standards

5.2.1 GR-63-CORE

The Generic Requirement (GR) document, GR-63-CORE, published by Telcordia Technologies (2012) details requirement on spatial features of equipment-building interfaces

and environmental performance criteria. This generic criteria helps to illustrate natural stresses telecommunications equipment may be exposed to and how to mitigate possible damage with suitable protection. Telcordia and industry representatives developed the criteria, and they believe the industry's compliance to the requirements will help telecommunications systems become more robust, more simplified with installation, and further improve economical planning and engineering of spaces (Telcordia Technologies, 2012).

When telecommunications equipment is subjected to motion during an earthquake, over-stressing to the equipment's framework, circuit boards, and connectors may result. The amount of motion and resulting stress depends on the structural properties of the building and framework that houses the equipment, as well as the strength of the earthquake. To properly ensure the protection of telecommunication systems in actual earthquakes, preliminary testing needs to be done to establish a baseline of their performance against previous earthquakes. The severity of the test depends on the designated network facility location for the equipment. Fig. 5.1 shows the map of earthquake risk zones according to the GR-63-CORE standard. Zone 4 corresponds with the highest risk areas. The following zones descend with intensity, indicating Zone 0 has no substantial earthquake risk. No earthquake requirements are given to Zone 0. Table 5.1 highlights the different earthquake risk zones with the expected Richter Magnitude, Modified Marcalli Index, and the expected ground and building accelerations (Telcordia Technologies, 2012).

5.2.2 VERTEQ-II Waveform

A prescribed waveform, VERTEQ-II, is used for the earthquake testing. VERTEQ-II is a synthesized waveform that represents the conditions of a typical floor motion within a building during an earthquake. The waveform captures variability by incorporating multiple typical earthquake ground motions for various building configurations and soil

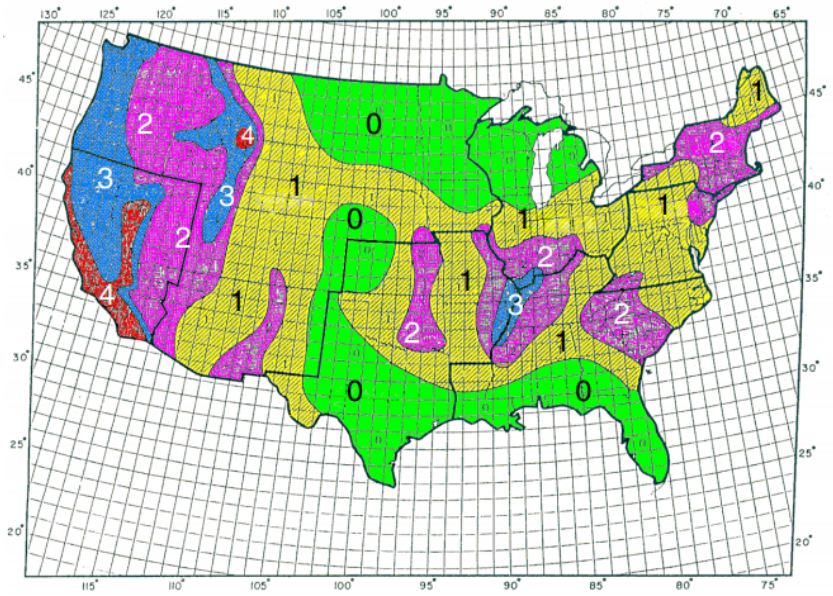

Figure 5.1: Earthquake Zone Map per GR-63-CORE (Telcordia Technologies, 2012).

site conditions. The acceleration, velocity, and displacement time histories of the Zone 4 VERTEQ-II record are shown in Fig. 5.2. The VERTEQ-II record has a peak ground acceleration (PGA) of 1.6 g, a peak ground velocity (PGV) of 102 cm/s, and a peak ground displacement (PGD) of 12.6 cm.

GR-63-CORE specifies a test plan for earthquake testing equipment using VERTEQ-II to run on a shaker table. The standard requires that "the shaker table's analyzed acceleration, also known as the Test Response Spectrum (TRS), must meet or exceed the Required Response Spectra (RRS) for applicable Earthquake Risk Zone

Table 5.1: Correlation of Earthquake Risks per GR-63-CORE (Telcordia Technologies, 2012).

Earthquake Risk Zone	Richter Magnitude	Modified Marcalli Index (MMI)	Low Frequency Ground Acceleration [g]	Low Frequency Upper Building Floor Acceleration [g]
0	< 4.3	V	< 0.05	< 0.2
1	4.3 – 5.7	V – VII	0.05 – 0.1	0.2 – 0.3
2	5.7 – 6.3	VII – VIII	0.1 – 0.2	0.3 – 0.4
3	6.3 – 7.0	VIII – IX	0.2 – 0.4	0.4 – 0.6
4	7.0 – 8.3	IX – XII	0.2 – 0.4	0.6 – 1.0

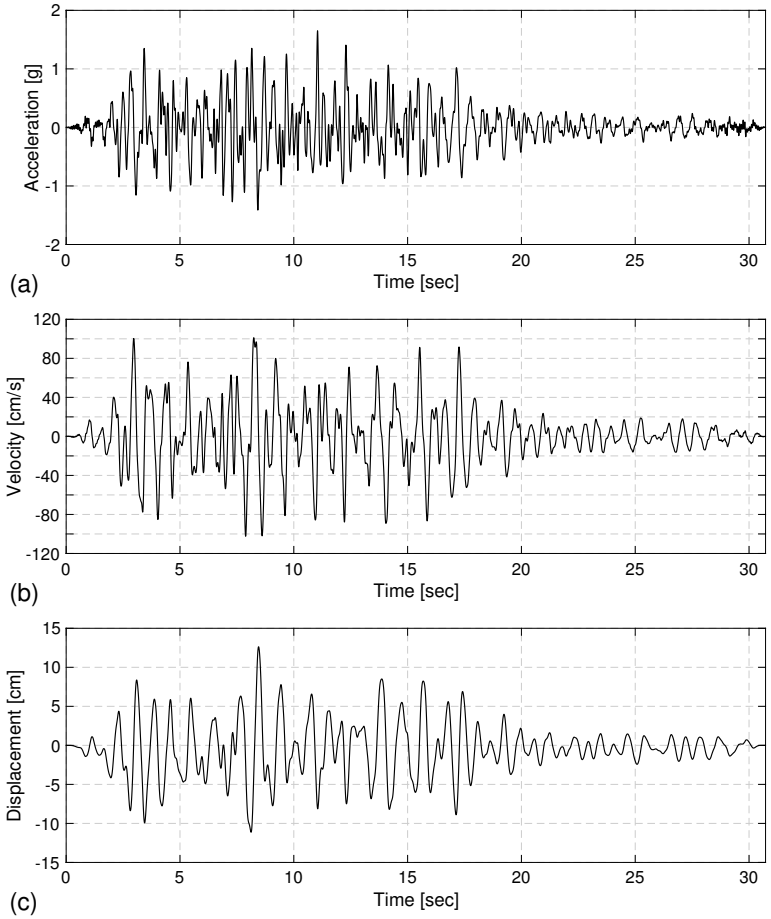

Figure 5.2: Earthquake Synthesized Waveform – VERTEQ-II (Telcordia Technologies, 2012).

in the range from 1.0 to 50 Hz." Also noted by the standard, "[t]he TRS is determined using a damping level of 2 %." The RRS is shown in Fig. 5.3 for earthquake risk Zone 4, which is prescribed by the coordinate points in Table 5.2 (Telcordia Technologies, 2012).

5.3 Isolation Performance

Vibration-sensitive equipment such as data cabinets are usually seismically rated according to their ability to prevent improper movement of components or overturning of the entire system during an earthquake. The seismic rating also includes the equipment's ability to sustain peak accelerations while still actively operating (Casey, 2017).

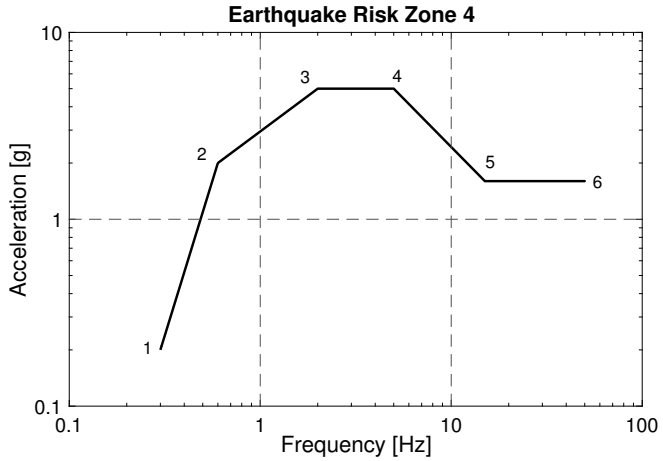

Figure 5.3: Required Response Spectrum per GR-63-CORE (Telcordia Technologies, 2012).

Dynamic Isolation Systems, Inc. (2017) observed that typical equipment can remain operational at accelerations up to 0.3 g. Accelerations felt by the equipment usually takes precedence for data cabinet protection design. RISs are prone to failure if excessive relative displacements cause impacts between the rolling profile's lip and the spherical steel ball (often not simulated due to complication within code). Relative displacements, therefore, also serve as a response quantity of interest for quality assurance of the overall performance of the RIS. RISs inherently possess a limited displacement capacity. As mentioned in Section 1.3.3, the typical single RIS displacement capacity is around 20 cm.

Table 5.2: Points given for the Required Response Spectrum (RRS) for Zone 4 per GR-63-CORE (Telcordia Technologies, 2012)

Coordinate Point	Frequency [Hz]	Values for Upper Floor Acceleration [g]
1	0.3	0.2
2	0.6	2.0
3	2.0	5.0
4	5.0	5.0
5	15.0	1.6
6	50.0	1.6

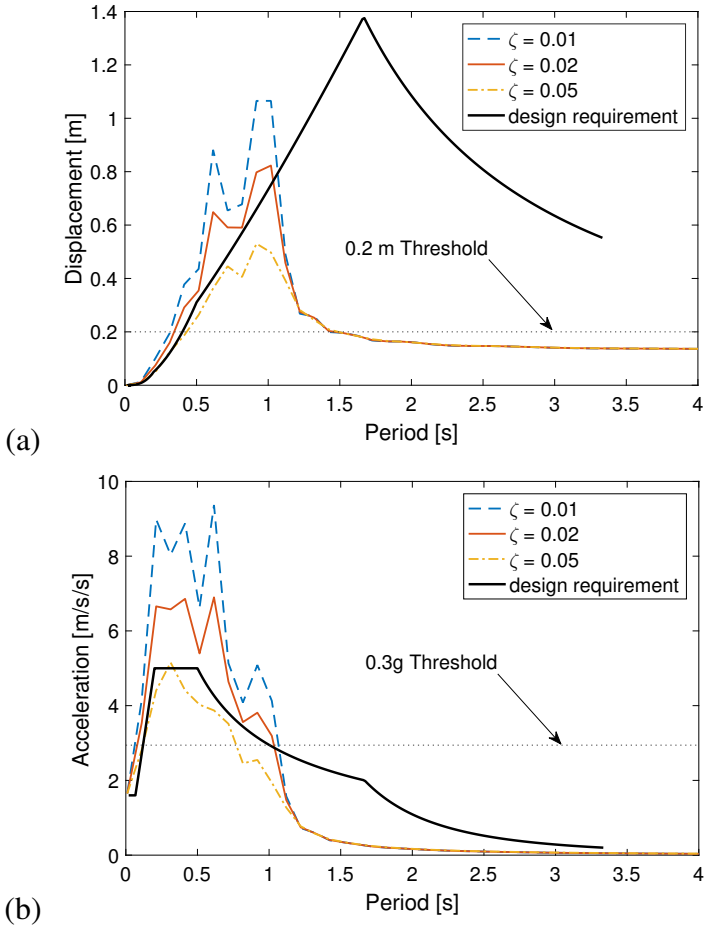

Figure 5.4: Displacement (a) and acceleration (b) response spectra for VERTEQ-II.

RISs lengthen the equipment period to a range of 1-2 seconds. In Fig. 5.4(a), the displacement response spectra is given for a single RIS subjected to the prescribed waveform, VERTEQ-II. For periods between 1 and 2 seconds, the RIS is nearly at or above its displacement capacity of 20 cm. Note that this response spectra corresponds to a 10% probability of exceedance in 50 years, also known as the design basis earthquake (DBE). Therefore, if the system should experience the maximum considered earthquake (MCE; 2% probability of exceedance in 50 years) the system would not have the capacity to accommodate the larger displacement demands. This proves that there exists a need to increase the displacement capacity of the RIS to accommodate extensive levels of demands.

It is also worth noting that the VERTEQ-II record was heavily filtered for frequencies below 1 Hz (periods longer than 1 second) due to the chances of shaker failure for large ground displacements beyond its capacity. This in turn greatly decreased the displacement response [Fig. 5.4(a)] at low frequencies where RISs operate; the design requirement is substantially higher for both the displacement [Fig. 5.4(a)] and accelerations [Fig. 5.4(b)]. The filtered data was used for the numerical simulation of the double RIS.

5.3.1 Performance Criteria

The evaluation criteria in this study examines the peak total acceleration experienced by the equipment given by

$$a_o^{\mathrm{t}} = \max_t \left| a^{\mathrm{t}}(t) \right| \tag{5.1}$$

where $a^{\mathrm{t}}(t)$ is the equipment acceleration. The allowable limit for a_o^{t} is typically taken to be 0.3 g; if felt accelerations exceed the allowable limit, the isolated equipment may experience damage, constituting a failure of the RIS. While Casey (2017) reported that cabinets holding sensitive electronics normally remain operational between the range of 0.25 g shaking and 0.33 g impact load, the performance of the double RIS will be assessed in terms of peak total accelerations sustained by the isolated equipment.

Additionally, for the evaluation criteria, this study examines the maximum peaking bearing displacement experienced by each isolation layer given by

$$u_{io} = \max_t |u_i(t)| \quad (i = 1, 2) \tag{5.2}$$

where $u_i(t)$ relative displacement across the ith bearing. The allowable limit on u_{io} is taken to be 20 cm; beyond the allowable limit indicates an impact that degrades the system's performance.

5.4 Parametric Study

In order to simulate the behavior of multiple configurations of the double RIS, a parametric study of various rolling radii for both the top and bottom rolling profiles is presented. The response of each system's peak relative displacement for each isolation layer and its peak acceleration is given in the contour plots in Figs. 5.5, 5.6, and 5.7, respectively. It is important to note that the brightness of the color in the contour indicates the level of the response: yellow, the brightest color in the plot, indicates the highest response, while dark blue, the darkest color, indicates the lowest response. For the purposes of this study, the lowest possible response from all three criteria is of interest. Each separate plot signifies a different mass ratio value, $\mu = m_1/m_2$, for a constant damping ratio (ζ_i) of 2% for both isolation layers.

For displacements in the first isolator layer (Fig. 5.5), significant peak response values occur when the radius of the first layer (R_1) is substantially larger than the radius of the second layer (R_2). This trend is explained by the fact that the first layer is softer (more flexible) than the second layer. For displacements in the second isolator layer (Fig. 5.6), the opposite is true; a ridge of the peak response values form at larger R_2 ($>$ 6 cm) than R_1 ($<$ 5 cm). This trend is explained by the second layer being softer, accommodating larger displacements than the first layer. The behavior of the softer layer can be thought to act similar to a structure with a "soft story." When the structure encounters a lateral load, the stiffer story would resist more of the load but deflect little, while the softer story would resist less of the load but deflect more under the same load. Similarly, a softer layer in the double RIS would displace more for a given excitation due to the lack of resistance possessed by the shallow rolling profile curvature.

Another trend apparent in both Figs. 5.5 and 5.6 is where a new ridge begins to form for large R_2 ($>$ 50 cm) relative to the first radius (10 cm $< R_1 <$ 100 cm) as an effect from increasing mass ratio in each subsequent figure (a–f). This may be explained by

the influence increasing the mass ratio has on which modes contribute to the response of the system. With the increase of the mass ratio, the higher (second) coupled frequency decreases, moving into a higher energy region of the response spectrum, and the modal participation factor for second mode increases (Chopra, 2012). These factors contribute to the second mode of response having more of an influence on the displacements in each layer.

As for accelerations (Fig. 5.7), it appears that significant responses occur at small radii (< 10 cm) for both isolation layers, with the largest responses occurring for radii less than 4 cm. Figs. 5.7(a)–5.7(f) are symmetrical about the highlighted 1:1 line. Therefore, the acceleration performance of a double RIS is independent of the arrangement of the order of the isolation layers. For instance, the peak acceleration response of a double RIS with different top and bottom layer radii, e.g., $(R_1, R_2) = (25\text{ cm}, 50\text{ cm})$, would perform the same as another double RIS with the flipped configuration of the original double RIS, e.g, $(R_1, R_2) = (50\text{ cm}, 25\text{ cm})$. This symmetry was not observed for displacements (Figs. 5.5 and 5.6). To explore this behavior further, the response along the 1:1 line (*Case I*) is considered in detail in the following section.

5.4.1 Case I: Identical Radii

For identical radii ($R_1 = R_2$) given by the 1:1 line from the contour plots (Figs. 5.5, 5.6, and 5.7), Fig. 5.8 illustrates the peak responses for a double RIS varying mass ratios compared to a single RIS. For Fig. 5.8(a), the peak displacements of the first isolator for varying identical radii of the double RIS, u_{1o}, appears to have a splitting effect due to the pairing of two isolators. Similar behavior was observed in Chapter 3 when the SDOF structure was placed upon the single RIS. The splitting effect for the double RIS reduces the maximum peak displacement response of the first isolator compared to the single RIS. However, increased responses for radii above 11 cm occur for increasing mass ratios ($\mu > 5\%$) with increasing radii size. The similar splitting effect is found in

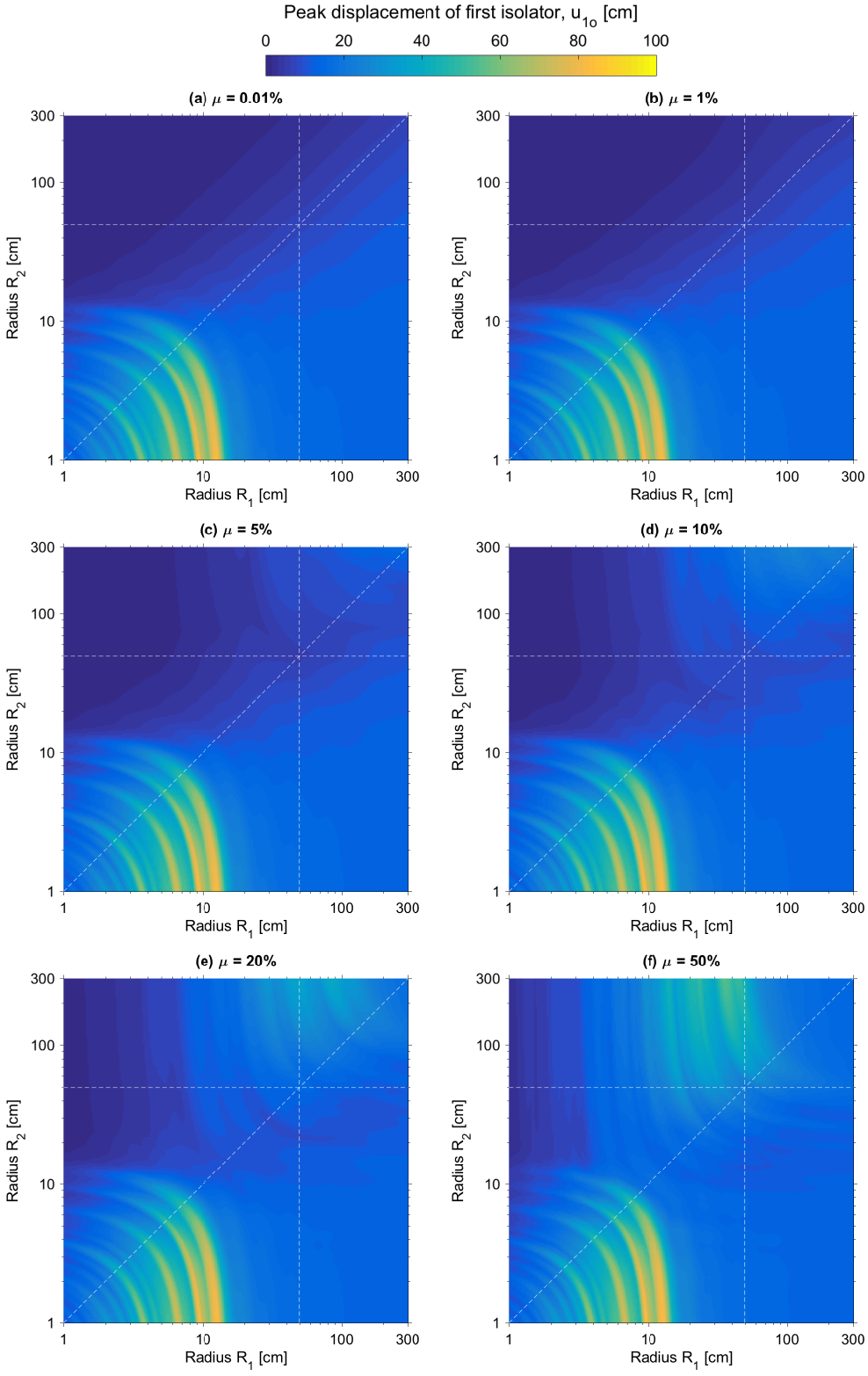

Figure 5.5: Peak displacement across first isolator, u_{1o}, of double RIS with μ = (a) 0.01%, (b) 1%, (c) 5%, (d) 10%, (e) 20%, and (f) 50%.

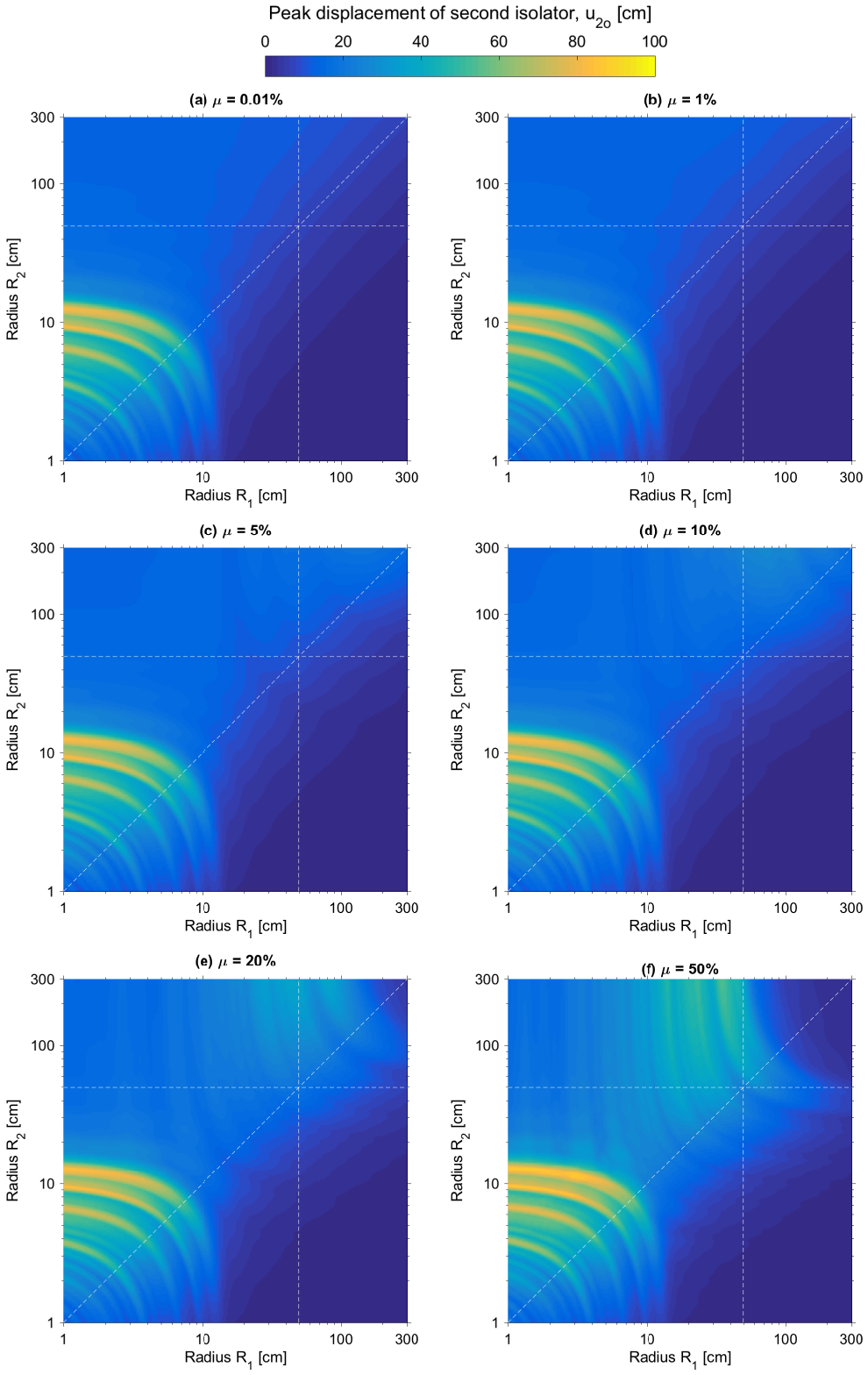

Figure 5.6: Peak displacement across second isolator, u_{2o}, of double RIS with μ = (a) 0.01%, (b) 1%, (c) 5%, (d) 10%, (e) 20%, and (f) 50%.

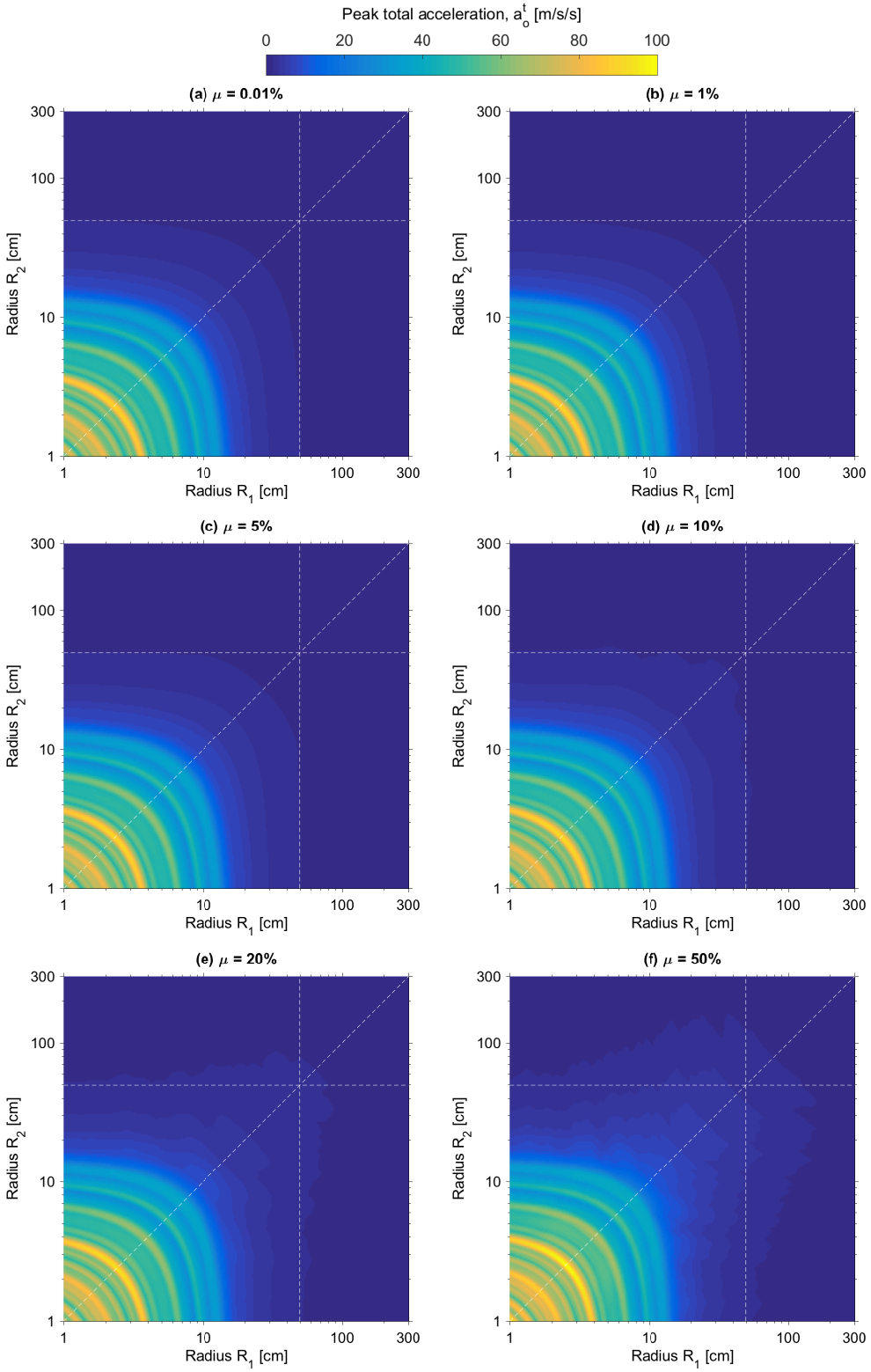

Figure 5.7: Peak total acceleration of isolated equipment, a_o^t, of double RIS with μ = (a) 0.01%, (b) 1%, (c) 5%, (d) 10%, (e) 20%, and (f) 50%.

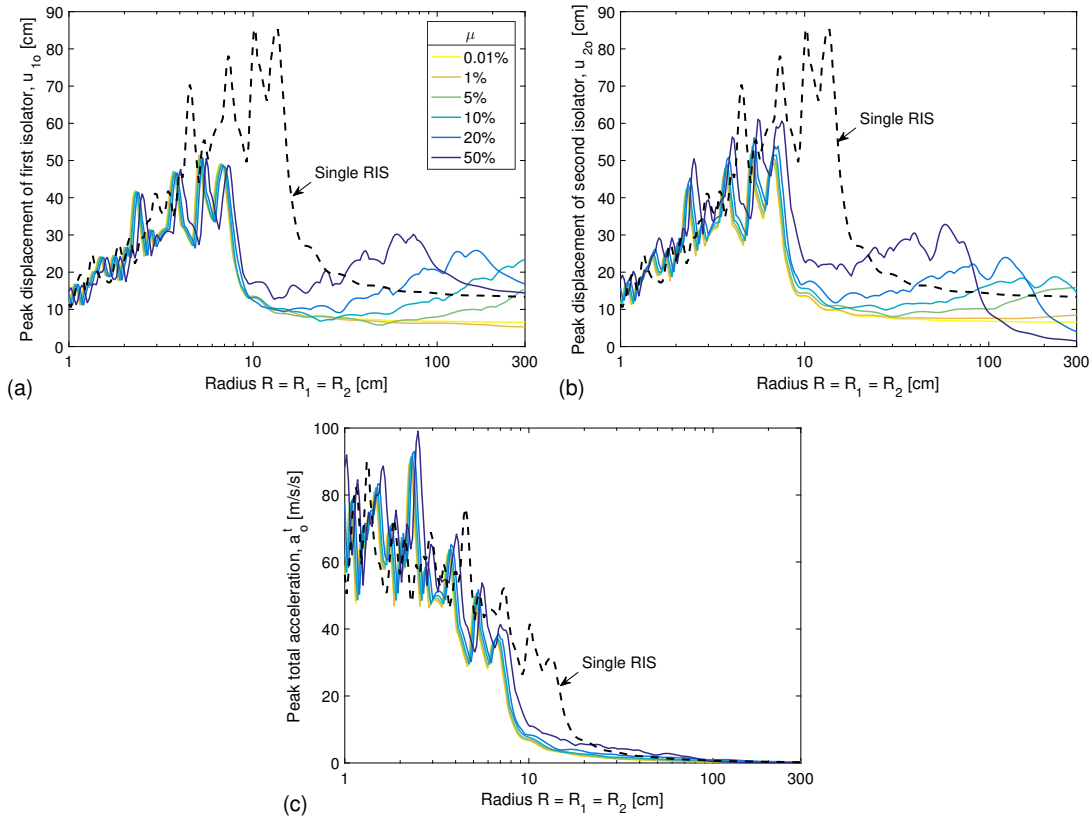

Figure 5.8: Peak responses—(a) displacement of first isolator, u_{1o}; (b) displacement of second isolator, u_{2o}; and (c) total acceleration of equipment, a_o^t—of double RIS with varying, but equal, first and second rolling radii ($R_1 = R_2$) and varying mass ratio μ.

Fig. 5.8(b) for the peak displacements of the second isolator, u_{2o}.

As for the total acceleration peak responses in Fig. 5.8(c), all the cases for the double RIS trend toward zero as the rolling radii become large ($R > 10$ cm). Eventually, the same is true for the single RIS. It is important to note that, as accelerations begin to decrease, displacements begin to increase in the double RIS. This double RIS behaves in accordance with previous studies over the competing objectives of a dual isolation acceleration and displacement response spectra (Becker and Ezazi, 2016). The displacement response spectra for the single RIS remains at capacity (18–20 cm) for rolling radii greater than 11 cm, while for the double RIS ($\mu < 5\%$) each subsystem performs well below the same capacity of single RIS.

Figs. 5.9, 5.10, and 5.11 show the time histories when each rolling radius equals 48.7 cm for varying mass ratios. The results show the double RIS's total acceleration, sub-system displacements, and the total displacement compared to the single RIS's response criteria. Fig. 5.9 compares the response of the baseline single RIS to the response of a double RIS with a low mass ratio (μ = 1%). The double RIS peak acceleration and the sub-system peak displacements are nearly half of the single RIS peak responses, while the total displacements of both the single and double RIS are nearly identical. In terms of design, the double RIS (μ = 1%) would reduce accelerations by almost half for half the bearing displacement found in a single RIS, allowing for smaller components to be used saving money.

Fig. 5.10 compares the response of the baseline single RIS to the response of a double RIS with a moderate mass ratio (μ = 10%). Similarly to Fig. 5.9, some reductions are found for the accelerations and subsystem displacements for the same amount of displacements in the single RIS. In the sub-system displacements plots [Figs. 5.9(c,d)], it is apparent that the second mode of the double RIS is becoming more prevalent in the system's response. This trend continues as shown in Fig. 5.11, where the mass ratio increases to 50%. No longer are the sub-system displacements lower than that of the baseline single RIS. The double RIS total displacements remain similar to the single RIS displacements, but the double RIS experiences substantially larger accelerations, in turn degrading the performance of the the double RIS. Hence, a low mass ratio is desired. The next section will examine the performance of the double RIS when one of the rolling radii is held constant as the other rolling radius varies (*Case II*).

5.4.2 Case II: Varying Radii

The white horizontal and vertical lines visible on the contour plots (Figs. 5.5, 5.6, and 5.7) are scenarios where one of the rolling radii is held constant as the other rolling radius varies. The constant rolling radius for both scenarios is taken to be 49.7 cm,

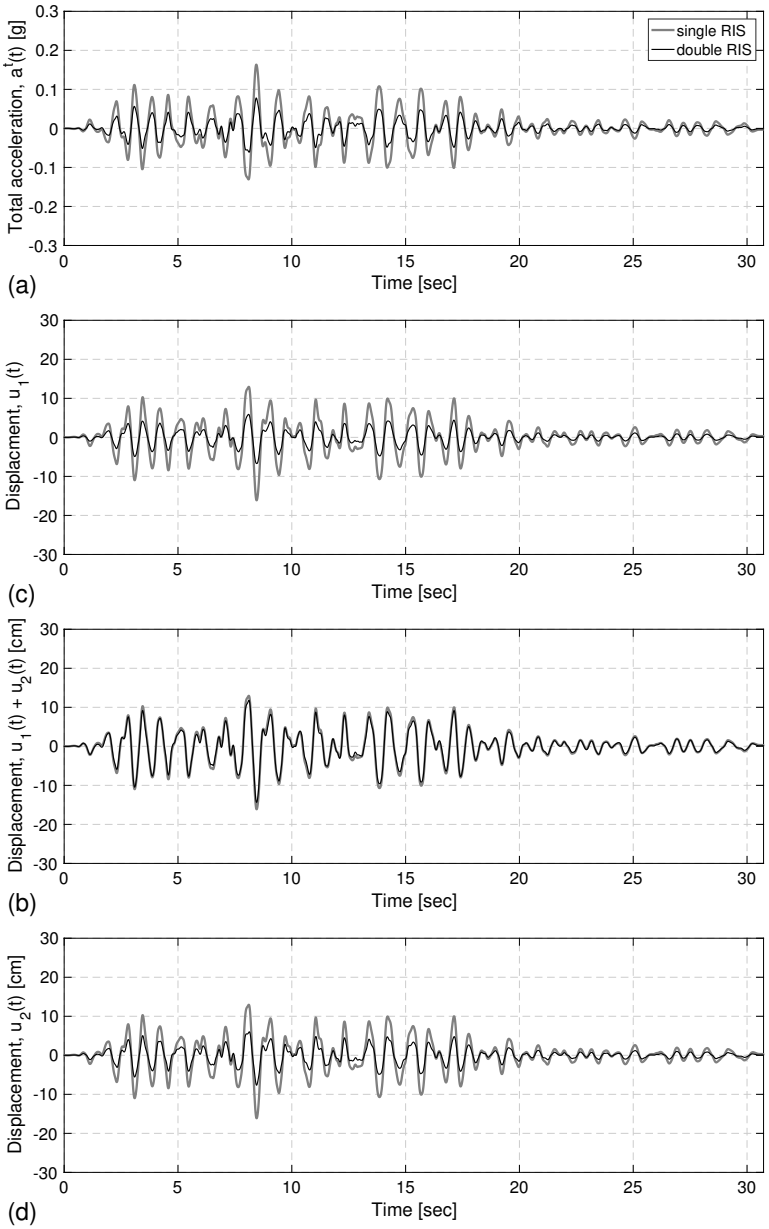

Figure 5.9: Response of a single RIS and double RIS with mass ratio $\mu = 1\%$; $R = R_1 = R_2 = 48.7$ cm.

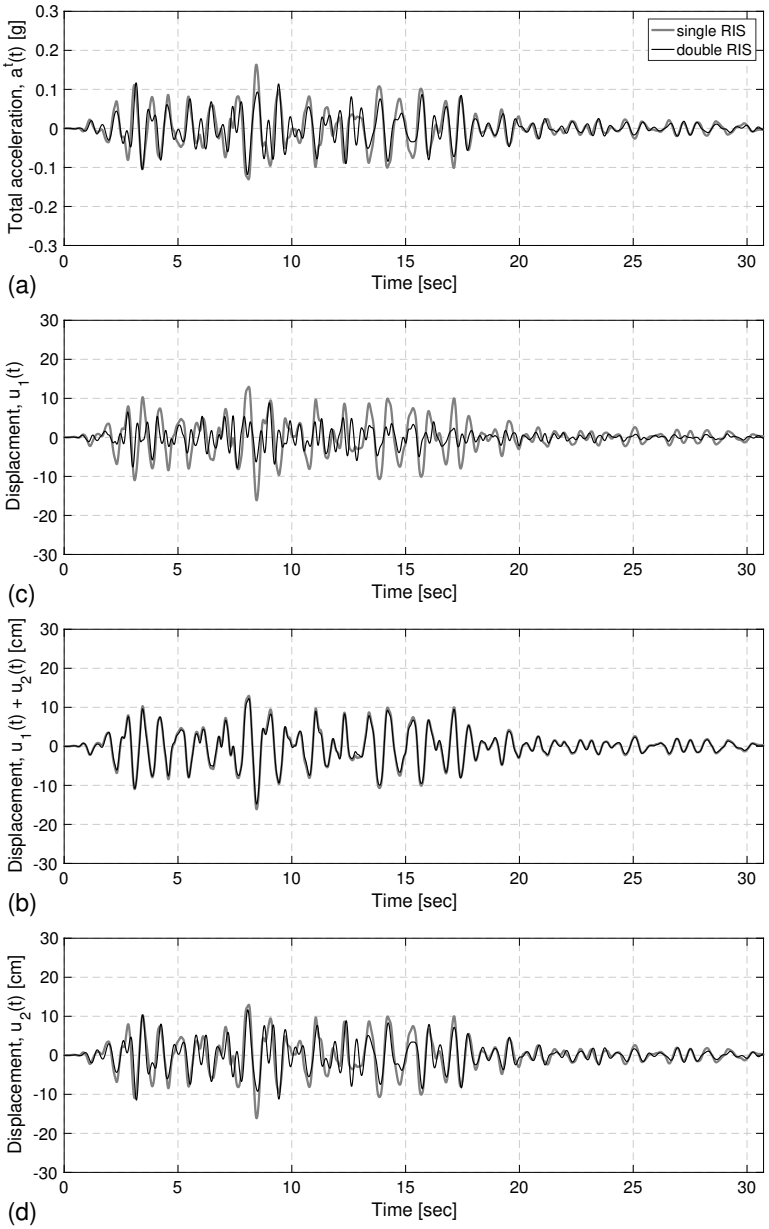

Figure 5.10: Response of a single RIS and double RIS with mass ratio $\mu = 10\%$; $R = R_1 = R_2 = 48.7$ cm.

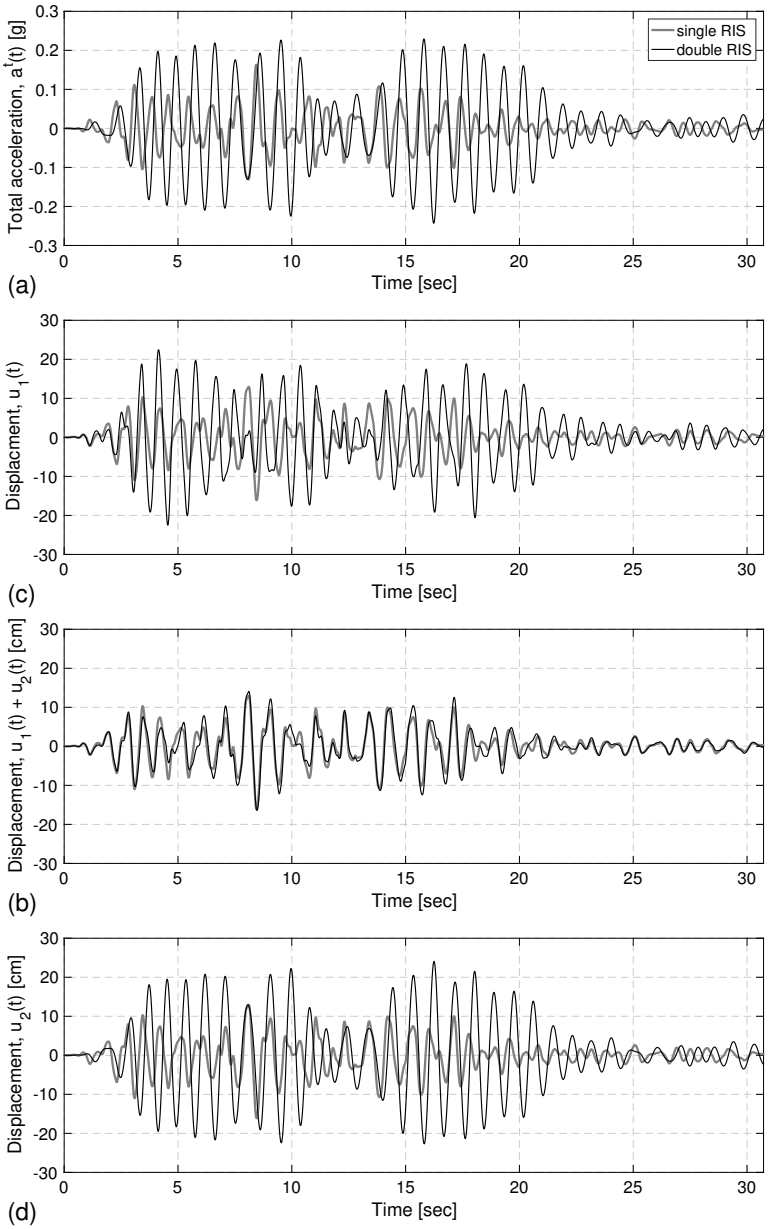

Figure 5.11: Response of a single RIS and double RIS with mass ratio $\mu = 50\%$; $R = R_1 = R_2 = 48.7$ cm.

which corresponds to an isolation layer having a natural circular frequency of 3.14 rad/s (period of 2 seconds) using the linearized expression found in Section 2.4. Using a 2-second period for the fixed rolling radii allows for a comparative study to a single RIS where the rolling radius is also 49.7 cm. This provides a baseline case to benchmark the behavior of the double RIS.

SCENARIO A

In Figs. 5.5, 5.6, and 5.7, the vertical line on the contour plots signifies that this scenario corresponds to R_1 equaling 49.7 cm, while R_2 varies. Fig. 5.12 displays all the peak response criteria for the double RIS with varying mass ratio. In Fig. 5.12(a), the peak displacement responses of the first isolator, u_{1o}, for small R_2 (< 2 cm) approach the single RIS displacement. This asymptotic behavior signifies that the double RIS effectively becomes a single RIS, where the first isolation layer is handling the displacement demand of the system and the second isolation layer is effectively rigid.

In Fig. 5.12(b), the peak displacement responses of the second isolator, u_{2o}, asymptotically approach zero, therefore verifying that the first isolation layer handles the entire double RIS displacement demand for small R_2 values. As R_2 increases the displacements in each isolation layer [Figs. 5.12(a,b)] increase for $\mu \geqslant 10\%$. For $\mu < 10\%$, the curves do not peak above the single RIS line. It appears that these systems behave as a single RIS, where the first isolation layer behaves rigidly and the second isolation layer accommodates all the displacement needs. Fig. 5.12(b) shows some curves ($\mu \geqslant 10\%$) increasing above the single RIS line, while other mass ratio values ($\mu < 10\%$) approach the single RIS line. Correlating this behavior with Fig. 5.12(a), double RISs with $\mu < 5\%$ behave similarly to the single RIS with the second isolation layer accommodating the displacement demand.

Fig. 5.12(c) displays peak total acceleration response, a_o^{t}, for a varying rolling radius R_2 and varying mass ratio μ. Mass ratios less than or equal to 5% have responses

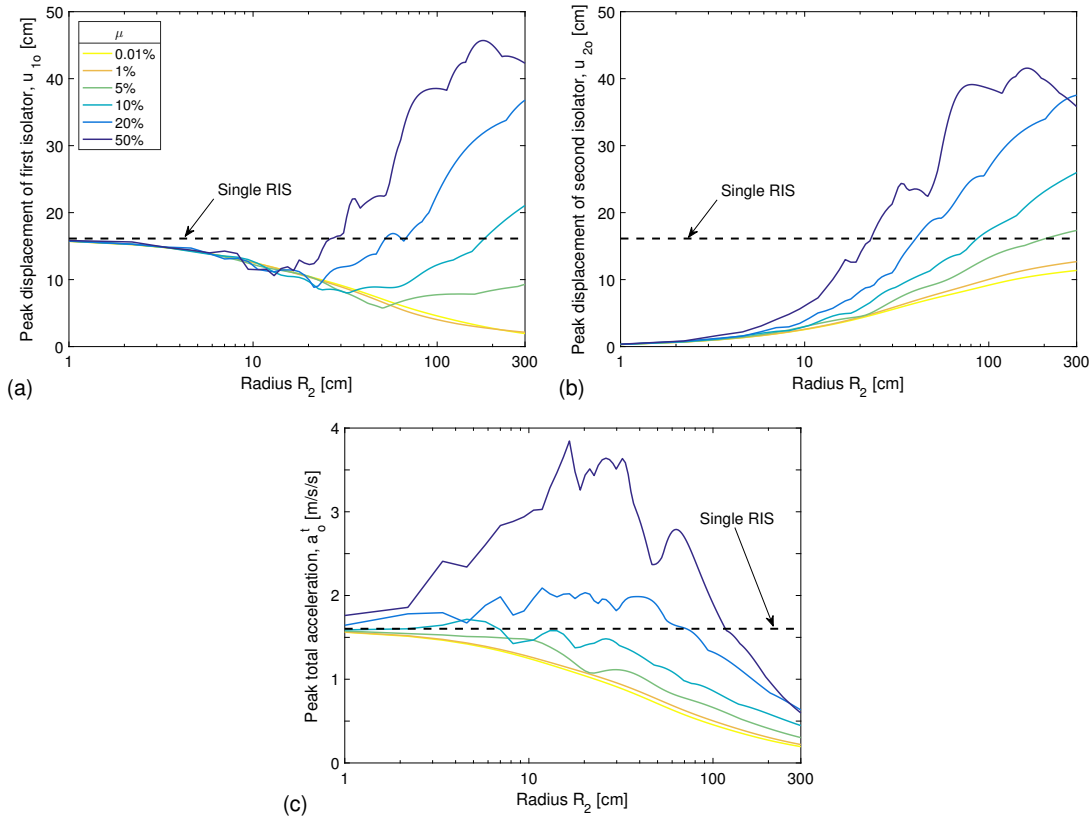

Figure 5.12: Peak responses—(a) displacement of first isolator, u_{1o}; (b) displacement of second isolator, u_{2o}; and (c) total acceleration of equipment, a_o^t—of double RIS with varying second rolling radius R_2 and varying mass ratio μ. First rolling radius $R_1 = 49.7$ cm.

below the single RIS tolerance of 0.3 g (2.943 m/s^2). Although all of the mass ratios drop below the single RIS line for large R_2 relative to R_1, substantial displacements are endured for large mass ratios.

As previously mentioned, the modal participation of the second mode for high mass ratios play a role in displacement responses. In this scenario, it is seen that the higher the mass ratio, the higher the displacement experienced for large radii even when one radius is held constant.

SCENARIO B

In Figs. 5.5, 5.6, and 5.7, the horizontal line on the contour plots display this final scenario corresponding to R_1 varying and R_2 equaling 49.7 cm. Fig. 5.13 displays all

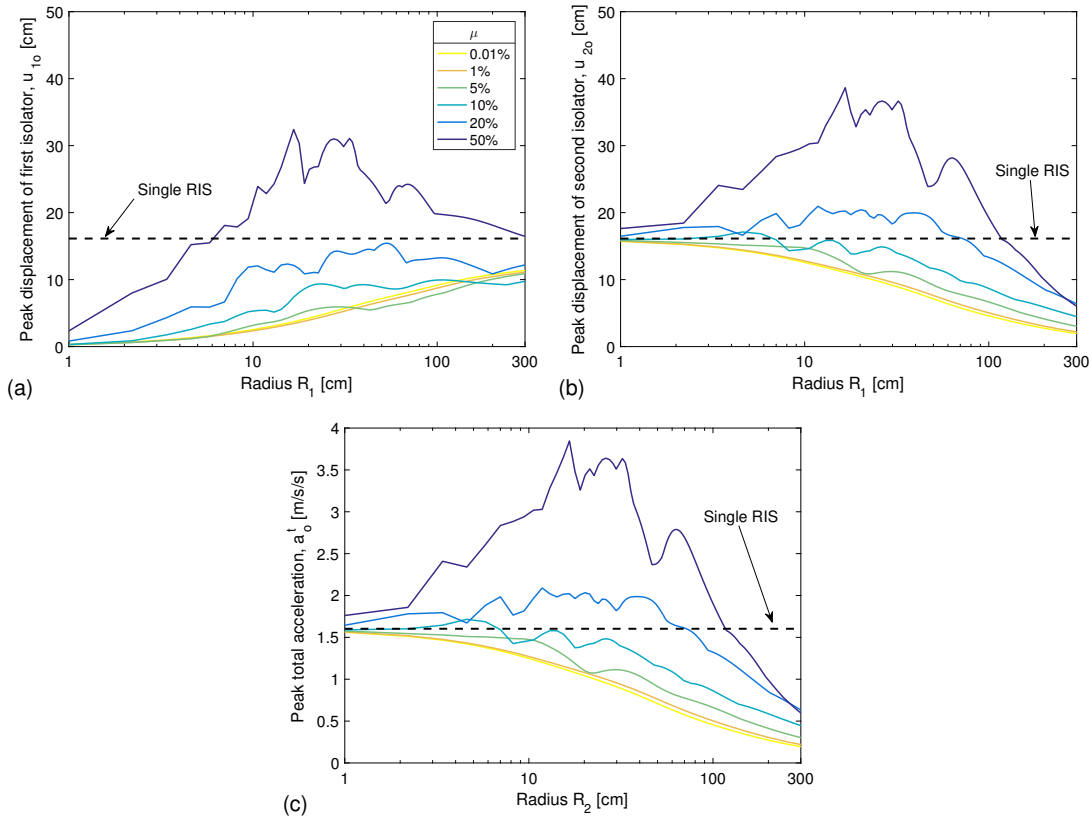

Figure 5.13: Peak responses—(a) displacement of first isolator, u_{1o}; (b) displacement of second isolator, u_{2o}; and (c) total acceleration of equipment, a_o^t—of double RIS with varying first rolling radius R_1 and varying mass ratio μ. Second rolling radius $R_2 = 49.7$ cm.

the peak response criteria for the double RIS with varying mass ratio. Because of the symmetry of the accelerations about 1:1 in the contour plots, Fig. 5.13(c) is identical to Fig. 5.12(c). Although the accelerations are indistinguishable, the displacement of both isolation layers for this scenario is not identical to scenario A. The behaviors at very small and very large radii of each figure are sightly different, but the general concept of these double RISs behaving like a single RIS still applies. Nevertheless, the curves in these figures moves asymptotically toward either zero or the single RIS line. In Fig. 5.13(a), the peak displacement of the first isolator, u_{1o}, appears to begin from zero when R_1 is small relative to R_2. As previously noted, when a rolling radius is relatively small it behaves essentially rigid and all deformation occurs in the other iso-

lator layer. This is highlighted by the left side of Fig. 5.13(b). The other side of each figure [Figs. 5.13(a,b)] behaves in the opposite manner. Regardless of the double RIS mass ratios, Fig. 5.13(a) asymptotically approaches the single RIS line and Fig. 5.13(b) asymptotically approaches to zero. It is worth noting in Fig. 5.13(a) that the curves for $\mu < 50\%$ fall below the displacement of a single RIS yielding optimal performance. Unfortunately, Fig. 5.13(b) does not display the same level of performance for the same mass ratios. Similar to scenario A, cases with $\mu < 10\%$ do not climb above the single RIS threshold, proving to have the optimal performance under the VERTEQ-II record.

Displacement Limits

As a reminder, the results presented in this section were numerically simulated using the linearized equations of motion for the double RIS. This linearization relies on the assumption that $u_i \ll 2R_i$. It is worth noting that this assumption is not satisfied for all the cases considered [e.g., for 1 cm $\leqslant R \leqslant$ 6 cm in Figs. 5.8(a) and 5.8(b)]. Further, it is not feasible to have a bearing displace greater than 2 times its radius. Impacts would occur before this displacement would be reached, thus making this assumption not mathematically sound or practical for certain locations on Figs. 5.5, 5.6, and 5.7.

5.5 Summary

In this chapter, a deterministic analysis using the VERTEQ-II waveform was performed. The corresponding response criteria were outlined for the analysis. Peak displacements for each isolation layer of the double RIS and peak total accelerations were presented for relevant system geometries, namely radii R_1 and R_2. Regions of better performance in terms of each criterion were highlighted. Two cases were considered for further analysis: equal radii, and one varying radius with the other radius held constant. Observations were made based upon these different cases considered, which were compared to a single RIS. It was found that the double RIS with low mass ratio performed opti-

mally compared to the other cases. This is because the double RIS behaves similarly to a single RIS, but has an increased displacement capacity to accommodate larger disturbances without impacts. Therefore, it is advantageous to design a double RIS with a low mass ratio ($\mu < 10\%$) with a softer first rolling radius than the second rolling radius ($R_1 > R_2$).

Chapter 6

Summary, Conclusions, and Future Work

6.1 Summary and Conclusions

Earthquakes in past years have created significant damage to infrastructure, impaired businesses operations, and caused loss of life. A growing concern is seismic damage to nonstructural components. In recent years, nonstructural components have received more attention from design codes. Design codes such as IBC or GR-63 have stringent requirements for equipment given as a seismic rating. The seismic rating requires that the equipment remain operational depending on the level of its rating. Yet, there remains a need for innovative solutions for equipment protection design. A promising solution to protect equipment is a rolling-type isolation system (RIS) because of its simple installation and performance compared to other isolation systems.

A physics-based mathematical model for a single RIS was derived via Lagrange's equations. The mathematical modeling of the RIS was used to simulate the RIS under various seismic motions. The mathematical model allows for the RIS geometries and system parameters to be altered to evaluate the system's performance over a range of configurations and disturbances. Four configurations were selected for fabrication and were tested against three different earthquake ground motions. The 3D-printed RIS model was extended to a sliding mechanism to test the performance of a rolling pendulum bearing against a friction pendulum bearing. Each of the bearings was fabricated

twice for two different radii. The experimental results showed the rolling pendulum bearing performed better than the friction pendulum bearing for all earthquakes except for the earthquake with low-frequency content. It was found that Mendocino had higher acceleration for the same range as the rolling pendulum bearing's natural frequency. It is worth noting that if the amplification is large enough, impacts could occur, which would be detrimental to the single RIS performance. Therefore, a double RIS was proposed to accommodate large displacements.

A fully-nonlinear mathematical model of the double RIS was developed to simulate the system performance for both stochastic and deterministic disturbances. For the stochastic analysis, a closed-form expression for the transfer function was derived from the linearized equations of motion. Different excitation power spectral densities (PSDs) were considered: constant (broadband) white noise and an earthquake-like disturbance based on the Kanai-Tajimi filter. Relevant parameters of the double RIS were varied and the response metrics (variances) were recorded. A single RIS acted as the baseline case to benchmark the double RIS performance. Optimal placement of the second isolator to the baseline RIS was considered. The placement of the second isolation layer was found inconclusive to the overall performance of the double RIS, only modifying the rolling radii induced better performance than a single RIS. For the broadband disturbance, there was no region in the system parameter space where all three performance metrics showed improvement. For the earthquake-like PSD, there existed a region in the parameter space in which all three response metrics showed improvement. This overlapping area, therefore, constitutes the proposed design parameter map. The Kanai Tajimi PSD is more representative of an earthquake record than the constant PSD.

Finally, a deterministic analysis was performed to further assess the double RIS's performance. A single synthesized waveform, VERTEQ-II, was applied to the numerical model of the double RIS. Relevant parameters (tuning frequency, and mass ratio)

of the double RIS were varied, and the corresponding responses were recorded. The addition of a low frequency (softer) first isolation layer relative to the other layer has optimal response quantities, and this aligns with the stochastic analysis where accelerations were reduced by the addition of a softer isolation layer. It is worth noting that low mass ratios further reduce accelerations and displacements. It is recommended to refer to the design plots for the Kanai-Tajimi case for a more comprehensive design approach. These results aim to provide a framework usable in the preliminary design stage of a double RIS to mitigate seismic responses.

6.2 Future Work

Motivated by the findings of this study, existing knowledge gaps in the seismic protection of non-structural building contents have been identified. Due to time constraints, however, these research topics are outside the scope of this thesis. Future studies should address these research needs listed below, some of which require a 3D printer to fabricate the double RIS and a shake table to test the system.

- The mathematical model of the double RIS should be experimentally validated. The double RIS could be readily fabricated with additive manufacturing, as done in Chapter 3, then tested with a shake table using the VERTEQ-II waveform. The tuning frequencies of the stochastic analysis could be tested as well for performance verification for a wide range of earthquakes.

- This study considered only the VERTEQ-II waveform, but the double RIS should be tested subject to numerous other ground motions. The performance of the double RIS subjected to VERTEQ-II has skewed results because of the filtering of the low-frequency content for shake table testing. Therefore, the performance of the double RIS gives a false representation of the performance of the double RIS in the area of low-frequency content based on VERTEQ-II alone. Additional synthe-

sized earthquakes, or natural earthquakes, could easily be numerically simulated with the mathematical model and/or and experimentally tested with the physical model to get a holistic view of the double RIS's performance.

- Other innovative RIS designs should be proposed and evaluated. For example, the RIS could be designed such that its behavior is displacement dependent based on a level of disturbance similar to a triple friction pendulum. The study may focus on the relationship between the double RIS's increased capacity and its ability to reduce displacement with the addition of damping. A backbone curve could be constructed to illustrate the different stiffnesses and damping with each level of disturbance.

- The double RIS considered in this study was linearized using the assumption of large rolling radius compared to the amount of displacement across the rolling surface. Possible future studies could look at the nonlinear behavior of the double RIS system when the vertical components are retained in the equations of motion, or the rolling profiles of the double RIS are different from the constant radius rolling profile (e.g., conical or polynomial).

Bibliography

J. L. Almazán, J. C. De La Llera, J. A. Inaudi, Modelling aspects of structures isolated with the frictional pendulum system, Earthquake Engineering & Structural Dynamics 27 (8) (1998) 845–867, doi:10.1002/(SICI)1096-9845(199808)27:8⟨845::AID-EQE760⟩3.0.CO;2-T.

T. Asami, O. Nishihara, A. M. Baz, Analytical Solutions to H∞ and H2 Optimization of Dynamic Vibration Absorbers Attached to Damped Linear Systems, Journal of Vibration and Acoustics 124 (2) (2002) 284–295, doi:10.1115/1.1456458.

T. Asami, T. Wakasono, K. Kameoka, M. Hasegawa, H. Sekiguchi, Optimum design of dynamic absorbers for a system subjected to random excitation, JSME International Journal. Ser. 3, Vibration, Control Engineering, Engineering for Industry 34 (2) (1991) 218–226, doi:10.1299/jsmec1988.34.218.

T. C. Becker, A. Ezazi, Enhanced performance through a dual isolation seismic protection system, The Structural Design of Tall and Special Buildings 25 (1) (2016) 72–89, doi:10.1002/tal.1229.

G. Bondonet, A. Filiatrault, Frictional Response of PTFE Sliding Bearings at High Frequencies, Journal of Bridge Engineering 2 (4) (1997) 139–148, doi:10.1061/(ASCE)1084-0702(1997)2:4(139).

J. E. Brock, A Note on the Damped Vibration Absorber, ASME Journal of Applied Mechanics 68 (1946) A–284.

I. G. Buckle, R. L. Mayes, Seismic Isolation: History, Application, and Performance–A World View, Earthquake Spectra 6 (2) (1990) 161–201, doi:10.1193/1.1585564.

S. J. Calhoun, J. Harvey, P S, Enhancing the teaching of seismic isolation using additive manufacturing, Engineering Structures 167 (2018) 494–503, doi:10.1016/j.engstruct.2018.03.084.

C. D. Casey, Rolling-Type Isolation: An Experimental Characterization and Numerical Parametric Study, M.S. Thesis, University of Oklahoma, 2017.

C. Chadwell, K. Brennan, M. Porter, Seismic Hazard Mitigation of Wine Barrel Stacks, in: Structures 2009: Don't Mess with Structural Engineers, ASCE, 1011–1019, 2009.

A. K. Chopra, Dynamics of Structures: Theory and Applications to Earthquake Engineering, Prentice Hall, Englewood Cliffs, New Jersey, 4th edn., 2012.

L. L. Chung, C. Y. Yang, H. M. Chen, L. Y. Lu, Dynamic behavior of nonlinear rolling isolation system, Structural Control and Health Monitoring 16 (2009) 32–54, doi:10.1002/stc.305.

M. C. Constantinou, J. Caccese, H. G. Harris, Frictional characteristics of Teflon–steel interfaces under dynamic conditions, Earthquake Engineering & Structural Dynamics 15 (6) (1987) 751–759, doi:10.1002/eqe.4290150607.

S. H. Crandall, W. D. Mark, Random Vibration in Mechanical Systems, Academic Press, New York, 2nd edn., 1963.

N. D. Dao, K. L. Ryan, E. Sato, T. Sasaki, Predicting the displacement of triple pendulum bearings in a full scale shaking experiment using a three dimensional element, Earthquake Engineering & Structural Dynamics 42 (11) (2013) 1677–1695, doi:10.1002/eqe.2293.

J. P. Den Hartog, Mechanical Vibration, Dover, 1985.

E. Devlin, C. Emerson, L. Wrobel, Business Resumption Planning, CRC Press, 1997.

S. Dyke, J. Caicedo, M. Soto-Fournier, University Consortium of Instructional Shake Tables: Enhancing Education in Earthquake Engineering, in: Proceedings of the International Meeting on Civil Engineering Education, Real Cuidad, Spain, 2003.

Dynamic Isolation Systems, Inc., Non-Structural Isolation, Brochure, URL http://www.dis-inc.com/pdf_files/DIS%20Non-Structural%20Isolation.pdf, 2017.

EEFIT, The Northridge, California Earthquake of 17 January 1994, Tech. Rep., Earthquake Engineering Field Investigation Team, 1997.

EQE, The January 17, 1994 Northridge, California earthquake: an EQE summary report, EQE International, [San Francisco], 1994.

FEMA, Primer for Design Professionals: Communicating with Owners and Managers of New Buildings on Earthquake Risk, Tech. Rep. FEMA 389, Federal Emergency Management Agency, Washington, DC, 2004.

FEMA, HAZUS MH Estimated Annualized Earthquake Losses for the United States, Tech. Rep. 366, Federal Emergency Management Agency, Washington, D.C., 2008.

D. M. Fenz, M. C. Constantinou, Spherical sliding isolation bearings with adaptive behavior: Experimental verification, Earthquake Engineering and Structural Dynamics 37 (2008b) 185–205, doi:10.1002/eqe.750.

D. M. Fenz, M. C. Constantinou, Spherical sliding isolation bearings with adaptive behavior: Theory, Earthquake Engineering and Structural Dynamics 37 (2008a) 163–183, doi:10.1002/eqe.751.

D. Foti, J. M. Kelly, Experimental analysis of a model isolated at the base with rubber-layer roller bearing (RLRB), European Earthquake Engineering 10 (1996) 3–13.

H. Frahm, Device for damping vibrations of bodies, U.S. patent 989,958, 1909.

T. S. Fu, E. A. Johnson, Distributed Mass Damper System for Integrating Structural and Environmental Controls in Buildings, Journal of Engineering Mechanics 137 (3) (2011) 205–213, doi:10.1061/(ASCE)EM.1943-7889.0000211.

D. T. Greenwood, Advanced dynamics, Cambridge University Press, New York, NY, 2003.

V. E. Hahnkamm, Die Dämpfung von Fundamentschwingungen bei veränderlicher Erregerfrequenz, Ingenieur Archiv 4 (1932) 192–201, doi:10.1007/BF02079857, (in German).

P. S. Harvey, Jr., Rolling Isolation Systems: Modeling, Analysis, and Assessment, Ph.D. Thesis, Duke University, 2013.

P. S. Harvey, Jr., H. P. Gavin, The nonholonomic and chaotic nature of a rolling isolation system, Journal of Sound and Vibration 332 (2013) 3535–3551, doi:10.1016/j.jsv.2013.01.036.

P. S. Harvey, Jr., H. P. Gavin, Double rolling isolation systems: A mathematical model and experimental validation, International Journal of Non-Linear Mechanics 61 (2014) 80–92, doi:10.1016/j.ijnonlinmec.2014.01.011.

P. S. Harvey, Jr., K. C. Kelly, A review of rolling-type seismic isolation: Historical development and future directions, Engineering Structures 125 (2016) 521–531, doi:10.1016/j.engstruct.2016.07.031.

P. S. Harvey, Jr., G.-P. Zéhil, H. P. Gavin, Experimental validation of simplified models for rolling isolation systems, Earthquake Engineering and Structural Dynamics 43 (2014) 1067–1088, doi:10.1002/eqe.2387.

N. Hoang, Y. Fujino, P. Warnitchai, Optimal tuned mass damper for seismic applications and practical design formulas, Engineering Structures 30 (3) (2008) 707–715, doi:10.1016/j.engstruct.2007.05.007.

M. Houseini, A. Soroor, Using Orthogonal Pairs of Rollers on Cancave Beds (OPRCB) as a base isolation system—part i: analytical, experimental and numerical studies of OPRCB isolators, The Structural Design of Tall and Special Buildings 20 (2011) 928–950, doi:10.1002/tal.568.

M. Houseini, A. Soroor, Using Orthogonal Pairs of Rollers on Cancave Beds (OPRCB) as a base isolation system—part ii: application to multi-story and tall buildings, The Structural Design of Tall and Special Buildings 22 (2013) 192–216, doi:10.1002/tal.671.

G. W. Housner, S. F. Masri, Performance of the base-isolated USC University Hospital under the 1994 Northridge earthquake, Nuclear Engineering and Design 148 (2) (1994) 509–513, doi:10.1016/0029-5493(94)90130-9.

R. A. Ibrahim, Recent advances in nonlinear passive vibration isolators, Journal of Sound and Vibration 314 (2008) 371–452, doi:10.1016/j.jsv.2008.01.014.

Y. Iwata, On the construction of the dynamic vibration absorber, Japanese Society of Mechanical Engineering 820 (1982) 150–152.

E. Jampole, G. Deierlein, E. Miranda, B. Fell, S. Swensen, C. Acevedo, Full-Scale Dynamic Testing of a Sliding Seismically Isolated Unibody House, Earthquake Spectra 32 (4) (2016) 2245–2270, doi:10.1193/010616EQS003M.

E. A. Jampole, S. D. Swensen, B. Fell, E. Miranda, G. G. Deierlein, Dynamic testing of a low-cost sliding isolation system for light-frame residential structures, in: Proceedings of 10NCEE, Anchorage, AK, 2014.

R. S. Jangid, Stochastic seismic response of structures isolated by rolling rods, Engineering Structures 22(8) (2000) 937–946, doi:10.1016/S0141-0296(99)00041-3.

K. Kanai, Semi-Empirical Formula for the Seismic Characteristics of the Ground, Bulletin of the Earthquake Research Institute 35, University of Tokyo, Tokyo, Japan.

A. Kasalanati, A. Reinhorn, M. Constantinou, D. Sanders, Experimental study of ball-in-cone isolation system, in: Building to Last: Proceedings of the 15th Structures Congress, ASCE, New York, 1191–1195, 1997.

J. M. Kelly, Aseismic base isolation: review and bibliography, Soil Dynamics and Earthquake Engineering 5 (4) (1986) 202–216, doi:10.1016/0267-7261(86)90006-0.

J. M. Kelly, Base Isolation: Linear Theory and Design, Earthquake Spectra 6 (2) (1990) 223–244, doi:10.1193/1.1585566.

J. M. Kelly, The role of damping in seismic isolation, Earthquake Engineering and Structural Dynamics 28 (1999) 3–20, doi:10.1002/(SICI)1096-9845(199901)28:1⟨3::AID-EQE801⟩3.0.CO;2-D.

G. C. Lee, Y.-C. Ou, T. Niu, J. Song, Z. Liang, Characterization of a Roller Seismic Isolation Bearing with Supplemental Energy Dissipation for Highway Bridges, Journal of Structural Engineering 136 (2010) 502–510, doi:10.1061/(ASCE)ST.1943-541X.0000136.

T. W. Lin, C. C. Chern, C. C. Hone, Experimental-study of base-isolation by free rolling rods, Earthquake Engineering and Structural Dynamics 24(12) (1995) 1645–1650, doi:10.1002/eqe.4290241207.

T.-W. Lin, C. C. Hone, Base isolation by free rolling rods under basement, Earthquake Engineering and Structural Dynamics 22 (1993) 261–273, doi:10.1002/eqe.4290220307.

D. Lopez Garcia, T. T. Soong, Sliding fragility of block-type non-structural components. Part 1: Unrestrained components, Earthquake Engineering and Structural Dynamics 32 (2003a) 111–129, doi:10.1002/eqe.217.

D. Lopez Garcia, T. T. Soong, Sliding fragility of block-type non-structural components. Part 2: Restrained components, Earthquake Engineering and Structural Dynamics 32 (2003b) 131–149, doi:10.1002/eqe.218.

T. A. Morgan, S. A. Mahin, The use of base isolation systems to achieve complex seismic performance objectives, Pacific Earthquake Engineering Research Center, 2011.

G. Mosqueda, A. S. Whittaker, G. L. Fenves, Characterization and modeling of friction pendulum bearings subjected to multiple components of excitation, Journal of Structural Engineering 130(3) (2004) 433–442, doi:10.1061/(ASCE)0733-9445(2004)130:3(433).

A. M. Nacamuli, K. M. Sinclair, Seismic Isolation: Applications of WorkSafe Technologies Ball-N-Cone Isolator, in: Structures Congress 2011, Structural Engineering Institute (SEI), Las Vegas, Nevada, United States, 852–863, 2011.

F. Naeim, J. M. Kelly, Design of seismic isolated structures, John Wiley & Sons, New York, NY, 1999.

J. Ormondroyd, J. P. Den Hartog, The Theory of the Dynamic Vibration Absorber, Journal of Applied Mechanics 50 (7).

Y.-C. Ou, J. Song, G. C. Lee, A parametric study of seismic behabior of roller seismic isolation bearings for highway bridges, Earthquake Engineering and Structural Dynamics 39 (2010) 541–559, doi:10.1002/eqe.958.

M. Ozer, T. Royston, Extending Den Hartog's vibration absorber technique to multi-degree-of-freedom systems, Journal of Vibration and Acoustics, Transactions of the ASME 127 (4) (2005) 341–350, doi:10.1115/1.1924642.

A. Penkuhn, Three point foundation for building structures, U.S. patent 3347002, 1967.

F. F. Pieterse, A. L. Nel, The advantages of 3D printing in undergraduate Mechanical Engineering research, in: 2016 IEEE Global Engineering Education Conference, Abu Dhabi, UAE, 25–31, doi:10.1109/EDUCON.2016.7474526, 2016.

K. A. Porter, G. S. Johnson, M. M. Zadeh, C. R. Scawthorn, S. J. Eder, Seismic Vulnerability of Equipment in Critical Facilities: Life-Safety and Operational Consequences, NCEER-93-0022, Tech. Rep., Multidisciplinary Center for Earthquake Engineering Research State University of New York, Buffalo, NY, 1993.

E. Sato, S. Furukawa, A. Kakehi, M. Nakashima, Full-scale shaking table test for examination of safety and functionality of base-isolated medical facilities, Earthquake Engineering & Structural Dynamics 40 (13) (2011) 1435–1453, doi:10.1002/eqe.1097.

H. Tajimi, A statistical method of determining the maximum response of a building structure during an earthquake, in: Proc. 2nd World Conference on Earthquake Engineering, vol. II, 781–798, 1960.

I. Takewaki, Robustness of base-isolated high-rise buildings under code-specified ground motions, The Structural Design of Tall and Special Buildings 17 (2) (2008) 257–271, doi:10.1002/tal.350.

Telcordia Technologies (Ed.), Network Equipment-Building System NEBS Requirements: Physical Protection, GR-63-CORE, Piscataway, NJ, 2012.

C. S. Tsai, Y. C. Lin, H. C. Su, Characterization and modeling of multiple friction pendulum isolation system with numerous sliding interfaces, Earthquake Engineering & Structural Dynamics 39 (13) (2010) 1463–1491, doi:10.1002/eqe.1044.

M.-H. Tsai, S.-Y. Wu, K.-C. Chang, G. C. Lee, Shaking table tests of a scale bridge model with rolling-type seismic isolation bearings, Engineering Structures 29 (2007) 694–702, doi:10.1016/j.engstruct.2006.05.025.

D. Vamvatsikos, C. A. Cornell, Incremental dynamic analysis, Earthquake Engineering and Structural Dynamics 31 (3) (2002) 491–514, doi:10.1002/eqe.141.

L. N. Virgin, Enhancing the teaching of linear structural analysis using additive manufacturing, Engineering Structures 150 (Supplement C) (2017a) 135–142, doi:10.1016/j.engstruct.2017.07.054.

L. N. Virgin, Enhancing the teaching of structural dynamics using additive manufacturing, Engineering Structures 152 (Supplement C) (2017b) 750–757, doi:10.1016/j.engstruct.2017.09.052.

G. P. Warn, K. L. Ryan, A review of seismic isolation for buildings: Historical development and research needs, Buildings 2 (2012) 300–325, doi:10.3390/buildings2030300.

B. Wei, R. Cui, G. Dai, Seismic performance of a rolling-damper isolation system, Journal of Vibroengineering 15 (3).

WorkSafe Technologies, Inc., ISO-Base platform, URL http://www.worksafetech.com/, 2011.

C.-Y. Yang, C.-H. Hsieh, L.-L. Chung, H.-M. Chen, L.-Y. Wu, Effectiveness of an eccentric rolling isolation system with friction damping, Journal of Vibration and Control 18 (2011) 2149–2163, doi:10.1177/1077546311428633.

Appendix A

Drawings of Isolation Bearings

Figs. A.1, A.2, and A.3 show the design drawings of the 3D printed bearing components.

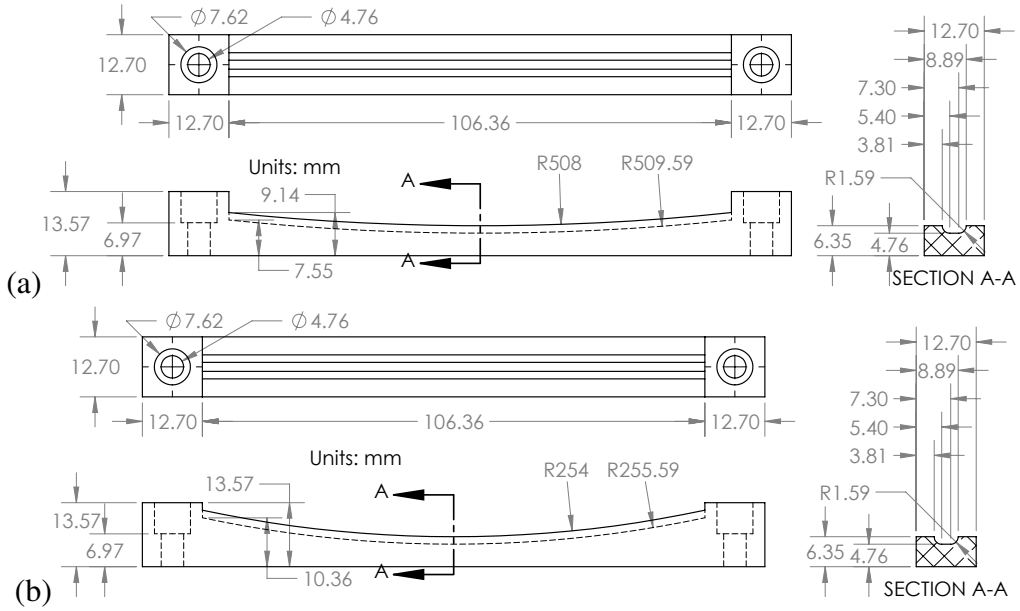

Figure A.1: Details of sliding/rolling surfaces used in FP/RP bearings with R = (a) 508 mm and (b) 254 mm.

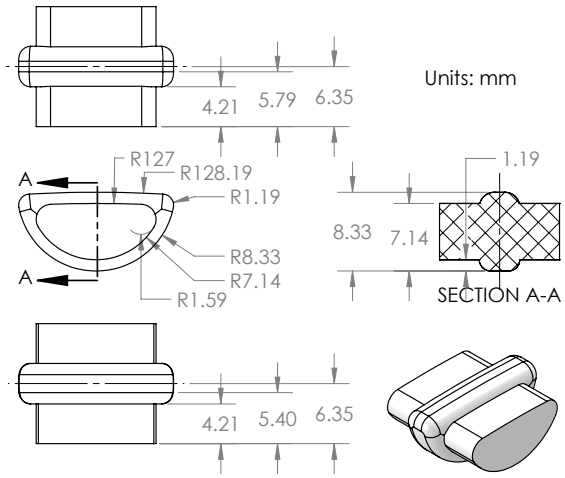

Figure A.2: Details of articulated slider used in FB bearings.

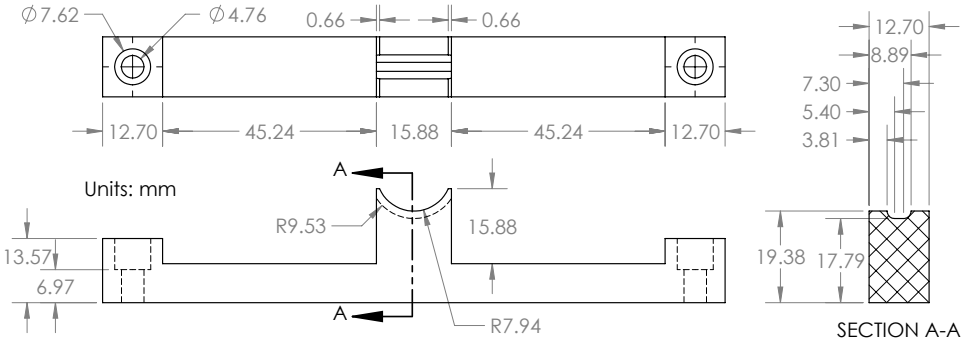

Figure A.3: Details of upper mount for FB bearing.